SYNTHESIS AND FUNCTIONALIZATION OF IRON OXIDE NANOPARTICLES AND THEIR APPLICATION IN HYBRID MATERIALS

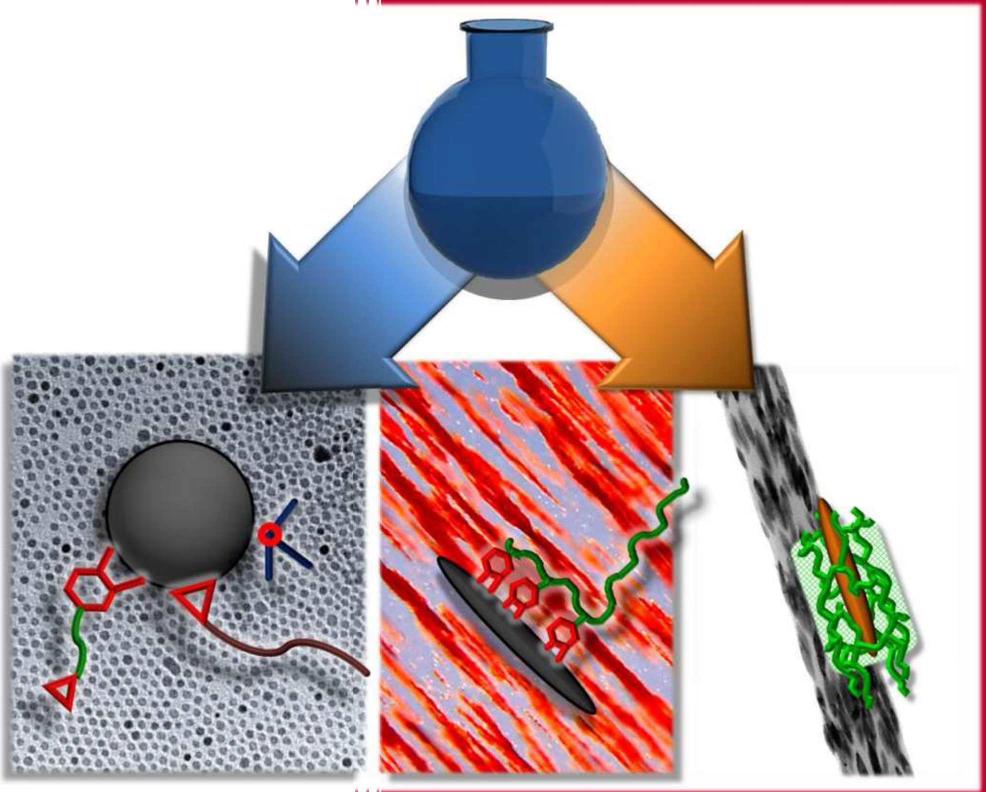

Dissertation

Phillip Daniel

Johannes Gutenberg-Universität Mainz

2017

SYNTHESIS AND FUNCTIONALIZATION OF IRON OXIDE NANOPARICLES AND THEIR APPLICATION IN HYBRID MATERIALS

Dissertation

Zur Erlangung des Grades

“Doktor der Naturwissenschaften”

Fachbereich Chemie, Pharmazie und Geowissenschaften der

Johannes Gutenberg-Universität Mainz

vorgelegt von

Phillip Georg Daniel

Geboren in Mainz

Mainz, 2017

[redacted]

Dean of Faculty: [redacted]

1st report: [redacted]

2nd report: [redacted]

Submitted:

Oral exam:

JG|U

Max Planck Graduate Center
mit der Johannes Gutenberg-Universität Mainz


AK
TREMEL

ABSTRACT

English

Nanomaterials have been in the center of interest for several decades now, and the number of publications and applications still grows. However, there are many aspects of nanoparticle formation and behavior still unknown. In particular, the coordination of ligands onto a particle surface holds many questions because of the intermediate states of nanoparticles, lying between bulk and molecule-like behavior.

In this work, two synthetic methods were used to make spherical and spindle-shaped particles of different iron oxides. Strongly magnetic maghemite (γ-Fe_2O_3) spheres were used as a model system to investigate the binding of the surfactant molecules oleic acid, 3,4-dihydroxyhydrocinamic acid and tetramethylammonium hydroxide. Here the focus was on the nature of the exchange of one ligand against another one. The magnetic properties inside solid polymer matrices were investigated with particles of different functionalization in PMMA and polydopamineacrylate (PDAm). Particles incorporated in PDAm exhibited interesting changes in the magnetic moment which resulted from a chemical reaction of the polymer bound to the particle and forming a shell with opposite magnetic moment. Such chemically controllable magnetism might be applied in data storage and switchable technologies.

Weakly ferromagnetic spindle-shaped hematite (α-Fe_2O_3) particles were synthesized using variable reaction parameters. This research was meant to show how these parameters affect the length and the aspect ratio of the particles. The particles were used to make mesogenic phases in polyethylene glycol (400) as a solvent. The orientation of the lyotropic liquid crystal phase could be directed by an external magnetic field. The flow of light can thus be directed magnetically. Furthermore, different concentrations of hematite particles were embedded in polyvinyl alcohol via an electrospinning process and their peroxidase-like behavior and wound healing properties were probed. The particles inside the fiber meshes catalytically convert reactive H_2O_2 to H_2O and O_2 and thus promote the healing process of skin tissue. This composite offers a cheap and easy way to produce band-aids for wound treatment.

German

Nanomaterialien sind seit mehreren Dekaden im Fokus der Forschung und die Zahl der Publikationen steigt stetig weiter. Dennoch sind viele grundlegenden Aspekte der Nanopartikelbildung weiterhin nicht vollständig aufgeklärt. Im Besonderen wirft die Wechselwirkung von Liganden und Parikeloberfläche noch viele Fragen auf.

In dieser Arbeit werden zwei bekannte Synthesen zur Darstellung stark magnetischer, spherischer Maghemitpartikel (γ-Fe_2O_3) und spindelförmiger Hämatitpartikel (α-Fe_2O_3) verwendet. Maghemit wurde als Modell herangezogen, um die Wechselwirkung und Bindung von Oberflächenliganden wie Ölsäure, 3,4-Dihydroxydihydrozimtsäure und Tetramethylammoniumhydroxid zu untersuchen. Dabei lag der Fokus auf dem Austausch der Liganden. Der Einfluss von unterschiedlichen Polymermatrices auf die magnetischen Eigenschaften der Partikel wurde mit Polymethylmethacrylat (PMMA) als passive und Polydopaminacrylat (PDAm) als aktive, katecholfunktionalisierte Matrix untersucht. Die Partikel in PDAm zeigten verringerte Sättigungsmagetisierung, die durch die Reaktion des Polymers mit der Partikeloberfläche verursacht wurde. Solch chemisch kontrollierbarer Magnetismus ist interessant für schaltbare Datenspeicher.

Schwach magnetische, spindelförmige Hämatitpartikel (α-Fe_2O_3) wurden mit veränderten Reaktionsparametern synthetisiert. Dabei wurde der Einfluss der Paramter auf die Form, Größe und Seitenverhältnisse genauer untersucht. Mit diesen Partikeln wurden lyotrope, flüssigkristalline Phasen hergestellt, die sich mit einem externen Magentfeld ausrichten ließen. Darüber hinaus wurde die katalytische Aktivität der Hämatitpartikel genutzt, um Fasern herzustellen, die in einer katalaseähnlichen Reaktion H_2O_2 Konzentration senken können und dabei H_2O und O_2 produzieren. Die Fasern wurden mittels Electrospinning aus partikelhaltiger PVA Lösung erzeugt und zeigten in Experimenten mit Zellen, dass sie zelltoxische H_2O_2 Konzentrationen verringern und so Zellwachstum fördern können. Dies ermöglicht die Anwendung als Hautpflaster.

“Ist der Zettel noch so klein, es gehört auch noch ein Datum rein!”

In memory of KJD

„Wenn man sein Ziel nicht kennt, sind alle Wege falsch“

Konfuzius

ACRONYMS

acac: acetylacetonate

AFM: Antiferromagnetism / antiferromagnetic

ATR FTIR spectroscopy: Attenuated wave total reflection Fourier transformed infrared spectroscopy

DBE: Dibenzyl ether

DMA: Dimethylacetamide

DPE: (Di)phenyl ether

emu: electromagnetic unit

FC: Field cooling

FM: Ferromagnetism / ferromagnetic

HDD: 1,2-hexadecandiol

LC: Liquid Crystal

$NOBF_4$: nitrosonium tetrafluoroborate

NP: nanoparticle

OA: Oleic acid

OAm: Oleyl amine

Oe: Oersted

P(DEGMEMA-*b*-DOPA): poly ((diethylenglycol monomethyl ether) methacrylate-*b*-dopamine acryl amide)

P(MMA-*b*-DOPA): poly (methyl methacrylate-*b*-dopamine acryl amide)

PDAm: poly dopamine acrylate

PMMA: poly methyl methacrylate

POM: polarization microscopy

PVA: polyvilyl alcohol

ROS: Reactive oxygen species

RAFT (polymerization): radical addition fragmentation transfer

SEM: Scanning Electron Microscope

SQUID: Superconducting Quantum Interference Device

TDD: 1,2-tetradecandiol

TEM: Transmission Electron Microscope

TGA: Thermogravimetric analysis

UV-VIS spectroscopy: Ultraviolet – visible light spectroscopy

XRD: X-ray diffraction

ZFC: Zero field cooling

Contents

All research has been done between 2013 and 2017 in the research team of [redacted]. This thesis was supervised by [redacted]

ACKNOWLEDGEMENT

Thanks to

- [redacted]
- [redacted]
- [redacted]
- [redacted]
- [redacted]
- [redacted]
- [redacted]
- [redacted]
- [redacted]
- [redacted]
- [redacted]
- [redacted]
- [redacted]
- [redacted]
- [redacted]

I. INTRODUCTION AND MOTIVATION

Almost every mineral in the earth's crust is a metal oxide. The most abundant transition metals in these oxides are titanium and iron. Iron oxides usually show some magnetization because of the two common oxidation states 2+ and 3+ (ferrous and ferric). The electronic configurations in these cases are $3d^6$ and $3d^5$, respectively. The high spin state in common oxide minerals like hematite, maghemite and magnetite therefore leads to a magnetic moment of the ions in tetrahedral or octahedral coordination. Hematite is the thermodynamically stable composition. Magnetite was the first ever discovered permanent magnet, which also led to the name and was of great industrial and scientific interest as a data storage medium up to the 1960s. Today, iron oxides are still of high interest in nanochemistry because of the cheap and abundant starting chemicals, controllable synthetic procedures and applications for new magnetic data storage devices.[1] As nanoparticles, even common compounds like magnetite could push the limits of magnetic storage. For example, particles with diameters around 5 nm as single bits are calculated to result in a 1 $\mathrm{Tb/in^2}$ storage density.[2] Further possible applications for nanoparticles in the medical realm are vehicles for drug or radionuclide delivery or as contrast agent for resonance imaging. In the technical realm, an improvement of data storage devices and application in spintronic devices are possible.

Over decades of research, many different synthetic routes have been developed in nanochemistry. Although gas phase processes and top-down methods like lithography offer good yields at low cost, the liquid-phase synthesis appears to be the most promising method for a control over size, shape and composition, as well as morphology. Liquid-phase methods consist of hydrolytic and nonhydrolytic sol-gel, hydrothermal, solvothermal, template-assisted and also biomimetic approaches. Because of the wide range of possible properties, metal oxides are of great interest in nanoscience. This results from a great variety of structures ranging from simple NaCl to more complex structure types. Thus interesting electronic (insulator, semiconductor, metal) and magnetic properties (ferro, ferri, or antiferromagnetism) or even switchable ferroelectric behavior can be observed. Hundreds of publications every year describe new strategies or improvements of established syntheses.[3]

Physical properties and chemical behavior of nanoparticles differ from those of the respective bulk materials due to the small particle size and large surface to volume ratio. Even though the physical properties of small magnetic particles are well understood, the interpretation of data from nanoparticle samples is still complicated. This is especially the case when different particle sizes are present in one sample. The chemical reactions with other chemical substances occur at the surface while the physical properties originate from the crystal structure of the bulk. As a consequence, small changes in surface coordination may have a large impact on the behavior of one particle as a whole.[2] For example, magnetism strongly correlates with particle size and surface modification of nanoparticles.

In most cases, the particles are already functionalized during synthesis. In organic solvents surfactants serve as stabilizers for the nanocrystals. They control growth and shape and the speed of formation. In the end they are bound to the surface, determining the solubility of the particles. When hydrophilic particles are synthesized in aqueous media, they are often functionalized in a second step. Surfactants prevent agglomeration and grant stable colloidal dispersions. A popular example is a ferrofluid of magnetic iron oxide particles that do not precipitate even after a long time. They are usually functionalized with tetramethylammonium hydroxide or perchlorate. In acidic solution the hydroxyl groups on the surface are then protonated, resulting in a positive layer that repels other positively charged particles. Chemically bound organic surfactant molecules and polymers protect nanoparticles by forming a single or double layer. The binding groups for iron oxide particles are mainly carboxylic acids, phosphates, sulfates and catechols. The steric repulsion counterbalances the magnetic attraction and van-der-Waals forces. Even though they cannot protect against oxidation and etching, organic surface molecules play an important role in medicine. The surface molecules can improve the transport of particles in the blood stream and the uptake into targeted cells for imaging diagnostic methods and treatment.[4]

Polymers can not only function as ligands but also simultaneously as a matrix. Nanoparticle-polymer-hybrids are common in nature and can be found in seashells, bones and teeth of certain snails[5]. The extreme stability of such composites leads to a wide use in man made products like tires. Locking particles in high viscous or stiff polymers completely prevents agglomeration and controls interparticle interaction by fixing a certain distance between the particles. Furthermore, due to the interaction of particle and matrix at the interface, the properties of such hybrid materials are more than the sum of the organic and inorganic components, and do not only depend on their ratio. This gives access to optically clear and oxidation- and ablation-resistant materials. In soft polymer networks, translation of particles is blocked while rotation in a certain angular range might be possible, which can be used for sensors and switches.[6]

Over the last decades, nanoparticles received increased attention because of their use in catalysis and as artificial enzymes. Compared to natural enzymes with one active metal ion center, nanoparticles are less selective but exhibit more active ions on the surface. Furthermore, the metal ions can be accessed by a substrate more easily. Thus the catalytic activity of nanoparticles is usually higher than that of natural enzymes. Along with the low cost of nanoparticle production, a wide range of applications like biosensing, immunoassays, cancer diagnostics, neuroprotection and stem cell growth is possible. Recently it was discovered that magnetic Fe_3O_4 nanoparticles exhibit peroxidase-like activity and therefore mimic a large family of enzymes that are naturally used to protect the body from reactive oxygen species (ROS) such as peroxide molecules and radicals. Hematite particles are known to show peroxidase-like properties.[7]

This work focused on the synthesis of different iron oxides, namely hematite and maghemite, of different shapes and sizes. The goal was to analyze the formation mechanism and the possibilities of functionalization of the particles with molecule and polymer ligands. The magnetic behavior and catalytic activity were of particular interest. Using the strong magnetic moment and morphology of the particles, their behavior as part of a hybrid liquid crystal system was probed. In the liquid crystal composite system the inorganic, anisotropic particles served as the mesogenic phase, the orientation of which could be controlled by a commercially available magnet.[8]

II. THEORETICAL BACKGROUND

Nanoparticles behave differently from their bulk counterparts. This arises from the high surface to volume ratio, which positions nanoparticles properties somewhere between that of molecules and bulk solids. There is a variety of reliable synthetic methods for a multitude of sizes and shapes of iron oxide particles. Precursor chemicals range from iron oleate ($Fe(C_{18}H_{35}O_2)_3$) or iron acetylacetonate ($(Fe(C_5H_7O_2)_3$ to other molecular iron complexes.[9] Additionally, the conditions vary between moderate temperatures in aqueous solution during co-precipitation[10] to high temperature thermal decomposition in ionic liquids[11–13] or high boiling organic solvents.[13,14] Morphology as well as the phase of the oxide can be tuned with the reaction parameters like molar ratios of precursor, surfactant and solvent, heating rate and reaction temperature and time. Other factors, such as additives,[15] stirring rate and formation of bubbles[16] during boiling can also influence the outcome of a reaction. During the reaction of iron acetylacetonate in organic solvents, a steep heating curve leads to bigger particles and even cubic shape, while slower heating results in small spherical particles.[17] Surfactants like oleic acid (OA, $C_{18}H_{36}O_2$) have a large influence on the size and shape of the particles. There is a dynamic equilibrium of free surfactants and surface bound molecules during the reaction. Bound surfactants block other precursor monomers from adding to the particle. The bond is easily broken again at high temperatures so on an average every site is equally blocked and the particle can grow homogeneously. In some cases the affinity of the surfactant towards a certain crystallographic plane of the particle is stronger and this plane will be blocked while other planes continue to grow. The functionalized planes will vanish while the growing planes dominate the final shape of the particle.[18,19] After the synthesis, the particles have to be re-functionalized properly to fit the application. In some cases this can be done directly after the reaction in the same vessel, or in a subsequent second step. Numerous different ligand molecules or polymers are used to bind to the surface. Depending on the targeted applications, these ligands can form biocompatible shells, change solubility or can release medical drugs. Many of the different iron oxide phases that are known as bulk materials have been synthesized as nanomaterials as well. The most important iron oxides are summarized briefly. Many iron oxides obtain some sort of collective magnetism like ferri- or ferromagnetism. At the nanoscale only a single domain is present in one particle and the magnetic behavior changes drastically. In addition to that, magnetic moments of surface ions are no longer negligible, as it is the case with bulk samples.

Iron oxide Phases

Hematite

The crystal structure of hematite (α-Fe_2O_3) is shown in **Figure 1**. It is the most common iron oxide while crystallizes in the rhombohedral corundum structure type with space group $R\bar{3}c$. It can be described as a distorted hexagonally close packed arrangement of oxide anions with Fe^{3+} in 2/3rd of the octahedral interstices. Antiferromagnetic ordering exists up to the Neel temperature ($T_N = 948$ K). However, only below the Morin temperature $T_M = 250$ K (for bulk hematite), the two magnetic sublattices are perfectly antiparallel along the c-axis of the rhombohedral lattice.[20] Magnetic moments lie in the basal planes and are aligned in parallel, and coupled antiparallel between adjacent planes.[21] Above T_M the magnetic moments flip by 90° from the antiferromagnetic axis which causes a small magnetization. This leads to a weak ferromagnetic (WF) state and a small magnetic moment in the basal plane (perpendicular to the c-axis). Thus hematite is weakly ferromagnetic between T_M and T_N (250 K and 950 K).[22] Usually, the weak dipole-dipole interactions are not taken into account. The Morin temperature decreases with smaller particle size. For very small particles below 30 nm, surface defects and uncompensated magnetic moments outweigh magnetic bulk effects.[23]

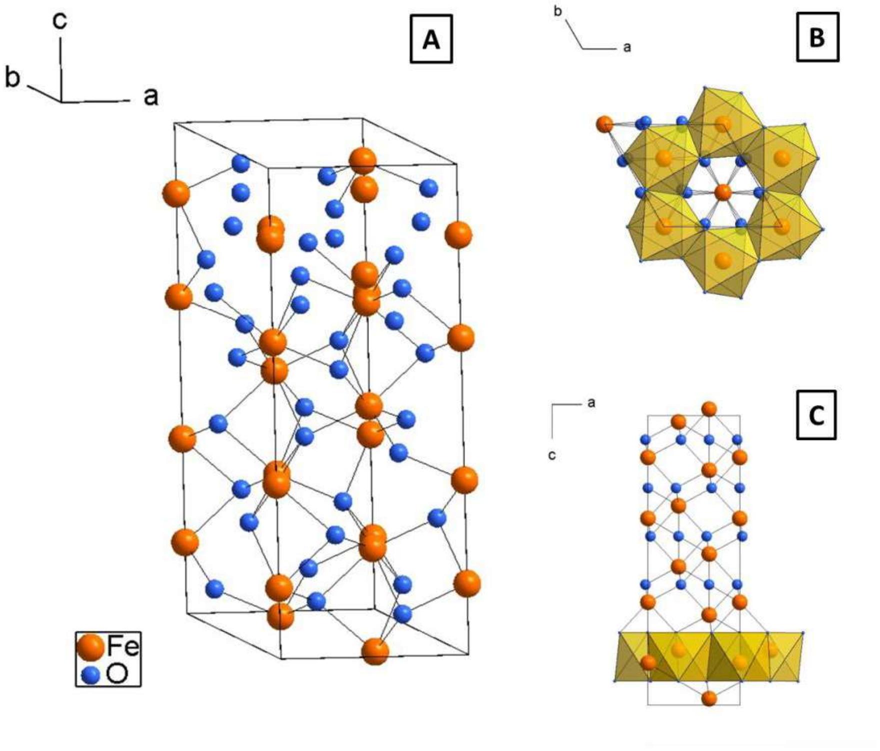

Figure 1: Crystal structure of hematite (A). (B) and (C) show the hexagonal orientation of octahedra along the c and the b axes, respectively.[24]

Magnetite

Figure 2 adopts the crystal structure of magnetite ($Fd\bar{3}m$). Magnetite (Fe_3O_4) is an inverse spinel of the general composition AB_2O_4 for $Fe^{3+}[Fe^{2+},Fe^{3+}]O_4$. It has a cubic closest packed (ccp) oxide structure with ½ of the octahedral voids occupied by Fe^{3+} and Fe^{2+} in a 1:1 ordered manner.1/8 of the smaller tetrahedral sites are occupied by ferric (Fe^{3+}) ions. As a comparison, in a regular spinel the tri valent ions occupy half the octahedral, and the bivalent species 1/4th of the tetrahedral holes. Rapid electron hopping between the bivalent and trivalent ions in the octahedral sites is possible, which makes the oxide a thermally activated conductor. There are two magnetic sublattices with opposite magnetic moment of ions in the tetrahedral and octahedral sites, respectively. This causes the material to be ferrimagnetic with a Néel temperature $T_N = 860$ K. At low temperatures (120 K) magnetite undergoes an insulator-metal transition (Verwey transition).[1] Along with this first order phase transition, there is a charge ordering process, which is accompanied by a reduction in symmetry from cubic to monoclinic, and it is accompanied by a change in magnetization.[25] Of all iron oxide phases, magnetite has the highest saturation magnetization. The reported values for bulk materials range from ~ 84 to 92 emu/g.[26]

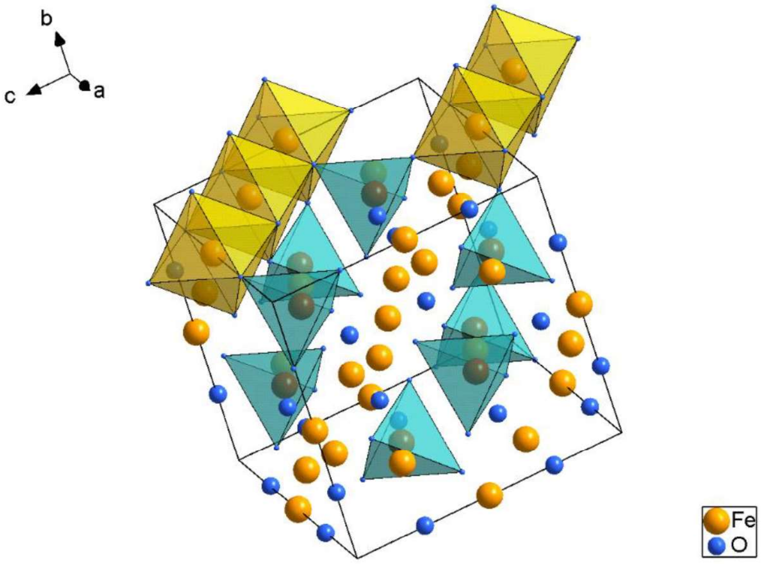

Figure 2: Crystal structure of magnetite. Some octahedral and tetrahedral cation positions are colored yellow and blue, respectively.[27]

Maghemite

The crystal structure of maghemite is shown in **Figure 3**. The structure is very similar to that of magnetite. Maghemite (γ-Fe_2O_3) gets its name from a mixture of magnetite and hematite because it resembles magnetite in its structure but has only ferric irons (Fe^{3+}). It can be described as defect structure of Fe_3O_4 with no Fe^{2+} and written as $Fe^{3+}[Fe^{3+},\square]O_4$ with □ illustrating the ferrous cation vacancies on the octahedral positions. Only ferric ions are distributed statistically over the octahedral sites. This leads to a loss in symmetry. Maghemite adopts the space group $P4_132$ and is a ferrimagnet, but the reported Néel temperatures range from $T_N = 620$ K (as bulk)[22] to 928 K[26]. As in magnetite, the magnetic ordering originates from superexchange interactions between two sublattices of iron in octahedral and tetrahedral sites with opposite magnetic moments. The saturation magnetization for bulk samples is reported to be between 74 – 80 emu/g.[26]

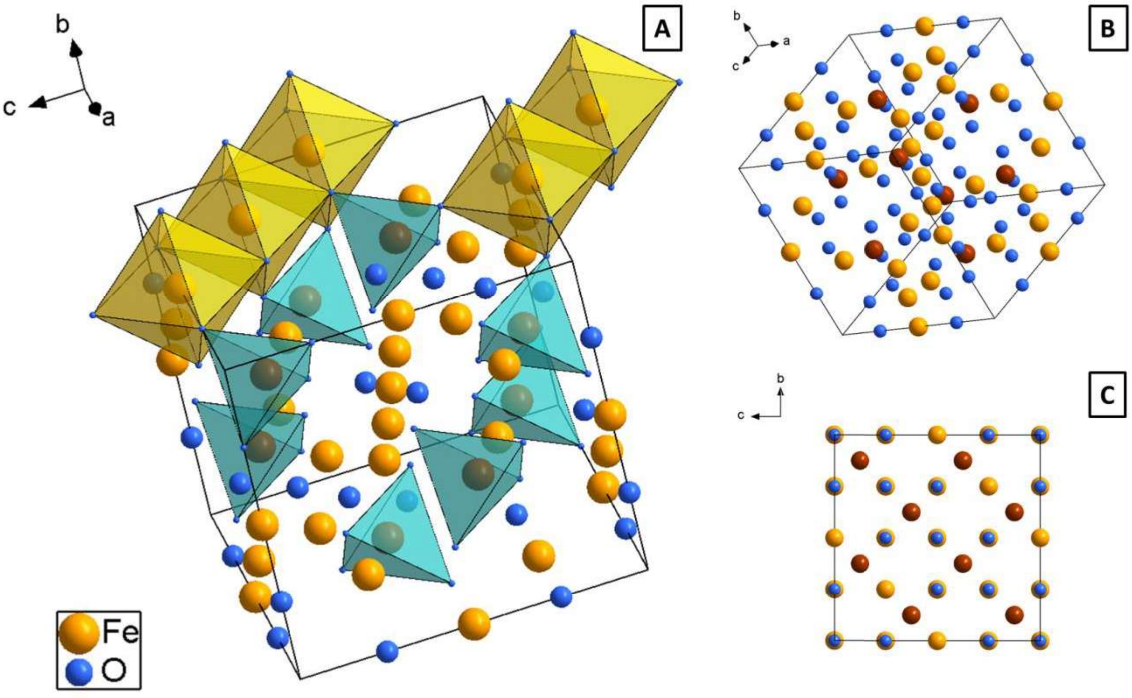

Figure 3: (A) Crystal structure of maghemite. Oxide anions (blue) form a closed packed structure with Fe(III) (yellow) in octahedral places highlighted in yellow and Fe(II) (brown) in tetrahedral voids highlighted in blue. The octahedral and tetrahedral sites are connected via common edges allowing the super exchange between Fe(II) and Fe(III). (C) shows the structure along the crystallographic c-axis.[28]

Akaganeite

Figure 4 shows the crystal structure of β-FeOOH akaganeite (FeO(OH, Cl)). The name comes from the akagane mine in Japan where the mineral was first discovered in natural deposits.[29] Akaganeite belongs to the iron oxide hydroxide class and has a hollandite type structure with the monoclinic space group *I2/m*. FeO_6 octahedra are connected via edges and form rings. Chloride and hydroxide can be substituted in the large “tunnels” within the crystal structure, as seen in **Figure 4** (C). Akaganeite forms small needle-like crystals. In crystal aggregates they tend to orient along the c-direction. The “tunnels” are therefore perpendicular to the c-axis, which makes this oxide especially interesting for ion loading and catalytic applications. Akaganeite is antiferromagnetic with a Néel temperature of 260 - 299 K[30]. However, the magnetic properties are largely influenced by the size and shape of the particles. [31]

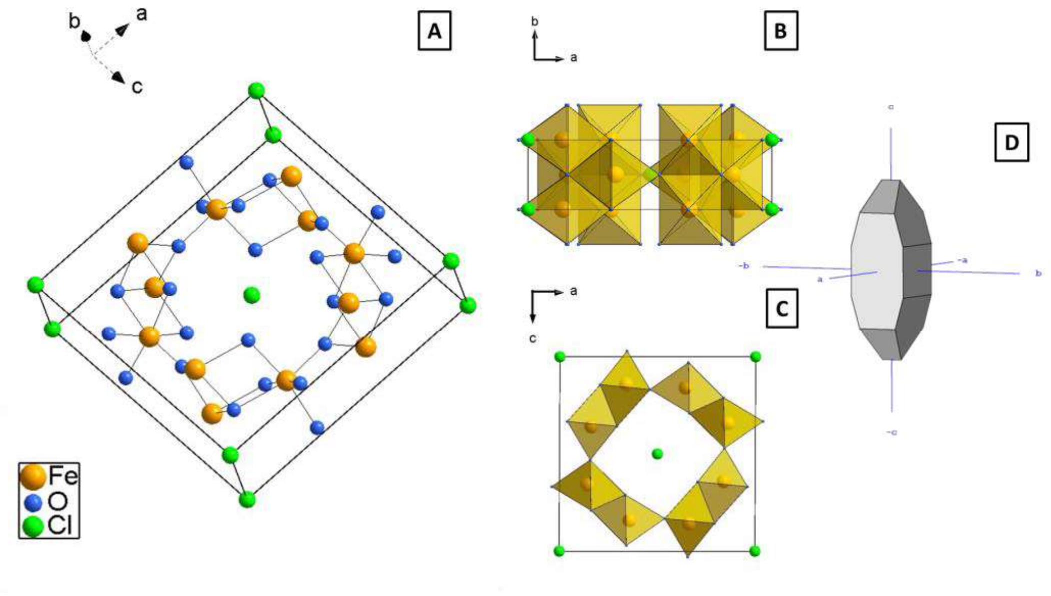

Figure 4: Crystal structure of akaganeite. FeO_6-octaedra are highlighted in yellow to illustrate the probable orientation of the crystal growth along the c-axis (B-C). (D) Typical morphology of an anisotropic akaganeite crystal.[32]

Magnetism

Collective magnetism and domain walls[1]

Materials either exhibit paramagnetic or diamagnetic properties that determine their behavior inside an inhomogeneous, external magnetic field. The respective properties originate from unpaired and paired electrons in the material. Paramagnetic materials are attracted and pulled inside an inhomogeneous field. Diamagnetic materials experience a repulsive force pushing them out of the field. The effect disappears instantly when the external field vanishes. Collective magnetism is a form of paramagnetism and remains after an external field is removed. Ferro-, anti-ferro- and ferrimagnetic materials have so-called Weiss domains in which the magnetic moments align parallel or antiparallel. **Figure 5** (A) illustrates the Weiss domains in the different materials. In ferromagnetic (FM) materials the magnetic moments of a magnetic sublattice are parallelly aligned inside the domains. Antiferromagnetism (AFM) has equal magnetic moments of opposite directions of the different sublattices inside the domains. Ferrimagnetism is a kind of

---

[1] Theory taken from magnetism skripts at https://www.wmi.badw.de

anitferromagnetism but the moments have different strength, which results in parallel net magnetic moments in one domain (see **Figure 5**).

The formation of domains as an energetic minimum is the result of opposite energies of the system. If a compound consists of only a single domain, it would be a permanent magnet with a magnetic field outside the solid and thus with a high magnetic field energy. Multiple smaller domains next to each other exhibit lower energy, because the magnetic flux propagates through the domains. **Figure 5** (B) illustrates the outside magnetic field for different domain sizes. Domains are separated by domain walls. The formation of domain walls requires energy proportional to the surface of the wall ($\sim r^2$). As a consequence, the resulting overall energy has a minimum at a certain domain volume. A system will tend to minimize the magnetic field energy by reducing the domain volume on one hand, while also minimizing domain wall surfaces on the other hand. The values of the domain wall energy, the thickness of the wall and the domain volume depends on the chemical composition, the crystal structure, the external field, temperature and other parameters. In a multidomain material with no net magnetization the magnetic moments of different domains cancel each other out. **Figure 5** (D) shows that an applied external field B causes the domains with magnetic moment to be parallel to the external field B to grow at the expense of adjacent domains with different magnetic orientation. This arrangement can persist after the field is turned off, turning the sample itself into a permanent magnet. **Figure 5** (E) schematically illustrates that inside the domain interface the magnetic moments rotate to the preferred orientation of the adjacent domain. The energy for the domain wall motion comes from the external magnetic field. Oscillating motion of domain walls created by an altering field dissipate energy as thermal energy into the material. This is the basic of hyperthermia treatments in cancer therapy.

The collective magnetic properties depend on temperature. Above the Curie temperature T_C for ferromagnetic, and the Néel temperature T_N for antiferromagnetic materials, the permanent magnetization will be lost and the material becomes paramagnetic. Nanoparticles are within the size range of Weiss domains and often contain only a single domain. Therefore they all possess a magnetic moment and an external field cannot change the size of the domain. As a result, they show a unique phenomenon known as superparamagnetism.

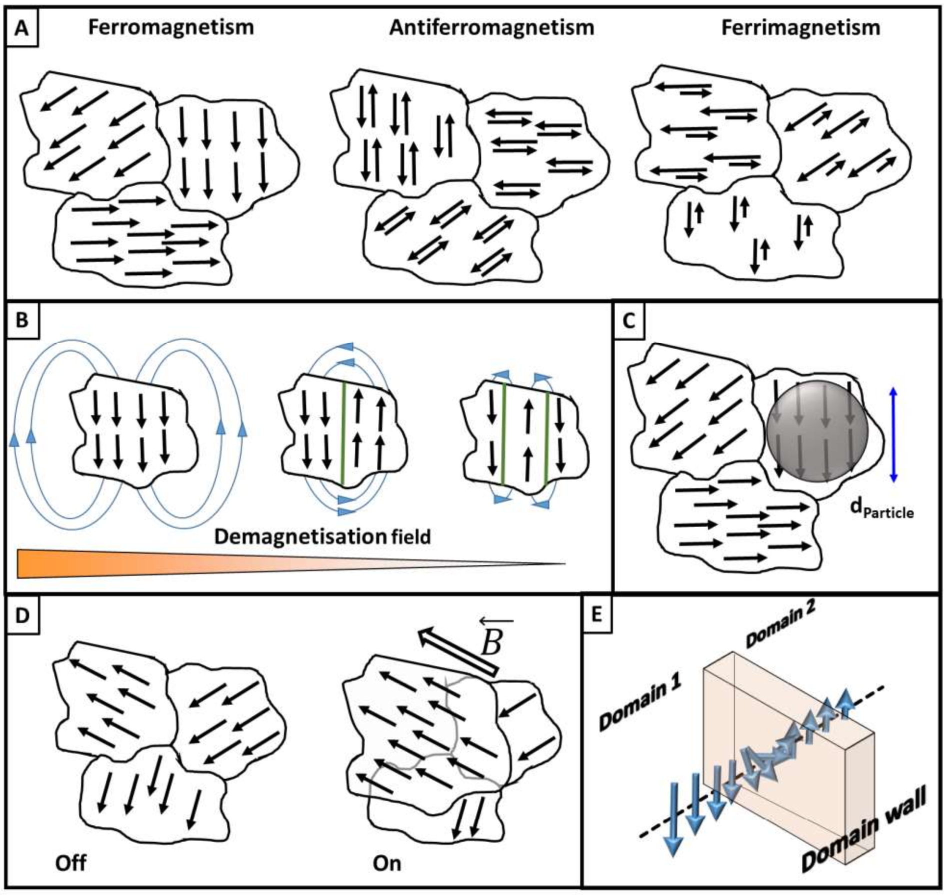

Figure 5: (A) Different types of collective magnetism. (B) Increase of the outer magnetic field (demagnetization field) with increasing domain volume. (C) For particle sizes smaller than an average domain, single-domain behavior is observed. (D) Growth of one domain when a field is applied. The domain wall schematically shown in (E).

Superparamagnetism – single domain particles

Some particles are smaller than the Weiss domains as illustrated in **Figure 5** (C) and thus only contain a single domain (single-domain particles). It is completely magnetized because all magnetic moments inside the particle are aligned in parallel. Thermal fluctuations of the magnetic moment cause the oriented state to relax and the overall magnetization to average zero after a short time. One single particle is a single paramagnet. A sample of small particles behaves like a paramagnetic sample, thus giving the name superparamagnetism. Lowering the temperature will decrease the thermal fluctuation and increase the relaxation time τ - the time it takes to break the uniaxial assembly of the magnetic moments.

$$\boldsymbol{\tau = \tau_0 e^{\frac{\Delta E}{k_B T}}} \qquad \textbf{(1)}$$

τ is the relaxation time, τ_0 is a material constant in the range of 10^{-9} to 10^{-12} s for ferro- or ferrimagnetic particles and 10^{-11} -10^{-13} for antiferromagnetic particles, k_B is the Boltzmann constant, T the temperature and ΔE the energy barrier the particle has to overcome to flip magnetization.[2] For non-interacting particles it is defined as

$$\Delta \boldsymbol{E} = \boldsymbol{KV} \tag{2}$$

Here the K and V are the anisotropy constant and the particle volume, respectively. Hence, the relaxation time increases with increasing particle volume. This is a simplified case since the energy barrier is influenced by both intrinsic and extrinsic factors.[32] Some important factors are

(1) Crystal anisotropy. This arises from spin-orbit coupling effects and quenching of orbital momentum, i.e., how far off the magnetic moment is from the symmetry axis of the crystallographic lattice.[2] This is depicted in **Figure 6**. The angle θ between the magnetization direction and the easy axis determines the crystal anisotropy energy.
(2) The morphology of the crystal determines the demagnetization field. For a spherical particle this anisotropy factor is zero.
(3) Surface structure of the crystal. Defects and reduced symmetry increase anisotropy.
(4) Dipolar interaction between adjacent particles in an agglomerated system.[14]

Figure 6 shows the energy of the magnetization vector as a function of the angle with respect to the easy axis of the particle. There can be multiple orientations of the magnetization vector, which result in minimal energy. When a magnetic field is applied the energies of the favored orientations shift and an easy axis parallel to the field is preferred.[2]

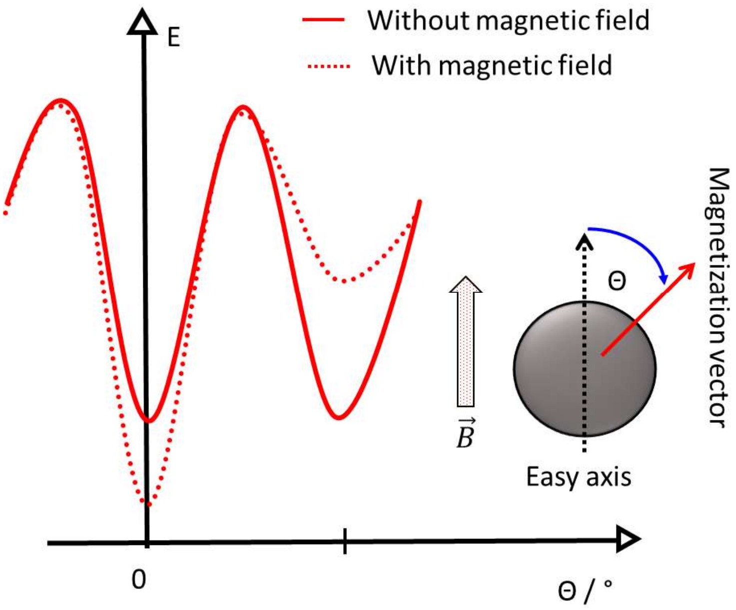

Figure 6: Magnetic energy of the system (nanoparticle) as a function of the angle θ between the magnetization vector and its direction with respect to the "easy" axis (direction of minimized energy).

The relaxation time τ is a combination of the Brownian relaxation τ_B, i.e. the reorientation of the whole particle due to thermal energy and Néel relaxation τ_N, which describes the reorientation of the magnetic vector along different easy axes of the particle. Brownian relaxation scales proportionally with the particle volume while Néel relaxation is an exponential function of the volume. The sum of the reciprocal relaxation times equals the total reciprocal relaxation time.[14]

$$\frac{1}{\tau} = \frac{1}{\tau_N} + \frac{1}{\tau_B} \tag{3}$$

If the time of the measurement τ_m is shorter than the relaxation time τ ($\tau_m < \tau$) the magnetic state of the sample is blocked. Otherwise the system will be in equilibrium again before the measurement is finished. This is shown schematically in **Figure 7**. The measuring time strongly depends on the method. For magnetization measurements DC mode is around $\tau_m = 10^2$ s, AC susceptibility around $\tau_m = 10^{-1} - 10^{-5}$ s and ^{57}Fe Mössbauer measurements around $\tau_m = 10^{-7} - 10^{-9}$ s. The temperature at which the flipping of magnetic moments is blocked (for a measurement with given τ_m) is called the blocking temperature T_B.

$$T_B = \frac{\Delta E}{k_B \ln\left(\frac{\tau_m}{\tau_0}\right)} \tag{4}$$

This equation connects the volume of the particles with the blocking temperature that can be extracted from measurements of magnetic moment over temperature.

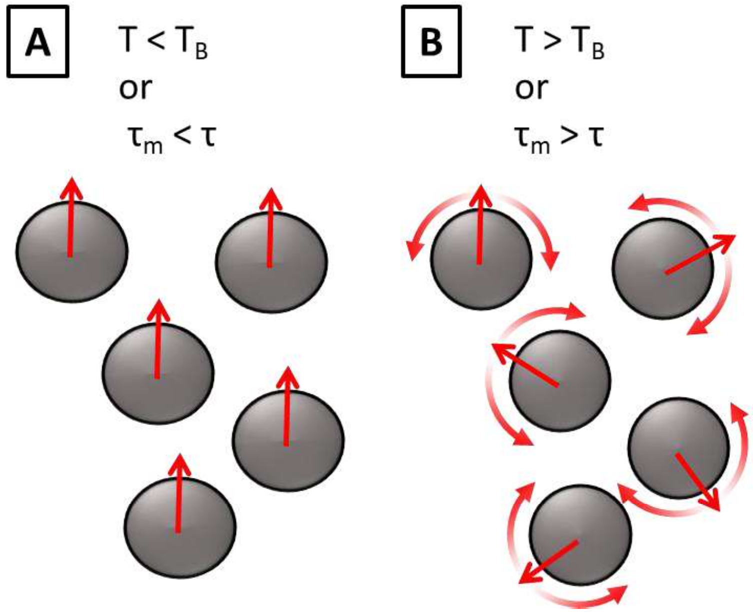

Figure 7: Magnetic moment orientation of magnetic nanocrystals. If the temperature is below T_B and $\tau_m > \tau$ a uniaxial alignment can be observed (A). In other cases the system is in equilibrium again (B).

Ferro- or ferrimagnetic materials can become superparamagnetic below a critical particle size. Above T_B the sample behaves as a paramagnet. Because the particle volume V is in the exponential term in equation (1), the relaxation time becomes longer for larger particles. Superparamagnetic particles have a high saturation magnetization but no hysteresis in $M(H)$ measurements, i.e. zero remanence and coercivity as shown in **Figure 8**. Another signature of superparamagnetism is that low magnetic fields are needed to saturate the magnetization of a sample, because the magnetic moments of whole particles are larger than the atomic moments of paramagnetic bulk compounds.

T_B is determined by measuring the magnetization as a function of temperature $M(T)$ with (FC) and without (ZFC) an external magnetic field H. Usually magnetization is measured during heating the sample from low temperatures (~5 K) to room temperature (RT) or higher. At low temperatures the magnetic moments are blocked. When the thermal energy increases, they align parallel to the external field and the magnetization increases. When the thermal energy equals ΔE, the randomization causes the magnetization to drop again. The maximum of ZFC curve therefore gives an approximate T_B value (depending on the measurement speed τ_m). In samples of weakly or non-interacting particles, this is also equal to the branching temperature, when ZFC and FC curves part because at temperatures higher than T_B the system should be in equilibrium regardless of heating or cooling steps. In many samples with a distribution of different particle volumes, T_{branch} and T_B do not coincide. For samples with a broad dispersity there is a range of blocking temperatures as seen from equation 5, which is a combination of equation 2 and 4. So while the largest particles of a batch are already blocked at a certain temperature, the smaller particles are still superparamagnetic.

$$T_B = \frac{KV}{k_B \ln\left(\frac{\tau_m}{\tau_0}\right)} \tag{5}$$

Particles with large dipole-dipole interactions cause the shape of the ZFC and FC curve to change. Above T_B the lines do not coincide. This means that the process is not reversible. This is because of collective behavior of the assembled particles.[33]

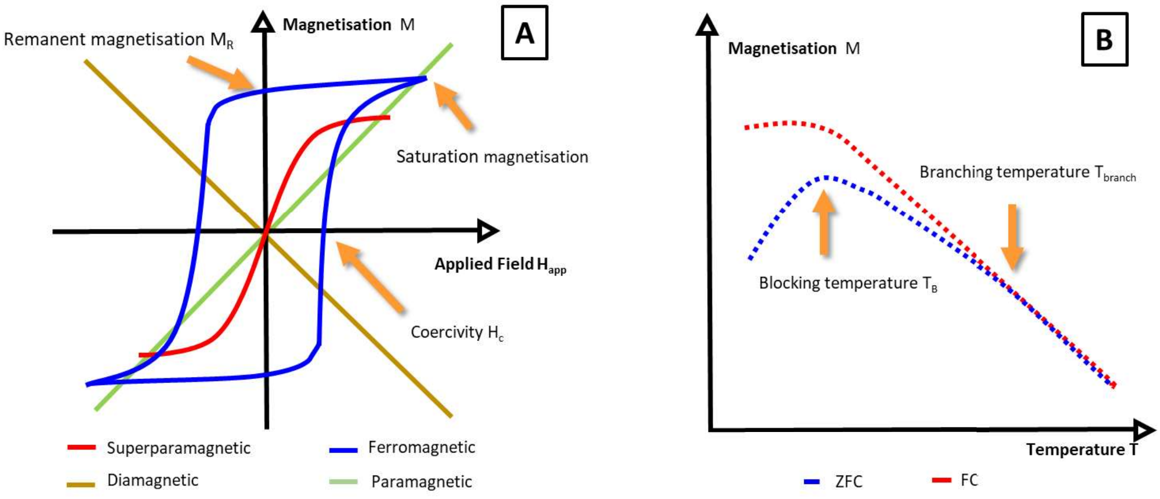

Figure 8: (A) Hysteresis curves of different magnetic phenomena. (B) Magnetic moment against temperature. In this case T_B and T_{branch} are different.

Synthetic methods

There are two common methods for precursor combustion in high-boiling organic solvents, hot-injection and heating-up. Hot-injection is a well-established method that has proven valuable for several nanoparticle systems. Into a preheated solution a mixture of solvent and precursor is added rapidly. This causes a spontaneous burst of nucleation (see below) and a drop in reaction temperature. The separation of the formation of particle seeds and the following growth ensure a narrow size distribution of the product. Lower temperature inhibits further nucleation and instead promotes growth of existing particles.

Hot-injection has several disadvantages that are hard to compensate in large scale synthesis. The method is sensitive to the injection speed and volume of the precursor solution, which has a large impact on the initial reaction kinetics. If the reaction volume is increased, a fast injection and homogeneous, rapid mixing and cooling of the solution cannot be guaranteed. As a consequence, there is no simultaneous oversaturation and no burst of nucleation. This causes unsteady growth and no formation of monodisperse particles.

This work will focus on the "heating-up" method. Heating-up is a non-injecting one-pot method in which a solution of precursors in high-boiling organic solvents along with surfactants and reducing or oxidizing agents is prepared at temperatures close to room temperature (RT) and subsequently heated. The heating can be conducted under protective atmosphere or in air. Crystallization occurs at elevated temperatures. Nanoparticles grow at even higher temperatures by addition of monomers to existing crystals. To ensure a narrow size distribution, the chemicals (precursor, surfactant, solvent) need to ensure a rapid generation of large quantities of nucleation seeds in a narrow time window, when the supersaturation of monomers is reached. Monomers are not necessarily the starting precursor compounds but rather compounds formed *in situ* e.g. an intermediate between $Fe(OA)_3$ complex and iron oxide nanocrystals act as monomers.[34] The starting material defines the temperature and speed of the monomer formation during the reaction. Affinity of surfactants towards the nanocrystal surfaces directly influences the surface energy of the particle. Strongly binding surfactants lower the surface energy and promote the formation of small particles while weakly binding surfactants lead to larger particles.

Following the kinetic model of the LaMer, more and more monomers will form during the heating process and gradually the monomers concentration increases. When an oversaturation of monomers is achieved, nucleation starts and crystallites form. This reduces the concentration of monomers almost instantaneously. The growth of existing crystals is favored compared to the formation of new seeds. The monomer concentration drops subsequently. This decrease in concentration is slower with time because fewer monomers in solution take more time to “find” nuclei to attach to.

Figure 9 A illustrates the three states of the LaMer model. In stage I the monomer concentration is rises over a certain period until it reaches a saturation concentration c_s and nucleation occurs. These small nuclei are unstable and can dissolve again. Further formation of monomers will increase the concentration to critical levels c_c and stable particle seeds abruptly form in solution, reducing the monomer concentration (“burst of nucleation” - step II). In step III the seed sprout by addition of remaining monomers. The growth (II) and generation (III) of the seeds are separated regarding time. This grants a narrow size distribution of the final particles.[3]

Figure 9 B plots the overall free energy of the heterogeneous nucleation process ΔG_T (equation 8), which is the sum of the free surface energy ΔG_S (equation 6) and the free bulk energy ΔG_B (equation 7). Since interfaces between different phases (solid and liquid) require lots of energy the free surface energy ΔG_S increases with the particle radius and causes nuclei to dissolve again to minimize the surface. The free bulk energy ΔG_B decreases with the particle radius. ΔG_S and ΔG_B grow with r to the power of 2 and 3, respectively, it results in a maximum of ΔG_T at a critical particle radius r_c above which the particles are stable against disintegration.[35]

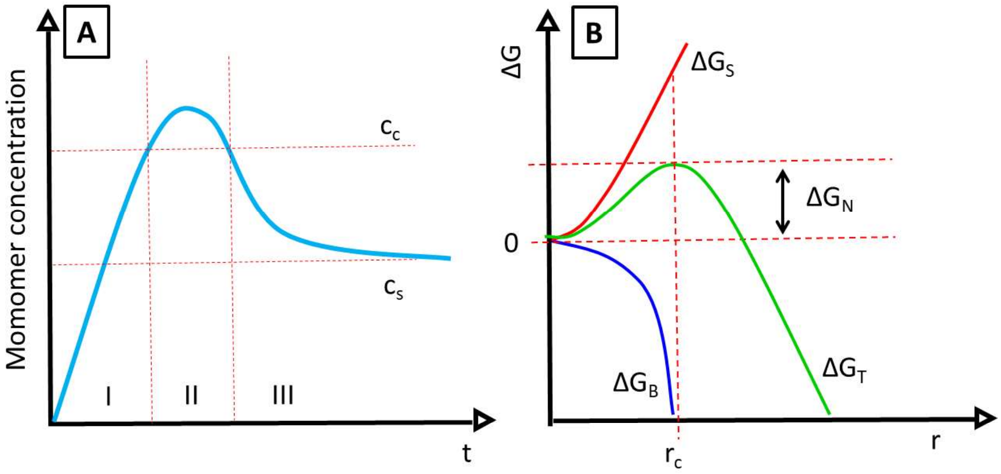

Figure 9: (A) Three stages of the LaMer model. (B) Classical heterogeneous nucleation theory of spherical particles.

Those energies are:

$$\Delta G_S = 4\pi r^2 \gamma \qquad (6)$$

$$\Delta G_B = \left(\frac{4\pi r^3}{3}\right)\Delta G_V \qquad (7)$$

Here, r is the radius of the nucleus and γ is the surface energy of the new phase while ΔG_V is the free Gibbs energy per volume, which is written as:

$$\boldsymbol{\Delta G_V = -\left(\frac{RT}{V_M}\right)\ln S}$$

The total free energy therefore is defined as:

$$\boldsymbol{\Delta G_T = \Delta G_S + \Delta G_B = -\frac{4\pi r^3 RT\ln S}{3V_M} + 4\pi r^2\gamma} \qquad \textbf{(8)}$$

The critical radius is a function of the surface energy γ, the oversaturation S and the volume of a monomer V_M and the temperature T: It is defined as the maximum of ΔG_T.

$$\boldsymbol{\frac{d\Delta G_T(r)}{dr} = 0} \qquad \textbf{(9)}$$

$$\boldsymbol{r_C = \frac{2\gamma V_M}{RT\ln S}} \qquad \textbf{(10)}$$

The formation of nanoparticles can be viewed as a dynamic process in which small particles form and dissolve again. When the temperature and number of monomers are high enough there is a high chance that many particles reach the critical radius. This is the burst of nucleation. The exact nucleation mechanism is still center of research and not fully understood.

Ligands and ligand exchange

Nanoparticles have a high surface to volume ratio that is responsible for most of the physical properties and chemical reactivity. The high energy surface is usually covered with molecules from the synthesis that bind to the particle surface. These surfactants have a large influence on the particles properties like dispersibility, optical properties and magnetic behavior. In addition, surfactants block any other molecules from interacting with e.g. catalytically active surface sites.

Synthesis in high boiling solvents leads to particles that usually carry large nonpolar hydrophobic ligands with long aliphatic chains and functional binding groups. Popular surfactants are oleic acid (OA), oleylamine (OAm) and 11-mecaptoundecanone. For use in dyes or in biomedical applications, the particles need to be dispersible in water.

In general, there are two methods available to change solubility. Using an excess of amphiphilic compounds will lead to the formation of a double layer system around the particle. The hydrophobic parts of the amphiphilic molecules hold on to the hydrophobic surfactants by Van der Waal interactions.[36] In this micelle, the interaction between surface ligands is rather weak. The double layer can easily be destroyed, leading to an agglomeration of the hydrophobic particles in the polar solution. Furthermore, the thickness of the organic shell of the NP increases, which hinders interparticle interactions.[37]

If a surfactant molecule with higher affinity towards the metal of the nanoparticle is used, it will substitute a great percentage of other surfactants but will circumvent a second substitution step as a consequence. Other compounds react with surfactants and substitute them. As an example, nitrosonium tetrafluoroborate ($NOBF_4$) is able to “wash” off ligands form from CdSe quantum dots, TiO_2 rods and Fe_3O_4 spheres.[38] In any case, BF_4^- is introduced as a new, weaker bound surface molecule. Aqueous NP-BF_4 solutions were even more stable than the hydrophobic particles in unipolar solvents. In a second step, other surfactant molecules or polymers can substitute BF_4^- on iron oxide NP. Because size and morphology were conserved in all these ligand exchange experiments, a change in blocking temperature could directly be contributed to interparticle distances. BF_4^- -ligands shorten distances between particles and result in stronger magnetic dipole-dipole interactions, leading to longer magnetic relaxation times.[39]

Inspired by the adhesive proteins found in mussel-fibers, DOPA (3,4-dihydroxyphenylalanine) has become a popular molecule in surface functionalization chemistry. The protein allows the mussel to hold on to almost any surface under water and even remain bound in dry conditions.[40,41] DOPA is a non-essential amino acid and is present in large quantities from 3-30 mole% in adhesive mussel proteins. Mussel adhesive protein is known to bind to all kinds of surfaces like metals, metal oxides and even PTFE.[42] Besides its function as an anchor, it also serves as a cross-linker when oxidized to the respective semiquinone or quinone. Oxidation can be tracked with NMR- and UV-VIS-spectroscopy by observing the signals of aromatic protons and characteristic absorption bands for aromatic systems respectively.[43] When catechol is oxidized, aromaticity is lost. The relevant part of the DOPA amino acid is the catechol group. Catechols are diphenols with two hydroxyl groups in *ortho* position. They are common in nature and appear in a variety of plants and plant derived products (**Figure 10** (2)). Dopamine has been reported to dissolve particles after functionalization. This is explained with the formation of a ring inside the surfactant molecule that weakens the binding to the metal.[44] Even though this decreases the long-term stability of functionalized NPs, dopamine remains a popular ligand for establishing soluble particle systems.

Figure 10 (3,4,5) shows some possible chemical reactions of catechol. Oxidation (**Figure 10** (3)) in high pH conditions will lead to the quinone that can react with adjacent oxidized catechols in an aryl-aryl coupling (**Figure 10** (4)). Products of such polymerization-reactions are insoluble polymers. Additional functional groups on the aromatic ring, such as nitro (-NO_2) groups which have strong electron-withdrawing properties, will not only increase the acidity of the hydroxyl groups but will also reduce the reducing effect of the catechol (**Figure 10** (5)). Catechol has high affinity towards ferric iron (Fe^{3+}) (**Figure 10** (6)) while catechols with electron withdrawing functional groups (like nitrocatechol) have strong affinity towards ferrous ions (Fe^{2+}). The metal is oxidized to ferric iron and the electron will be delocalized over the nitroaryl molecule.[45] The self-polymerizing properties due to oxidation and the strong binding to almost any surface made catechol (DOPA) a key anchor for surface modification. Antibacterial surface coatings have been developed by using catechol anchors on the surface as initiators for polymer coatings. Protective layers of up to 100 nm thickness provide anti-fouling behavior.[42] Alternating layer systems of iron oxide nanoparticles with catechol carrying polymers have been prepared to make extremely hard and robust materials.[46,47] The polymer infiltrated the particle layers and formed a stable composite analogue to the mussel protein that uses iron as crosslinking hub.[48]

Catechol ligands are widely used for metal nanoparticle functionalization.[49] The bidentate binding of the two hydroxy groups of catechol provides strong surface binding and long particle lifetime in aqueous media. Often PEG with catechol units as functional groups on the polymer backbone or side chains lead to stable colloid solutions for biomedical applications.[50] There are numerous publications with varying size and composition of the particles and properties of catechol polymers to optimize particle properties. The overall result is that catechol provides good colloidal stability especially for particle compounds containing Fe^{3+}.[51]

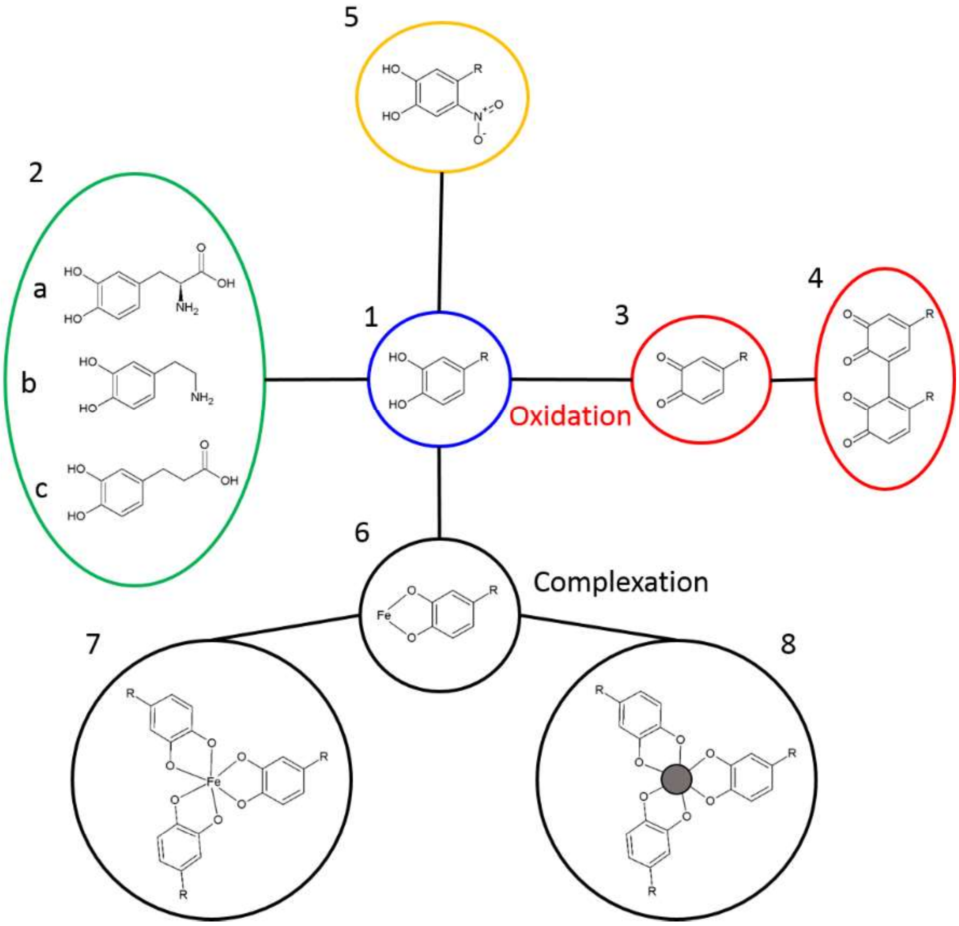

Figure 10: Exemplary reactions of catechol.

III. SPHERICAL IRON OXIDE PARTICLES

1. General effects on the synthesis of iron oxide NPs

Introduction

Sun *et al.* described the synthesis of iron oxide (Fe_xO; $0{,}6 \leq x \leq 0{,}75$) nanoparticles from iron acetylacetonate ($Fe(acac)_3$) in the presence of oleic acid (OA) and oleyl amine (OAm) in high boiling diphenyl ether.[52] OA and OAm are used as surfactants and stabilizers, and 1,2-hexadecane diol (HDD) was applied in the reaction as a reducing agent. Polyalcohols, and especially alkyl diols, are used to reduce metal ion precursors at elevated temperatures. The method, first described in 1986, is called polyol synthesis and is beneficial for the preparation of metal alloy particles like FePt, in which $Pt(acac)_2$ is reduced to Pt^0 by the diol.[53–5556] The exact reaction of this reagent is unclear. Due to adjacent hydroxyl groups, the diol can disintegrate to reducing species like CO and can also function as a surface ligand and block crystal faces. Compared to simple alcohols, diols are more efficient as reducing agents and colloid stabilizers because they have higher boiling points, which allow harsher reaction conditions. They strongly attach to metal ions due to the chelate effect and facilitate narrow size distributions.[22] The alkyl length of the diols has a critical influence on the solubility of the monomers, that form *in situ* and the final particle product in solution. It was found that longer hydrocarbon chains improve the stability.[57] In some cases the length of the diol influences the shape of metal particles like in the case of Pt multipods.[58] Christopher *et al.* further analyzed the synthetic method for cobalt iron oxide nanoparticles developed by Sun *et al.*[59] They varied reaction parameters, like 1,2-hexadecandiol (HDD) to metal and OA to OAm ratios, to analyze the effect of these compounds on the yield, size and size distribution of the formed particles. A strong influence of HDD on the size and size distribution could be observed. Without HDD the narrowest distribution could be achieved. Interestingly, the average particle diameter was close to that of reactions with a HDD to metal ratio of 5 to 1. With increasing HDD share the particle size increased linearly. This indicates that small amounts of HDD assist in the formation of nucleation clusters, which leads to smaller particles.[60] Larger particle diameter in absence of HDD is also reported for FeOx and NiPt particles.[35,61]

Oleyl amine (OAm) and oleic acid (OA) are widely used as surface stabilizing agents. The common conception is that upon decomposition of metal precursors, like $Fe(CO)_5$ and $Fe(acac)_3$ in the presence of OA, the metal oleate complex is formed *in situ,* and leads to the formation of monomers that form the nanoparticles.[62] If HDD is present, particles will form even without the surfactants OA and OAm. Stable dispersions of hydrophobic particles are obtained because HDD serves as a weaker surface stabilizer. In polar solvents additional amphiphilic molecules, like OA and OAm, can create double-layers with existing hydrophobic surface ligands. This results in water-soluble particles.[36] The absence of OAm gives very little yield while OA was found to have strong influence on the shape of the particles.[35,60] Both ligands can also serve as a reducing agents in reactions under harsh conditions.[63] Other works emphasize the importance of high OA to OAm, as well as high OA to precursor ratios for the formation of anisotropic particles in similar reactions.[643,65] Additional cations of the carboxylates also determine particle morphologies.[15,19]

In this work 1,2-hexadecandiole was replaced with cheaper 1,2-tetradecandiole (TDD) which has a shorter hydrocarbon-chain ($C_{14}H_{30}O_2$). The reaction was done in benzyl ether or phenyl ether. The particle diameter varies due to the higher boiling point of benzyl ether compared to phenyl ether.[59] This was done to determine the optimal particle size for later experiments.

Preparation

Iron oxide particles were synthesized by a modified method reported by Sun *et al.*. Decomposition of iron(III) acetyl acetonate in phenyl ether and benzyl ether in the presence of 1,2-hexadecandiole or 1,2-tetradecandiole, oleic acid and oleyl amine caused the formation of monodisperse NPs.[52]

Results and Discussion

Figure 11 shows TEM images of particles synthesized in diphenyl ether (PE) and benzyl ether (BE) next to their respective distribution of particle diameters. Particles from PE have a narrow distribution and an average diameter of 5 nm compared to the particles from BE, which have around 7 nm. This may arise from the higher reaction temperatures and the different coordination of the solvent molecules to the particles and the monomers. A broader distribution usually originates from a broader time in which the nucleation clusters are formed, according to LaMer's model.[34] Moreover, higher temperatures favor Ostwald ripening, which dissolves smaller particles and grows larger ones. Both preparation methods result in particles covered with hydrophobic ligands that prevent agglomeration and grant a more or less constant interparticle separation. This allows an easy arrangement into close packed assemblies if the size distribution is narrow. To analyze the surface ligands, an elemental analysis was performed. This analysis of dried particle samples showed 0 % N_2 (see **Table 4**), which leads to the conclusion that only OA covers the surface of the particles. This is expected, considering the high affinity of oxygen towards iron. Furthermore, it indicates that the amine OAm merely functions as a base to deprotonate OA, which plays the main part in stabilizing the monomers and particles. (A) and (B) in **Figure 11** shows the magnetic behavior as a function of temperature and external field, respectively. Smaller particles exhibit a lower blocking temperature (taken from the maximum of the ZFC curve) as expected. The broad size distribution from the particles prepared in BE is recognizable in the magnetic behavior as well. The ZFC does not show a sharp drop but a broad maximum. Interestingly, the magnetization at three Tesla (3 T) is almost equal for both samples (**Figure 11**). Usually a dependence of the magnetization on the particle dimension is expected.[66] With smaller particle diameter, the saturation magnetization should decrease. This is because of a shell of canted (or strongly interacting) spins forms the outer layer of a particle and thereby reduces the magnetization of the core, which is estimated to have bulk properties.[67] As a consequence of this, saturation magnetization levels of nanoparticles are usually lower than their bulk counterpart.[68] Here the similar magnetization at high fields can be explained with the different solvent. The solvent BE can disintegrate at high temperatures. Products of the disintegration bind to the surface, which influences the overall magnetic behavior.[69] Another possibility would be that the larger particles exhibit higher surface defect density due to the preparation at higher temperatures.

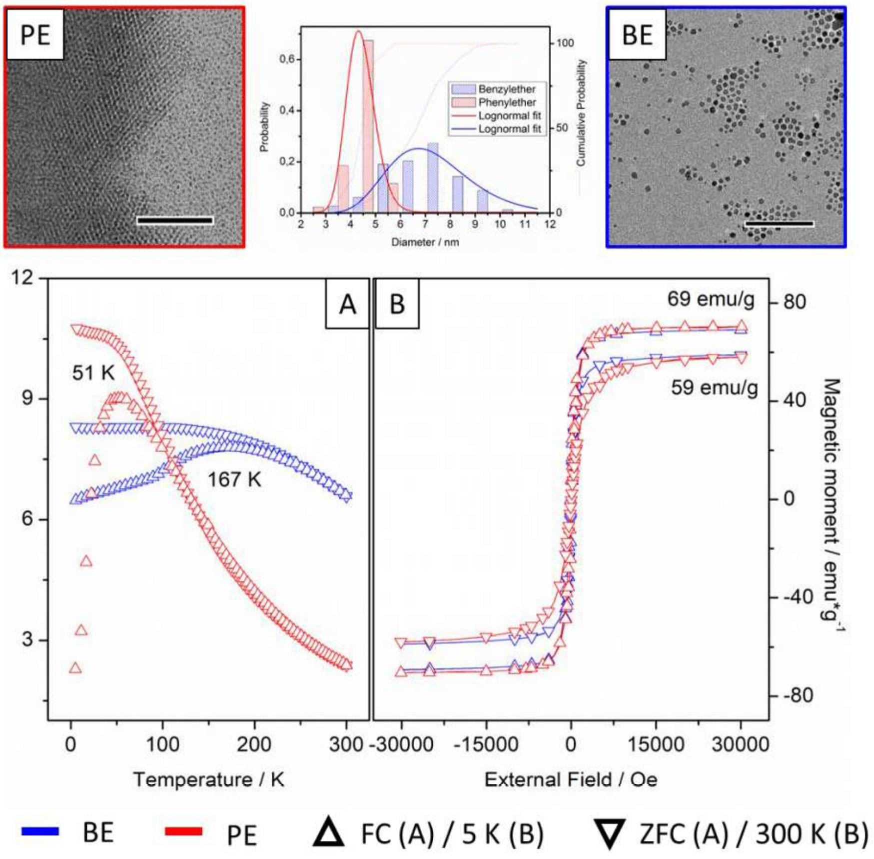

Figure 11: TEM images showing the size distribution of magnetic iron oxide particles prepared in benzyl ether BE (blue) and phenyl ether PE (red). The scalebar of the TEM images is 100 nm in both cases. A) Magnetization vs. temperature and B) magnetization vs. external magnetic field. T_{max} of both ZFC as well as M_{max} at 3 T (30,000 Oe) are marked.

To investigate the influence of the reducing diol, a Mössbauer analysis was performed with samples prepared with a fivefold molar excess of HDD and TDD compared to Fe(acac)$_3$ in BE. **Figure 12** shows Mössbauer spectra and TEM images of the particles. Mössbauer analysis shows that both samples are maghemite (γ-Fe_2O_3) with similar magnetic behavior. TEM images reveal spherical morphology of both particle batches. The size distribution of particles made with TDD is slightly larger compared to that of the HDD sample. The average sizes are 4 nm and 5 nm for the HDD and TDD samples, respectively. However the deviation is around 1 nm for both batches. The difference lies within the error as only 200 particles were used for the statistic. In essence, iron oxide particles could be synthesized with the same molar amount of a diol for less than half the price of HDD.

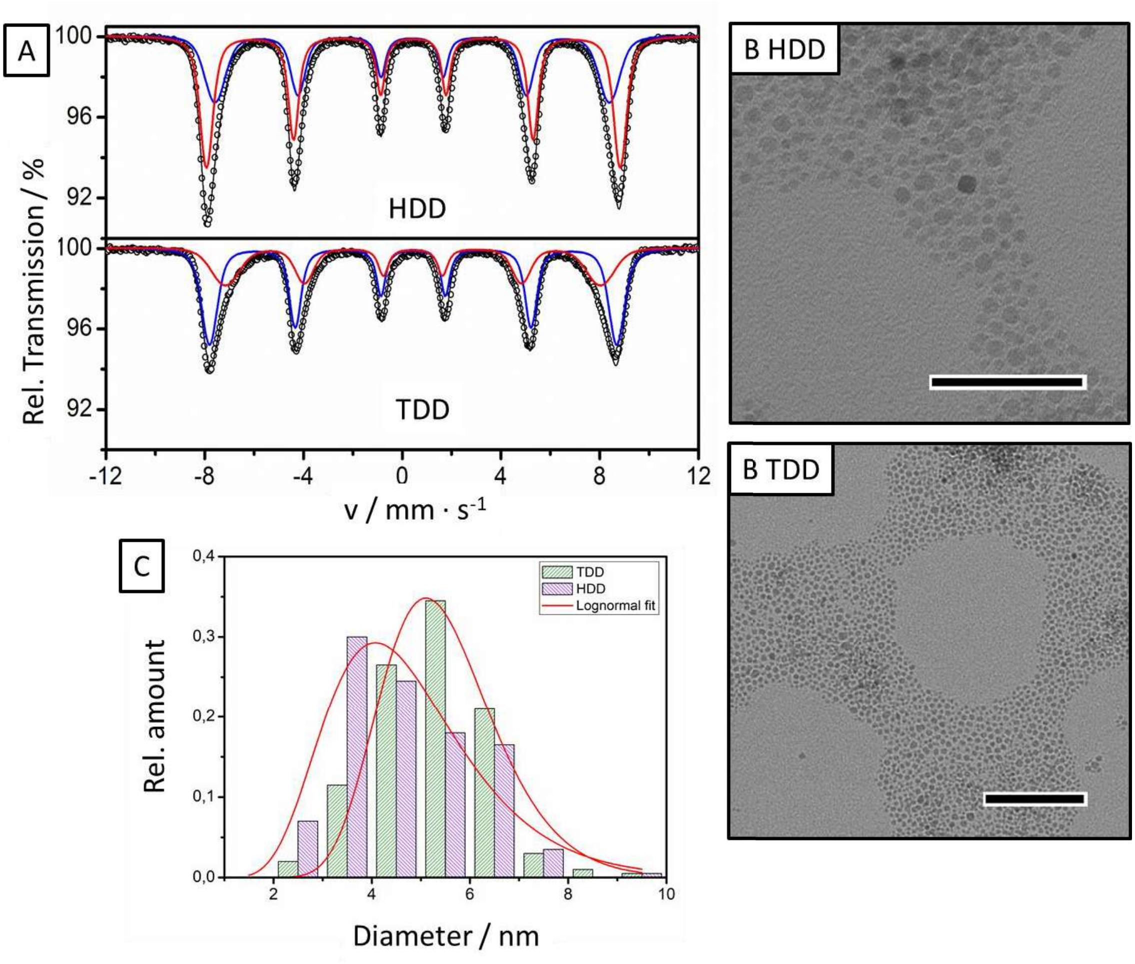

Figure 12: Mössbauer spectra of particles prepared with HDD, and TDD show no differences. TEM images show the resemblance of HDD and TDD samples (scalebar equals 50 nm for HDD and 100 nm and TDD).

The complete lack of TDD still leads to spherical, magnetic particles of similar size, size distribution and composition. **Figure 13** shows particles prepared in BE with and without diol. It was observed that the particles generated without TDD did precipitate in shorter time than the control group. This observation confirms that TDD functions in the same way as HDD as a surface ligand and stabilizes the particles even in the presence of OA, but has no influence on the size, size distribution and shape of the particles as seen in TEM images. As mentioned above the small difference in average size is negligible and lies within the range of error of the measurement.

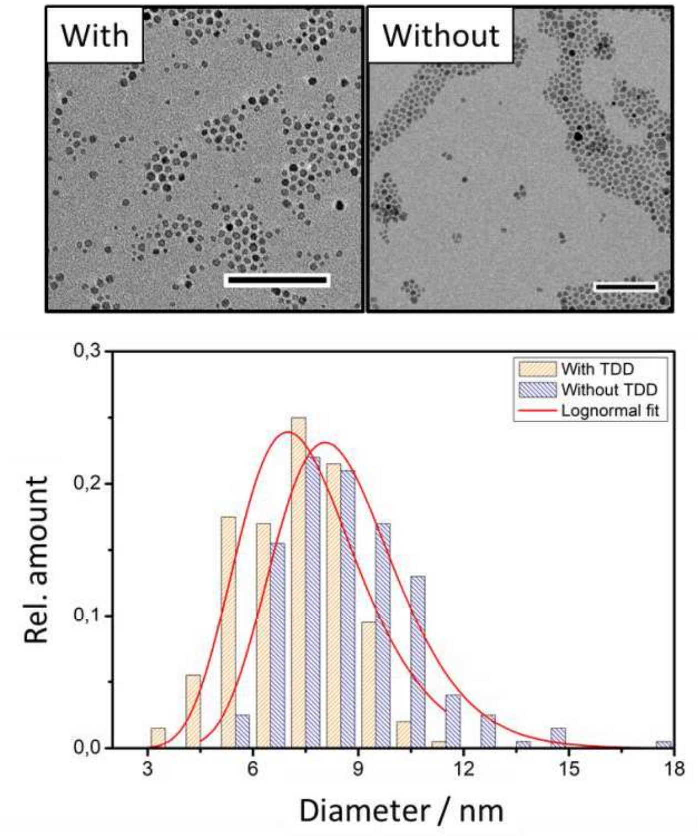

Figure 13: Nanoparticle synthesis with and without TDD in BE. Scalebar equals 100 nm.

In conclusion, although there are numerous publications on tunable size and shapes of nanoparticles, the majority of the research currently being conducted is geared towards their applications, despite the incomplete understanding of the basic chemistry underlying nanoparticle synthesis. There is still no full explanation of why the reactions lead to monodisperse nanoparticles of a certain composition. In particular, the effect and use of reducing agents, such as HDD and TDD, remains vague. This work shows that particles prepared without diol will not stay stable in dispersions as long as the particles are prepared with diol. The expensive HDD can be replaced with TDD. This drastically reduces the costs of the synthesis. The chemical behavior of reducing agents and solvents also influences the surface properties of the particles and intrinsic properties like magnetism. Since every reaction is unique and can lead to small differences, it is hard to distinguish between effects of chemicals or random deviations of each batch.

2. Reduction of particles due to functionalization with PDAm polymer

The following project was done in cooperation with [redacted] who carried out the Mössbauer measurements and data interpretation, as well as magnetization data collection. [redacted] assisted in X-ray powder diffraction measurements and data interpretation, and [redacted] performed the x-ray photoelectron spectroscopy (XPS). The polymer PDAm was prepared by [redacted]

Introduction

This work follows prior experiments on nanoparticle polymer Bragg-stacks, which were done in part by [redacted] a former member of the Tremel research team. Iron oxide nanoparticles and catechol carrying polymer were spin-coated in alternating order onto glass or silica substrates. It was observed that the magnetic behavior of these stacks strongly depends on the last nanoparticle layer only. When the stack was last covered with polymer the behavior drastically changed. This effect seemed to be independent on the number of layers, which led to the conclusion that the effect must originate from the polymer-nanoparticle interactions. This realization spawned several experiments, including new layered systems and the hybrid compounds described in this chapter.

Preparation

The spherical magnetic iron oxide particles were prepared by thermal decomposition of metal complex precursors, as described above.[52] Three different hybrid samples were made by covering particles with diverse surface ligands in different polymer matrices. **Figure 14** highlights the different samples, the corresponding surfactants, and matrix polymers. All samples were prepared inside a Mössbauer sample holder, a small polymer cup of 1 cm diameter with a volume of approximately 0.4 mL. Each sample contained 10 mg of particles and 100 mg of matrix polymer. For sample one (1) the prepared particles (with OA) were embedded in poly methyl methacrylate (PMMA) with an average mass of $M_w = 35{,}000$ g/mol. This was done by mixing the particles in diluted polymer in very little solvent. For the second sample (2) 3,4-dihydroxy-hydrocinamic acid (DHCA) functionalized particles were enclosed in PMMA. The ligand exchange is described in experimental part. The third sample (3) contains OA capped particles in a poly dopamine acrylate (PDAm) matrix. PDAm was synthesized by a method developed by Theato *et al.* (**Figure 54**), by production of an active ester pentafluorophenylacrylate (PFA) that was later polymerized via RAFT polymerization to create polypentafluoroacrylate (PPFA). In a polymer analogue reaction, pentafluorophenyl was substituted by dopamine groups leading to the final catechol carrying polymer PDAm. It should be noted that the ligand exchange was done without prior TMAH treatment and is therefore considered to be an incomplete substitution, with OA still present on the surface. This is indicated schematically as remaining OA ligand on the particle in **Figure 14**.

OA was substituted by DHCA in THF. Hydrophobic particles, as well as DHCA are dispersible and soluble in THF. The particles were collected using a magnet and washed several times with ethanol to remove unbound ligand molecules. The substitution was verified via FTIR spectroscopy and TEM.

For XPS (X-ray photoelectron spectroscopy) a sample of NP in PDAm was prepared in solution and dried on a gold-sputtered glass substrate.

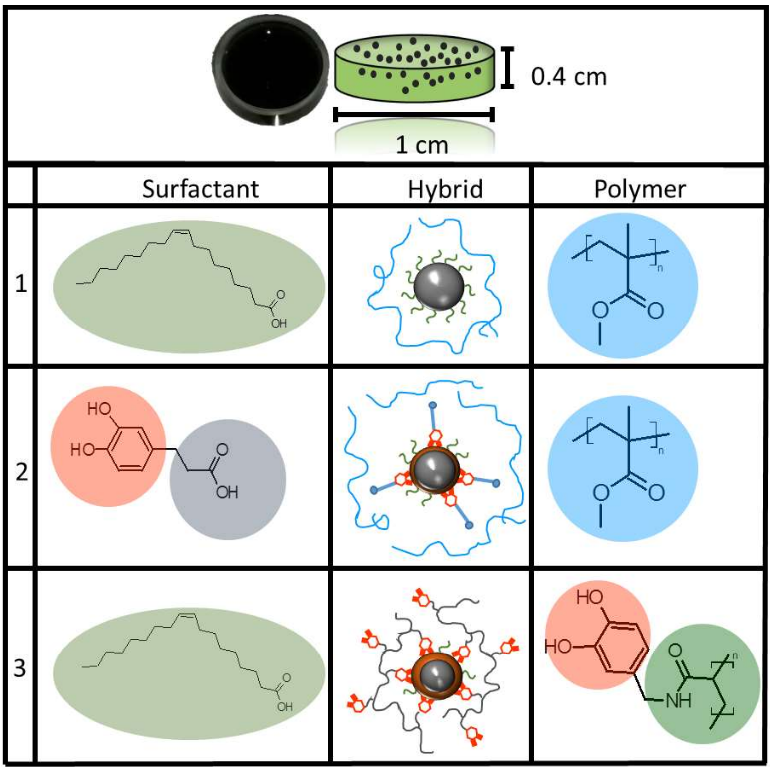

Figure 14: Top picture shows Mössbauer sample holder. The scheme illustrates the three samples prepared for the experiment. 1: OA capped NP in PMMA. 2: DHCA capped NP in PMMA. 3: OA capped NP in PDAm.

Results and discussion

Figure 16 shows TEM images of the pure particles with OA. The ligand prevents the particles from agglomerating and forces the particles into an almost closest packed hexagonal arrangement in 2D, with almost constant distance between particles. The size distribution shows a maximum at 7 nm, which is also the average diameter $d_{av} = 7 \pm 2$ nm, and ranges from 3 nm to 10 nm. The results of the lognormal fit are listed in **Table 10** in the appendix. **Figure 15** shows TEM images of the polymer functionalized NP. The particles are not freely distributed anymore because the polymer covers the particles and strongly connects them together. In the TEM images polymer appears as large areas without define shape and with low contrast compared to NP.

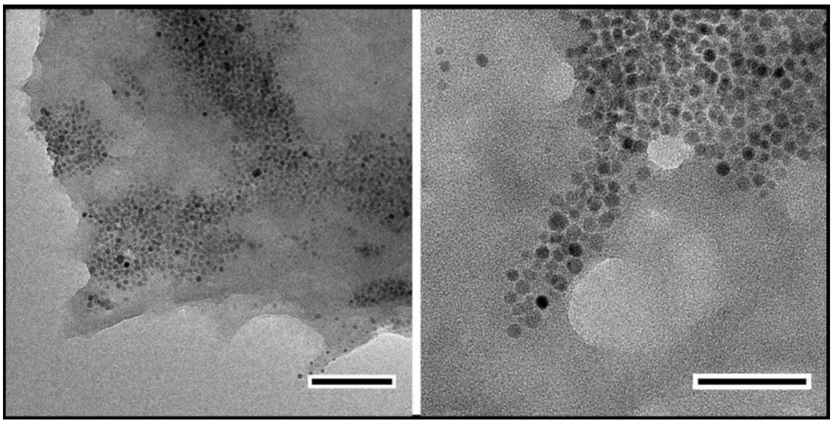

Figure 15: TEM images of NP functionalized with PDAm in solution for XPS measurements. Scalebar equals 100 nm and 50 nm for the left and right image respectively.

Magnetization of the particle powder was measured at 100 Oe as a function of temperature. The ZFC curve reaches its maximum T_{max} at 57 K which is set as the blocking temperature (T_B) of the sample and is also shown in **Figure 16**. This value for T_B is in the expected temperature range for the corresponding particle size.[70] The magnetization as a function of the applied field shows no hysteresis at 300 K, showing that the particles were superparamagnetic, as expected for particles of that small size.[32] The saturation magnetization M_s at 50,000 Oe (5 T) was 59 emu/g which is lower than M_s for bulk maghemite (83.5 emu/g) and magnetite (92 emu/g).[71] The superparamagnetic nature of the NP powder was further confirmed in Mössbauer experiments (**Figure 16** C). Thermal fluctuation of the magnetic moment (Brownian and Néel relaxation) is faster than the measurement time of the Mössbauer experiment. The average magnetic moment of the sample is zero, this causes one broad peak to appear as an average value above T_B at 293 K.[72] The broad peak is a single doublet with $\delta = 0.35 \pm 1$ mm·s^{-1} and $\Delta E_Q = 0.71 \pm 2$ mm·s^{-1}, indicating a high-spin state of trivalent iron. At helium temperatures (4 K), the signal splits up into a sextet characteristic for maghemite (γ-Fe_2O_3).[73]

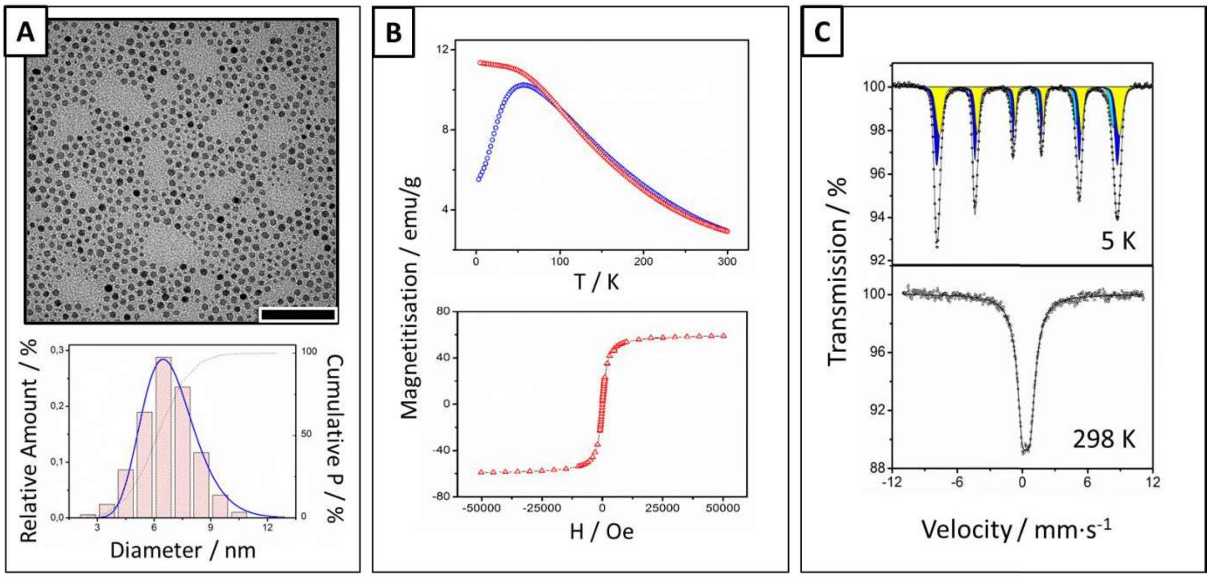

Figure 16: (A) TEM image and size distribution of prepared OA functionalized NPs. (B) Magnetization as a function of temperature (top) at 100 Oe and external field (bottom) at 5 K. (C) Mössbauer spectra at 4 K (top) and room temperature (bottom).

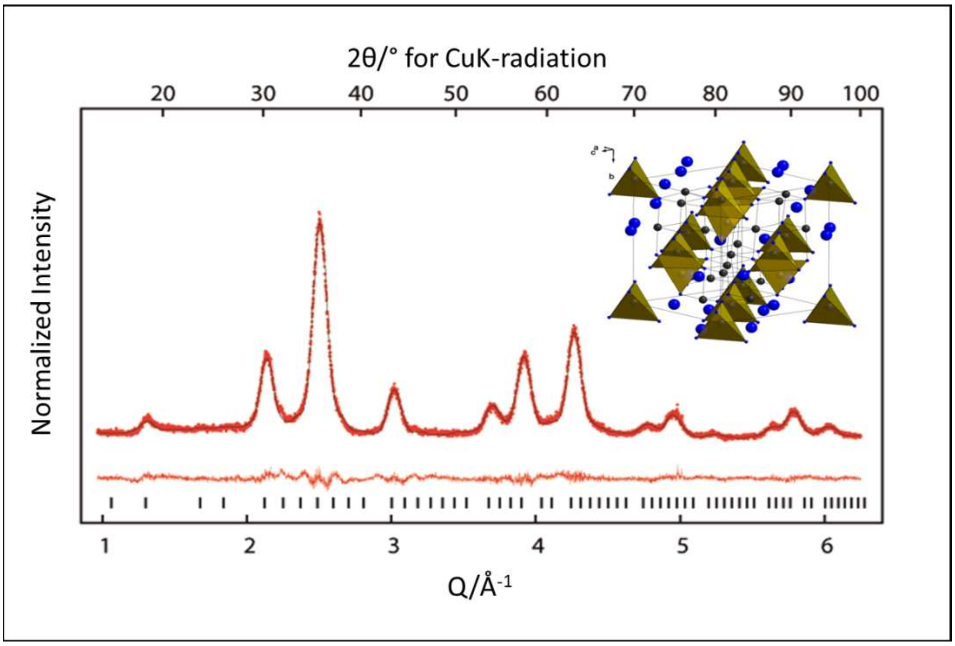

Figure 17: Powder XRD pattern of the dried NP with OA.

Full pattern profile analysis ("Rietveld refinement") of the powder diffraction data identified the iron oxide phase as maghemite (**Figure 17**). The average crystallite size was determined to be 7 nm, which is in agreement with the average particle size observed with electron microscopy.

The ligand exchange with DHCA was verified by FTIR spectroscopy, as shown in **Figure 18** together with a TEM image of DHCA capped NPs (C). Morphology and size did not change during the ligand exchange reaction. A clear sign of new surface functionalization is the formation of agglomerates of the particles in ethanol. The catechol group of DHCA will bind most likely to the iron (III) surface ions. The carboxylic group of DHCA then forms the outer surface of the particle. Formation of hydrogen bonds causing strong interparticle interaction and results in the formation of agglomerates in ethanol. The FTIR spectrum shows strong bands around 2800-3000 cm^{-1} from C-H stretching vibrations.[74] The bands at 1400 cm^{-1} and 1600 cm^{-1}, marked (c) and (e) for the OA capped NP, belong to oleic acid.[75] C=O stretch vibrations from OA at 1700 cm^{-1} are very weak but broad, resulting from interactions with surface ions. The main differences are two bands at 1265 cm^{-1} and 1487 cm^{-1} that are only visible after the ligand exchange and correspond to C-O stretching of phenolic groups and -C=C- ring vibrations, overlapping with $-CH_2$ scissoring vibrations, respectively.[76] These bands correspond to aryl C-O stretching modes and aromatic vibrations, respectively.[77] There are still less intense bands that can be assigned to OA. This indicates that the ligand exchange is not complete and only a fraction of the OA groups have been replaced by DHCA as a consequence of steric effects or repulsive interactions between the bound OA and free DHCA. No characteristic Fe-O vibration modes (around 580 cm^{-1}) could be observed because data could only be collected from 650 to 4000 cm^{-1}.[78]

TGA data of both samples show a similar loss of mass with time at constant heating rate. **Figure 18** B shows the function of relative mass against the temperature. It reveals several steps, and the $dm_{rel}(T)/dT$ signal indicates temperatures of mass loss as minima of the function. The first small step can be assigned to the vaporization of physically adsorbed water (between 100 °C and 200 °C).[79] The second and third steps appear between 200 °C and 450 °C and may originate from the evaporation of chemically adsorbed water and the decomposition of the organic ligands, respectively.[79,80] The first minimum in $dm_{rel}(T)/dT$ signal is almost identical in both samples, while the second weight loss is different by around 50 °C. Assuming that all ligands were removed completely, at 500 °C the difference in mass is around 2 %. Thus OA and DHCA (OA) constitute approximately 15 % and 17 % of the total particle mass. This value is taken into account later for calculating the magnetization of NPs inside the polymer matrix. The last drop in weight might be a reducing process. At high temperatures carbon remains from the ligands reduce the iron oxide NP. TGA is a very good method to analyze the number of ligand molecules on nanoparticles quantitatively, provided that only one type of ligand is present. With the known molar mass the number of moles of surfactant can be calculated. It should be mentioned that the quality of the measurement is depending on the total mass of sample used, the heating rate and preheating times. More mass per sample will automatically lead to longer decomposition times over a broader temperature range. In worst case scenarios, the maximum temperature is reached with “unburned” compound remaining in the sample holder. All samples of this work have been measured with the same heating rate, but because the sample is decomposed in the process the amount is limited to the stock available. All samples were between 2 and 8 mg. In some cases no plateau of "constant" weight could be achieved.

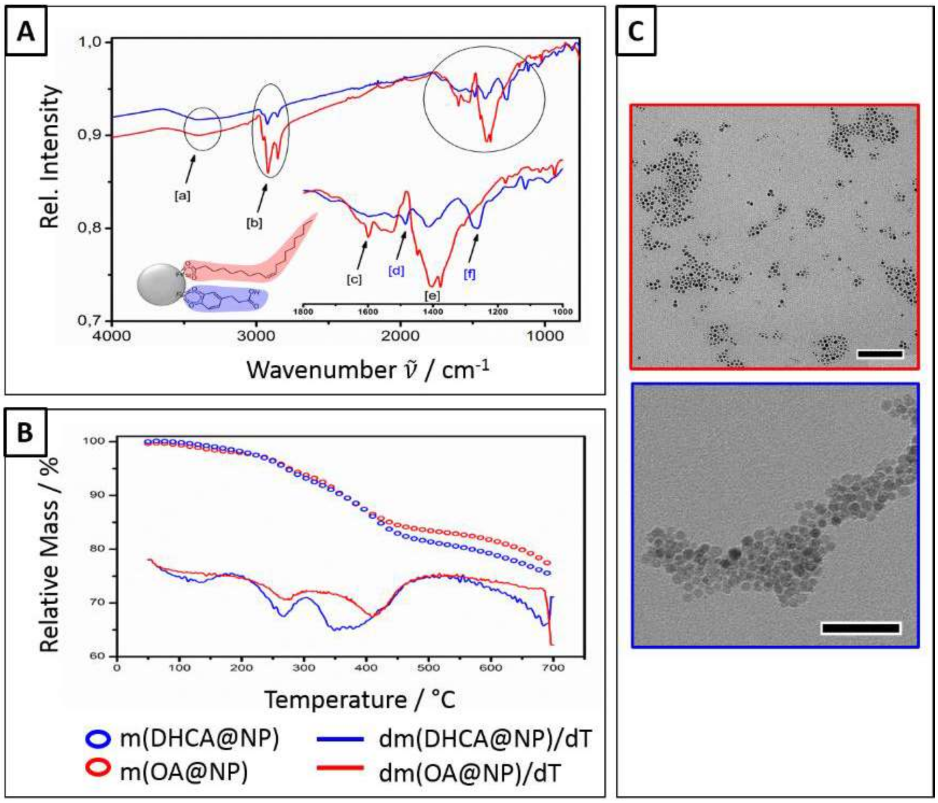

Figure 18: (A) ATR FTIR data of OA (red) and DHCA (blue) functionalized NP. (B) Thermogravimetric analysis of OA (red) and DHCA (blue) particles under N_2. (C) TEM images of NPs befor and after the exchange recation.

In magnetic measurements, the particles inside the respective matrix exhibited different magnetic behavior. The saturation magnetization M_{sat} (at 3 T = 30,000 Oe) differs for the different polymer matrices for the OA capped powder sample. Taken into account the mass of ligand calculated by TGA, M_{sat} of particles in PDAm is roughly half the strength of the as prepared NPs, as powder or in PMMA. DHCA functionalized NPs only slightly differ from OA capped NPs. This indicates that the binding of the active catechol carrying polymer has a strong effect on the magnetization properties of the particles. At first this seems unusual because a similar effect was expected for the simple DHCA ligand. The key seems to be the way the particles are functionalized. DHCA is added to NP dispersed in THF, while PDAm is best soluble in DMA. The solvent seems to have a significant effect on the catechol-NP interaction.

Taking the average blocking temperature (T_B) as the value when ZFC curve passes its maximum (T_{max}), then T_B does not differ much for the different cases. The blocking temperature strongly depends on particle size and shape distributions, cooling rate and applied field during the measurement, as well as the measuring speed.[81] Additionally, interparticle interactions, mostly of magnetic dipole-dipole interactions, which correlate with the distance between particles, influence T_B. T_B drops with increasing distance indicating fewer dipole-dipole interactions.[8283] Since no significant change in T_B is observed for the polymer NP hybrids, significant changes in magnetic dipole-dipole exchange interactions between particles can be excluded. Taking into account the close packing of DHCA functionalized particles (see **Figure 18**), a similar distance is suggested in all other compounds and the dry particle powder. The temperature at which ZFC and FC curve coincide is the irreversible or branching temperature T_{irr}. In ideal non-interacting particles T_{max} and T_{irr} are equal. Distributions in size and shape as well as interactions between particles cause T_{irr} and T_{max} to separate. **Table 11** lists all the extracted temperatures from the M vs T measurements. T_{irr} decreases from sample 1 to 3, with pure NP exhibiting even higher T_{irr} than sample 1. Analyzing this trend the irreversible temperature decreases from free particles to embedded particles with long OA ligands to embedded particles with short DHCA ligands to PDAm encapsulated NPs. This trend probably represents the degree of fixation of NP from loose powder to a tight polymer matrix.

In theory single domain particles are magnetically saturated and all magnetic moments inside the NP are aligned.[84] Is was shown that the outer layer of the particles has randomly oriented magnetic moments, causing the saturation magnetization of nanoparticles to be lower than their bulk counterpart.[6871] The lowering of M_{sat} is thus explained by the formation of a reduced outer particle layer. This layer decreases the volume of the single-domain inner phase and has a magnetic moment opposite to the moment of the core. This concept was developed from the acquired Mössbauer data of all samples. Hyperfine magnetic fields on ^{57}Fe nuclei, corresponding to Fe^{3+} at tetrahedral and octahedral sites of maghemite, are distributed between 509 kOe and 517 kOe.[2] The Mössbauer spectrum of the particles embedded in PDAm is formed by two superimposed sextets with H_{hf} between 513 kOe and 520 kOe and a relative intensity of 84 %, a sextet with $H_{hf} = 477$ kOe and intensity of 12 % and a nonmagnetic doublet with 4 % intensity. The sextet with $H_{hf} = 447$ kOE is assigned to Fe^{2+} in octahedral sites of magnetite. The minor doublet arises from paramagnetic Fe^{3+} high spin (HS). This leads to the assumption that this doublet originates from the iron-catechol binding of surface ions. The two magnetic compounds in the Mössbauer spectrum hence correspond to two fractions – shell and core - of the NP. Starting from the Fe^{2+} and Fe^{3+} site population, the ratio of maghemite to magnetite was calculated to be 65 % to 35 % respectively. The net magnetization of the nanoparticles is a sum of

---

[2] The corresponding magnetic fields are calculated by a software that uses the measurement of iron foil with exactly known splitting and corresponding fields to determine the field of unknown iron samples.

core magnetization and magnetic moments on the surface. The reduction of the overall magnetic moment by functionalization with PDAm can be explained by the opposite moments of core ($3,3\ \mu_B \cdot 0,65 = 2,1\ \mu_B$) and surface ($4\ \mu_B * 0,35 = 1,4\ \mu_B$). The residual value can be estimated to be $\sim 0,7\ \mu_B$. The non-magnetic doublet in the Mössbauer spectra could possibly originate from smaller particles for which the opposing magnetic moment of the shell cancels out the entire moment of the core. Since size and morphology are conserved through the ligand exchange and T_B is nearly constant for every sample. The magnetic anisotropy constant *K* given by $T_B = K \cdot V_{NP}$ with V_{NP} as volume of the particle also stays unaltered. Alternatively, the randomization of magnetic moments similar to observations in ferrihydrite nanoparticles could offer an explanation for the decrease of M_{sat}.[85]

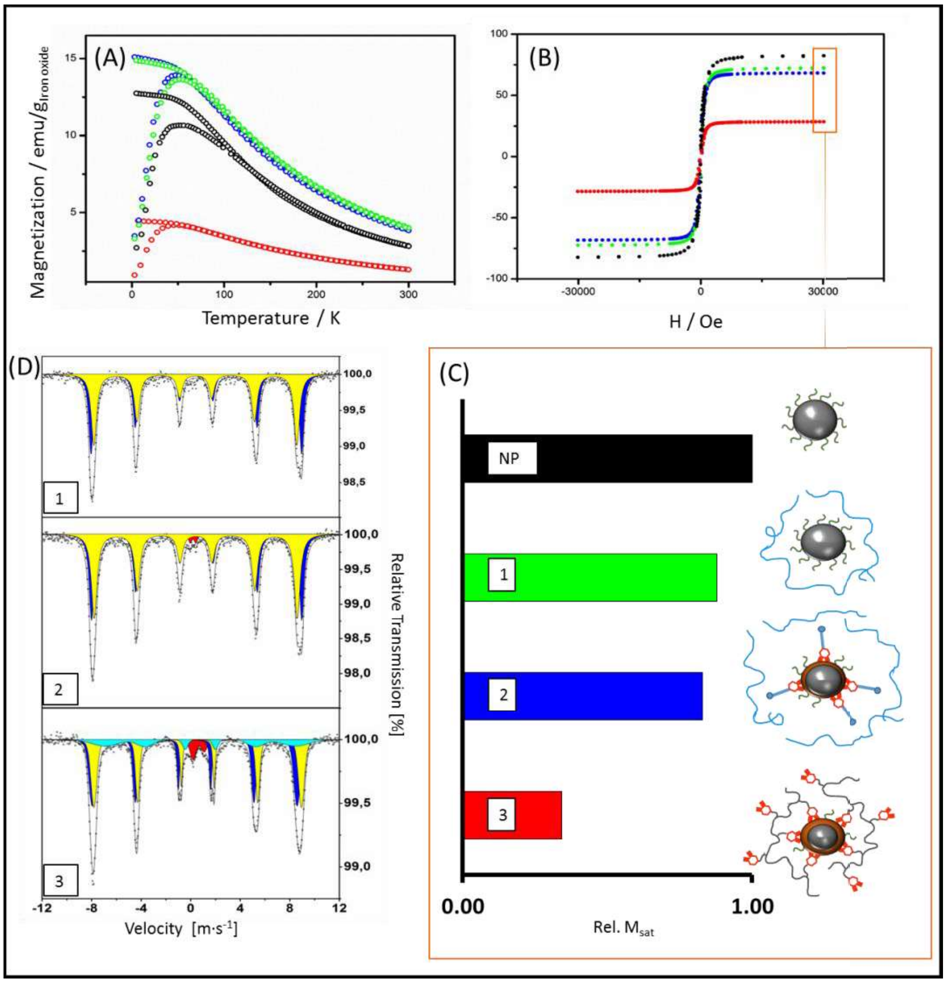

Figure 19: Graphs (A) and (B) show all collected magnetization data. The ZFC maxima T_{max} in (A) do not shift for the different hybrid systems. Magnetization as a function of field (B) shows similar behavior for all samples. The magnetization at 3 T visualizes the drop in net magnetization going from pure NP powder to PDAm enclosed NPs (C). Mössbauer data of all composite materials shows the increase in a nonmagnetic peak (red) following the same trend (D).

X-ray photon spectroscopy is an established method for chemical analysis. In this project it was used to verify the experimental data from Mössbauer and magnetization measurements by analyzing the oxidation state of iron. **Figure 20** displays the Fe 3p orbital energy for the different surface ligands. The spectra show drastic differences for samples (1) OA capped NP, (2) DHCA functionalized NP and (3) PDAm coated particles. The Fe 3p peak broadens from 1 to 3 indicating the presence of Fe^{2+} in samples 2 and 3 with increasing content while the Fe 3p peak of sample 1 only fits to Fe^{3+} species. As a confirmation of the binding of PDAm on the particle the N 1s peak only appears in sample 3 and corresponds to the nitrogen in the dopamine group (see **Figure 54** for the polymer structure). Given the fact that XPS is a surface sensitive method with only a few nanometers of penetration depth (~9 nm; $d \approx 3\lambda$) the Fe^{2+} peak strongly supports the statement of the magnetite layer formed by functionalization with catechol. Based on the Fe^{2+} to Fe^{3+} peak intensity ratio the Fe_3O_4 content in samples (2) and (3) is calculated to be 10 % and 33 % respectively. These data equal the contents worked out with Mössbauer spectroscopy. The particles are smaller in average ($d = 7$ nm) than the penetration depth of the X-ray photons. Therefore, the Mössbauer and XPS results are comparable. Based on the average radius $r = 3{,}5$ nm, the particle volume is $V = 179\ nm^3$. If approximately one third is reduced to magnetite on the surface, this layer would be around $d = 0{,}5$ nm in thickness.

Based on all these data it can be concluded that PDAm catechol reduces the outer layer of Fe^{3+} in maghemite to Fe^{2+}. Although the experiments do not give an explanation why the effect is strong in PDAm and rather insignificant for the pure catechol ligand DHCA, it establishes the power of ligands, not only on particle properties like solubility, but also on the magnetic behavior. PDAm reduces the magnetic moment by forming a core-shell type system The different functionalization conditions (one in THF and one in DMA) may lead to a stronger influence on the effect than expected. For future research a ligand system with opposite effect (increasing of magnetization) may be of interest.

Reduction of particles due to functionalization with PDAm polymer

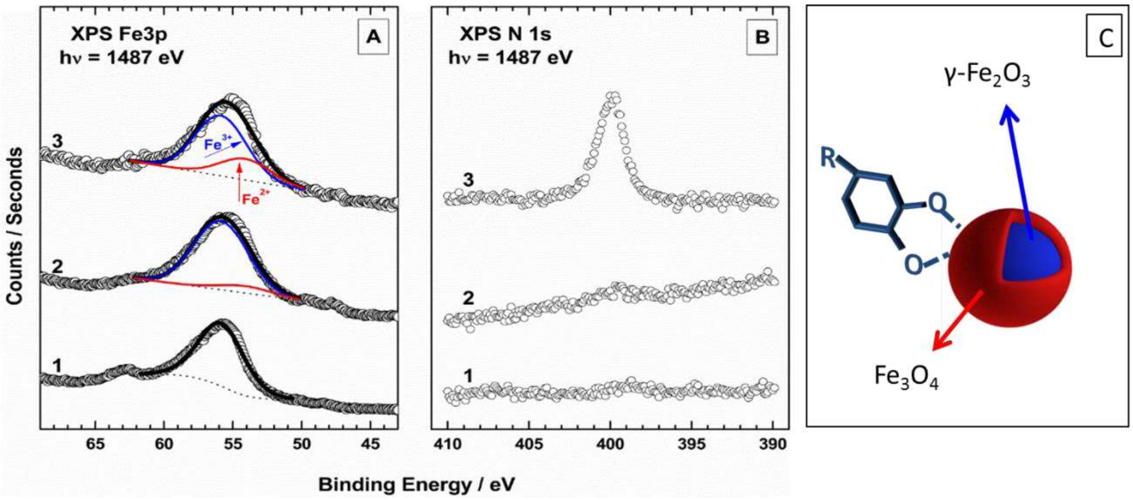

Figure 20: XPS spectra of Fe3p (A) and N1s (B) energy. (A) Shows the appearance of an Fe^{2+} band for DHCA capped NP (2) and PDAm functionalized NP (3). In (B) only sample 3 containing PDAm shows a peak originating from electrons in a 1s orbital of nitrogen. This is related to the dopamine anchor groups of the PDAm. (C) Particle core-shell system resulting from the reduction of PDAm functionalization.

3. Crossover functionalization of iron oxide nanoparticles with DHCA and TMAH

This work was done in cooperation with [redacted] whose bachelor thesis (September 2016)[86] represents parts of this research. Her observations on the ligand exchange process supplement the findings of previous research conducted for this thesis.

Introduction

There is a great interest in preparing biocompatible iron oxide nanoparticles[87,88] for MRI diagnostic scans[89] or as drug delivery system[90]. Catechol is common in nature and has a high affinity towards trivalent iron cations and other multivalent ions, in solution or as part of a metal oxide surface of a particle. It is commonly used as a ligand to modify particle systems to meet requirements like water solubility and the formation of stable dispersions.[78] In this work, DHCA (3,4-dihydroxydihydrocinamic acid) serves as a simple catechol ligand with a carboxyl-group that forms the outer layer, defining the solubility of the particles. Deprotonation of the carboxyl-group by a base should significantly increase the colloidal stability in polar solvents like water.[91] Different alkali hydroxide bases as well as ammonium bases were tested. TMAH (tetramethylammonium hydroxide) solution showed the most promising results. Stable, dark brown dispersions could be achieved. At first, this gave reason to believe that TMAH is a potent base that deprotonates bound DHCA. TMAH is widely used as a base in hydrothermal reactions.[92–95] Unexpectedly, TMAH could disperse dried OA capped, lipophilic particles in water and form long-time stable solutions. TMAH acts like $NOBF_4$ and effectively dislodges preexisting OA from the particle surface.[38,96] This raised the question if TMAH substitutes DHCA rather than deprotonating it. Here, the effect of different concentrations of TMAH and DHCA on hydrophobic OA capped particles is analyzed.

Preparation

OA capped particles have been prepared according to the route described by Sun *et al.*[52,97] (chapter “General effects on the synthesis”). They were functionalized in THF and water with a large excess (70 molar compared to OA ligand) of DHCA and TMAH, respectively. The particles were dried before each new functionalization step. In some cases, not all particles could be dispersed again for the second step. To reappraise the results, the first step was repeated without drying.

In a second experiment, NPs were functionalized twice with DHCA. These particles were dispersed in water and increasing amounts of TMAH solution were added to test the effect of low concentrations of TMAH. The particles were precipitated with THF, washed with water and dried. For the next step equal masses were dispersed in water to react with increasing amounts of TMAH. TGA showed the mass of DHCA to be around 20 % of the total particle mass (**Figure 24**). To analyze the substitution process, molar equivalents of 10, 20, 50 and 100 % TMAH were added to DHCA functionalized particles. FT-IR was used to survey the surfactants on the particle surface. After ligand exchange TGA data were collected to support IR analysis and TEM was used to analyze shape, size and size distribution of the particle samples during the exchange processes. XRD determined the iron oxide phase of the powder.

Results and Discussion

Exchange with ligand excess

TEM images (**Figure 21**) show spherical particles arranged with equally small interparticle distances. The size distribution ranges from 5 nm to 14 nm and the arithmetical average diameter of the spherical particles is 8 nm. The distribution of particle diameter was fitted to a lognormal function with a maximum at 9 nm. XRD in **Figure 22** shows that the reflection positions can be fitted to γ-Fe_2O_3 or Fe_3O_4 iron oxide phase.[98,99] The two iron oxide phases are hard to distinguish by X-ray diffractometry. The small size of the particles broadens the reflections so no exact conclusion about the phase can be drawn. The exact iron oxide phase is not important for the experiments and thus no refinement and no Mössbauer measurements were done on this particle batch. There is one broad reflection at 21° (2θ) that does not belong to any of the iron oxide phases and is an artifact of the (not single-crystal) silicon sample holder. The position fits the (220) plane of Si.

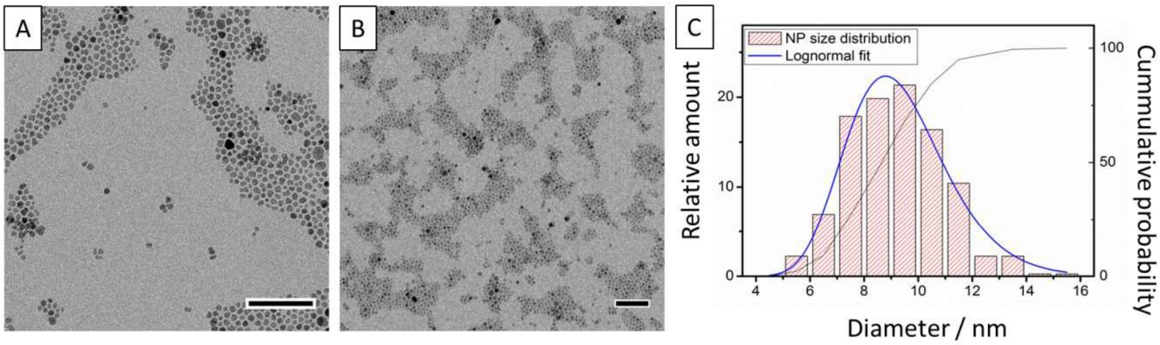

Figure 21: TEM and size distribution of the NP sample. The scale bar is 100 nm in both figures.

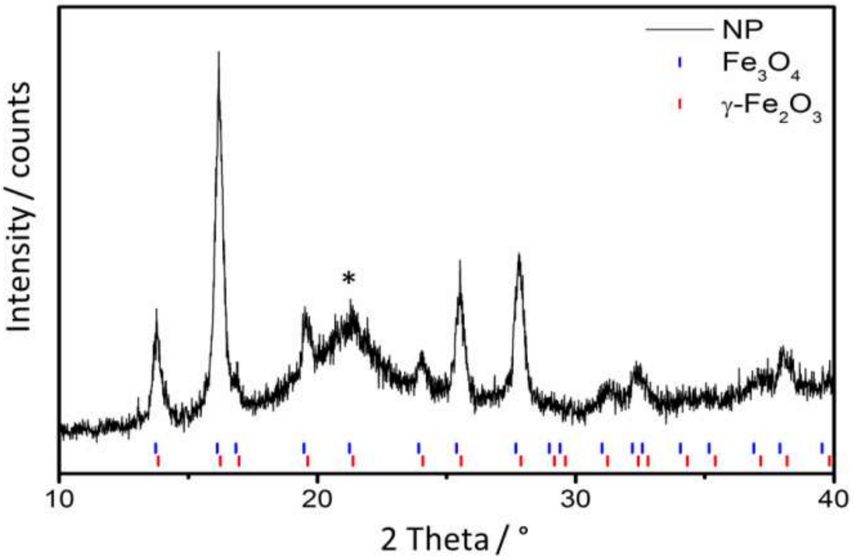

Figure 22: XRD of OA capped NP. The "*" marks a strong, broad reflection of silicon (220). The dashes mark the positions of common iron oxide phases as a reference.

Figure 23 shows the IR spectra of two alternating functionalization results after the last step. OA capped particles are shown as a reference. The name of the sample signifies the order of the functionalization steps. TMAH-DHCA means that the particles were first dispersed in TMAH solution and then functionalized with DHCA later on. OA functionalized particles exhibit several bands at around 2800 cm^{-1}, which originate from CH_2 groups as well as weak bands around 1700 cm^{-1}. They can be assigned to C=O vibrations. To characterize the predominant ligand on the surface, one unique IR-band for every used ligand (OA, TMAH, DHCA) was determined. For OA the absorption band at 1428 cm^{-1}, for DHCA the band 1260 cm^{-1} and for TMAH the band at 950 cm^{-1} was chosen. The chosen characteristic band of OA originates from asymmetric and symmetric stretching modes of the carboxylate group that is strongly overlapping with the symmetric stretching vibrations of methylene groups. [100] The characteristic bands of DHCA and TMAH are phenolic bands[101] and asymmetric C-N vibrations[102] respectively.

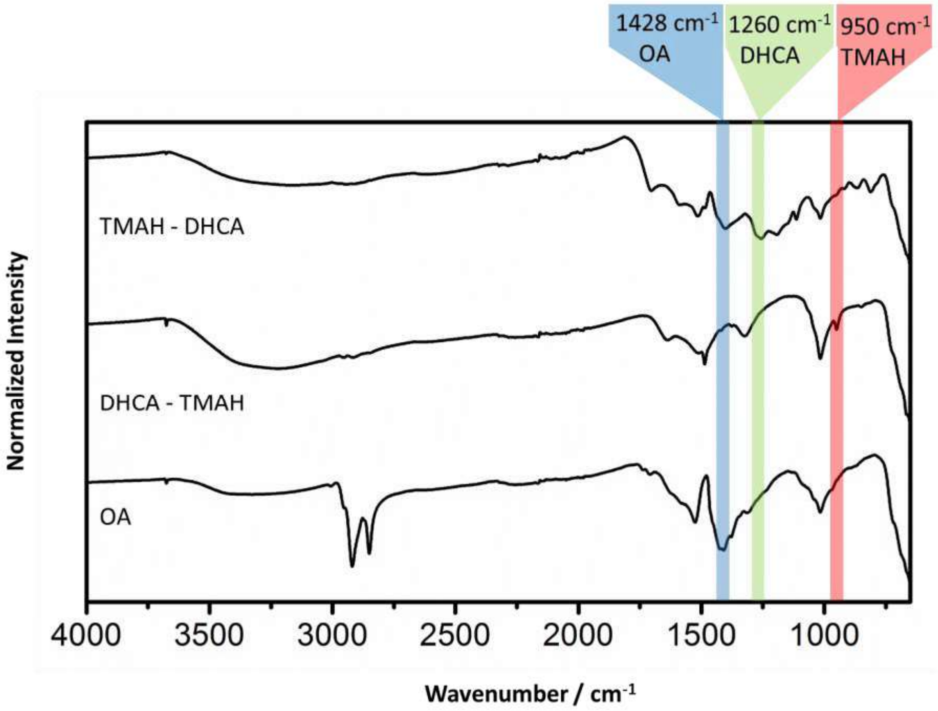

Figure 23: IR spectra of functionalized iron oxide particles. Characteristic bands of OA, DHCA and TMAH are colored blue, green, and red, respectively.

The IR data in **Figure 23** lead to the conclusion that only the latter molecule is dominantly present on the surface. OA is not visible in any functionalization case, i.e. it has been substituted. In case of a functionalization with TMAH in water, the formation of bubbles implied the presence of unbound OA as an ionic tenside. Even though DHCA is strongly connected to the particles with bidentate catechol coordination, an excess of TMAH appears to remove it completely.

TGA data of pure OA capped NP (circles), DHCA and TMAH functionalized NP (triangles and squares respectively) are plotted in **Figure 24**. The color stands for the functionalization step of the respective ligand. Orange represents the first and blue the second step. All graphs are scaled from 100 % to 60 % to compare the mass difference. To visualize the temperature of the maximum weight loss the first derivative of the function m(T) was calculated. Before the derivate, the graphs were smoothed using a sliding average method with 196 points. This eliminates the noise of the measurement which causes strong signals in the derivative. OA functionalized NPs show two major steps in weight loss at 261 °C and 378 °C as indicated by minima in the dm/dT graph (black line) and a total weight loss of 24 at 700 °C (76 % relative mass). The first weight loss corresponds with solvent remnants (H_2O, THF) adsorbed to the particles. The second, more intense loss is assigned to the evaporating and decomposition of the ligands on the NPs in the N_2 atmosphere. This means that 24 % of the total mass is oleic acid. This is in the expected range of ligand mass that varies depending on the synthesis.[77,80,100] TMAH functionalized particles lose less mass during the TGA protocol. At 700 °C the relative surfactant mass is 12 % and 9 % for first and second step which is less than the loss of the hydrophobic OA particles. TMAH NP only lose 53 % and 64 % relative to the OA capped NP.

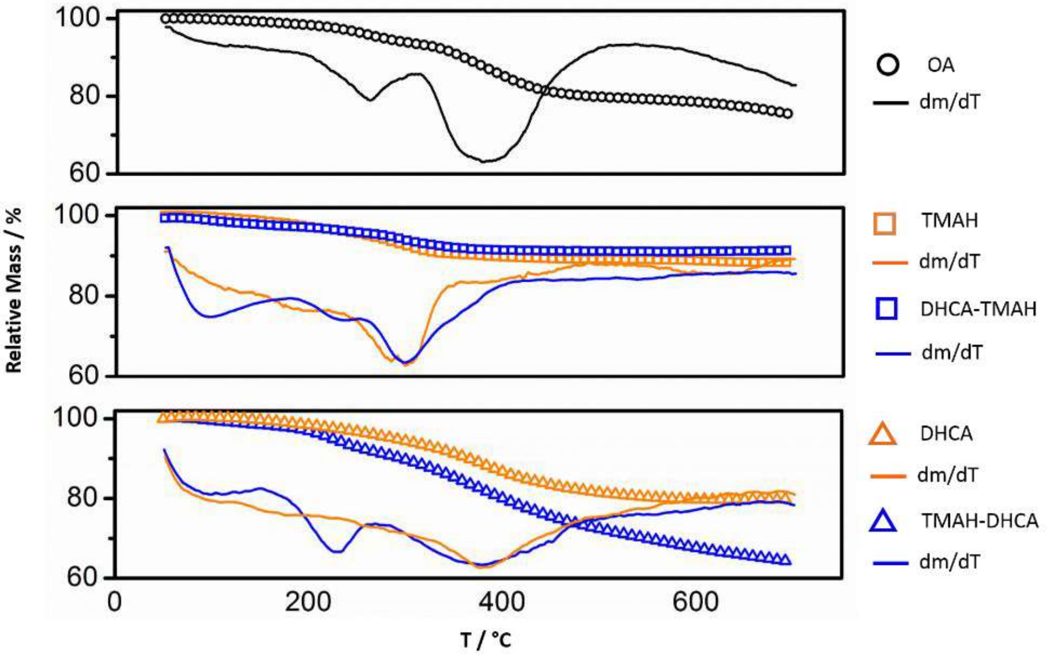

Figure 24: TGA data of OA (circles), TMAH (squares) and DHCA (triangles) functionalized particles. The colors indicate the functionalization step (orange: first step, blue: second). The line is the derivative of the relative mass.

Table 1: Data from TGA measurements.

Sample	dm/dT minima / °C				m_{rel} at 700°C / %	m_{Ligand} / %
OA			261	378	76	24
TMAH		193	297		88	12
DHCA-TMAH	96	233	297		91	9
DHCA	108			378	80	20
TMAH-DHCA	97	230		379	64	36

After the first step, NPs with TMAH show the temperature of maximum mass change at approximately 297 °C. This is also observed for particles with DHCA that were treated with TMAH in advance. They also exhibit smaller mass losses at around 100 °C and 233 °C, which are also visible in the TMAH-DHCA NPs in similar temperature regions. The first mass loss can be attributed to physically adsorbed water.[79] DHCA samples have their largest weight loss at around 378 °C, corresponding to the decomposition of the ligand. That transition temperature is higher than for TMAH samples, which means that TMAH decomposes earlier. The relative weight loss after heating differs for pretreated particles. DHCA as a second step after TMAH (TMAH-DHCA) treatment summed up to a greater organic layer on the surface than for the DHCA sample. The difference between the first and second step is 16 % relative mass (M_{rel} / %). This is 11 % relative mass more compared to OA functionalized particles. All significant temperatures of great mass loss and the corresponding relative masses are listed in **Table 1** as well as the mass loss after heating to 700 °C. This method was used because of the continuous decrease of the TGA curves did not show a plateau of constant mass after a certain heat treatment. They continued to lose weight until the end of the measurement. This was observed for DHCA-functionalized samples in different experiments (not specified in this work). Such continuous curves may occur when too much sample was used or the heating rate (°C/min) is too high. In this case, the heat does not burn all ligands in time and the organic compound will continue to scorch over broad temperature ranges even until the end of the measurement. Thus, at the end of the procedure there is still unburnt sample left. However, only very small amounts of sample (~ 5 mg) were used for every measurement. So in case of the DHCA functionalized particles another effect seems to be important. The strong binding of catechol to the particle surface may broaden the temperature region of decomposition. This is observed for different *ortho*-hydroxyphenyl-ligands like dopamine[103] and catechol.

Figure 25 shows the ligand masses determined at 700 °C. TMAH samples only show slight difference while DHCA functionalized particles possess even more organic substance than OA particles. It is assumed that upon treatment with TMAH, OA is substituted. Since TMAH has lower molecular weight than OA the observed mass loss is lower. If the particles are functionalized with DHCA in the first step, some of the OA is replaced. Since DHCA also has a smaller molecular mass than OA, the ligand mass is also smaller than for OA. It also shows that a previous treatment with TMAH cleans the surface, and more DHCA can coordinate. A similar effect could be observed for the functionalization with TMAH after DHCA treatment.

In general, a treatment of a highly affine ligand, like TMAH and DHCA, NP surface for a higher loading of the respective ligand was made in a second step. These results support the IR data of the respective exchange of TMAH and DHCA although pretreated particles differ in low temperature transitions.

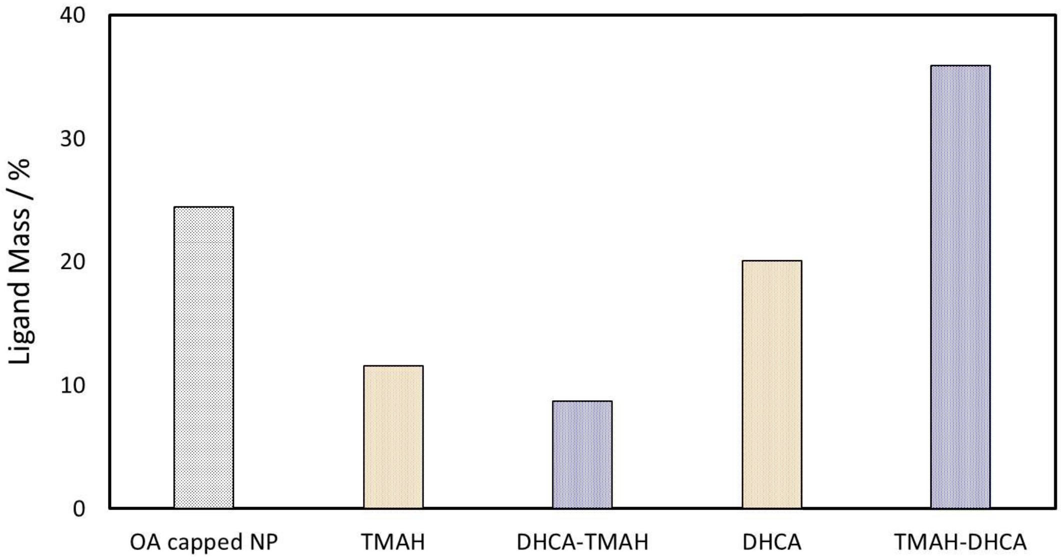

Figure 25: Comparison of the mass loss of different samples at 700 °C compared. The order of the functionalization steps is represented by order of the ligands.

In the first experiment, the ligands were added in large excess compared to the total particle mass and the mass of the particle surfactant. This raised the question at which TMAH/DHCA ratio a substitution of DHCA against TMAH can be observed in absorbance spectra. This is described in the following section.

Exchange with increasing amounts of TMAH

In this experiment, the amount of added TMAH (10 %, 20 %, 50 % and 100 % compared to OA ligand) to DHCA functionalized particles was probed. Independent of the TMAH volume, all samples formed a stable suspension of different particle concentrations with some precipitates remaining,. The particle concentration suspended in the solvent increased with the TMAH concentration, which was apparent by the color of the liquid phase. **Figure 26** shows the IR spectra of the precipitates and solutions. The DHCA band at 1260 cm^{-1} (green) appears in every spectrum, while the TMAH band at 950 cm^{-1} (red) appears in the precipitate at concentrations of 50 % (compared to DHCA surfactant) or higher. In the dispersion, the TMAH band appears already at 20 % and becomes more intense with increasing TMAH content. TMAH can either deprotonate carboxylate of DHCA ligand or replace the ligand in total (as seen in the previous experiment). For total replacement a large molar excess of TMAH is needed. In this experiment the function of TMAH as a base will probably dominate. Deprotonated DHCA stabilizes the aqueous suspension and prevents agglomeration due to repulsive Coulomb interactions. The IR spectra show characteristic bands of both molecules. At low TMAH concentrations DHCA is deprotonated and the nanoparticles remain undissolved (no colloidal suspension for 10 % TMAH content). With increasing TMAH concentration more particles are stabilized and also more particles are deprotonated but still insoluble. No quantitative statement can be made because an internal standard would be required, and a standard would change the reaction environment. A background correction was not possible in the fingerprint region. Therefore the result of this experiment is only qualitative.

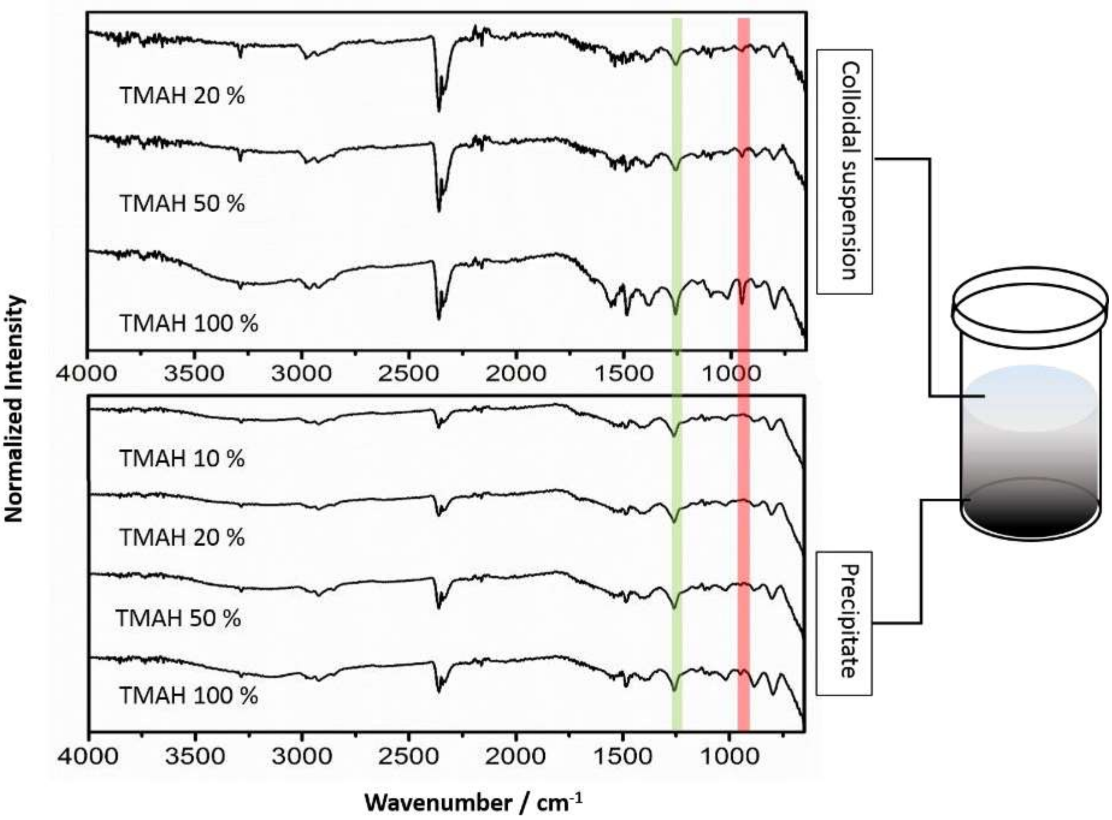

Figure 26: IR spectra of colloidal suspension and remaining precipitate of DHCA capped NP treated with different TMAH concentrations.

In conclusion, this experiment provides insights for catechol-nanoparticle stability. Even though the coordination of ligands onto (particle) surfaces is an equilibrium reaction, surfactants cannot be “washed off” completely with solvents. The TMAH ligand allows for complete ligand exchange. For small concentrations up to a 1:1 ratio (DHCA/ TMAH) DHCA is still detectable from its characteristic band at 1260 cm^{-1} in precipitate and in solution. This indicates that TMAH deprotonates DHCA and enhances the colloidal stability in water. For higher TMAH concentrations the DHCA band vanishes in the IR spectra. DHCA is replaced with TMAH completely. The ligand exchange is reversible: TMAH can be replaced with DHCA.

IV. SPINDLE-SHAPED PARTICLES

4. Spindle shaped Nanoparticles – Size and Shape

Introduction

Anisotropic particles have been the focus of many studies[18,104] because they are promising materials for many applications ranging from cathode materials[105,106] to applications in heterogeneous catalysis.[107] In this work, anisotropic iron oxide particles were used for different projects. This chapter describes the synthesis and the reaction parameters affecting the particle size.

Spindle-shaped hematite particles were first synthesized by Ozaki *et al.* through forced hydrolysis of iron chloride in water at boiling temperature.[108] Over the years this synthesis was used to prepare particles for several applications, including plasmonic structures[109] and materials that respond to magnetic fields.[21,110] Transmission electron microscopic analysis by Frandsen *et al.* unraveled the formation mechanism of “nano-rice”.[111] They determined the precursor state to be akaganeite (FeO(OH)(Cl)), rod-shaped particles that agglomerate along the long axis and react to iron (III) oxide (hematite). Concentration of ferric chloride salt ($FeCl_3$) and hydrochloric acid (HCl) affect shape and composititon.[112–114] Phosphate (often monobasic potassium or sodium phosphate) is added in catalytic concentrations to control the morphology. In the absence of phosphate the morphology of the particles is not spindle-shaped.[111,115]

This synthetic method was used to acquire large amounts of shape anisotropic particles using cheap, abundant chemicals. In this project, the dependence of the particle size on experimental parameters like reaction volume, precursor concentration, reaction time and stirring speed was analyzed.

Preparation of the Particles

The particles were prepared by dissolving iron chloride (anhydrous or hexahydrate) together with catalytic amounts of monobasic potassium phosphate (KH_2PO_4) in deionized water. The concentration of iron chloride and potassium phosphate as well as the volume of the solution was varied in several experiments (see experimental part). The resulting clear, yellow solution was then heated using an oil bath or a heat mantle. The solution remained under reflux conditions for three days. Stirring was performed either with a magnetic stirrer for solution volumes up to one liter or a mechanical stirrer for 2 L experiments. For most experiments, the stirring speed was approximately 300 RPM. The particles were precipitated by adding THF or NaOH solution, dried and then used for further experiments. For larger quantities, the reaction was scaled up proportionally.

Results and Discussion

Influence of reaction volume

The experiment was first carried out in a 100 mL flask. To obtain larger quantities, the reaction was scaled up to 250 mL, 500 mL, 1000 mL and 2000 mL with the corresponding amounts of starting chemicals. This revealed that with higher amounts of reactant, but equal concentrations, the particles became larger in size. **Figure 27** shows the average particle length plotted against the reaction volume. The average length increases with a reaction volume from 100 mL up to 1000 mL while for 2000 mL the average particle length was smaller than for 1000 mL. All average sizes and size distribution are listed in **Table 2**. The plot reveals that the dimension of the long axis approaches a limit (~450 nm) with increasing volume. The reaction in 2000 mL is marked because a different experimental set-up (different mechanical stirrer and heat mantle) was used. There were no experiments done to determine the number of particles per reaction. The yield of the reaction after three days was determined by the mass of the dried powder. It was approx. 95 % for all experiments, i.e. larger reaction volumes lead to fewer particles. In the upscaling process, the concentration of the reactants remained identical. Thus, the particle sizes are influenced by the mixing and heat transfer. All experiments in one-neck flasks had similar filling levels. The heat was transferred from the oil bath or heat mantle through the glass wall of the flask. With increasing size of the reaction vessel, the inner surface only increases with R^2 while the volume is a function of R^3 (with R being the radius of the flask). Thus, small flasks have a larger surface to volume ratio and a higher surface for reaction. This may lead to enhanced nucleation. Because the heat source and the stirrer were changed for the large 2 L experiment, the particle size for the large scale synthesis does not follow the previously observed trend.

Table 2: The average lengths of nanoparticles depend on the reaction volumes.

Flask volume / mL	Average length / nm	Standard deviation / nm
2000	416	32
1000	455	104
500	363	85
250	287	56
100	256	82

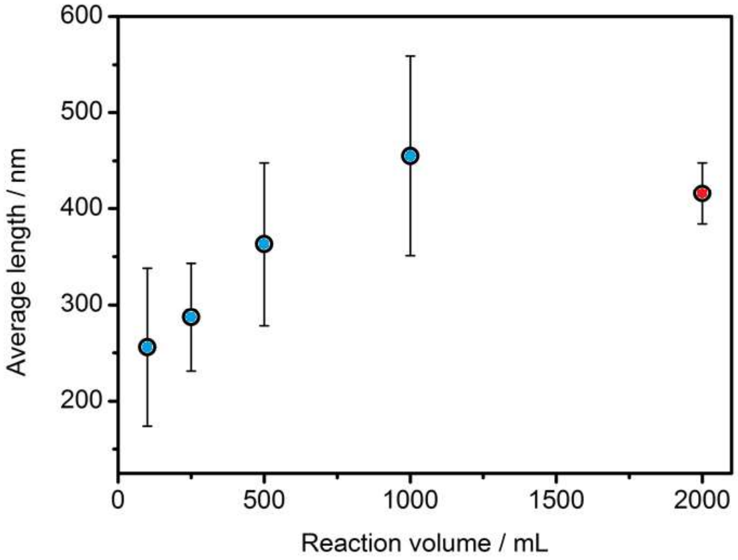

Figure 27: Average size depending on the flask volume.

Influence of precursor concentration

Figure 28 shows TEM images of experiments with half and double concentration of both ferric chloride ($FeCl_3$) and potassium dihydrogen phosphate (KH_2PO_4), respectively. The morphology remained spindle-shaped for c = ½, but the surface was rougher than that of particles from higher concentrated solutions (A). When the concentration was doubled (c = 2), the particles are rod-like and smaller (C). The small particles were akaganeite (FeOOH(Cl)), as demonstrated by powder diffraction (B). Independent of the reaction volume, at double concentration the product was a clear brown solution of akaganeite particles. Large particles show a broad particle length distribution.[3] This distribution can be described by a superposition of several normal (Gaussian) distribution functions. In this case, a symmetric distribution function can be applied because the size of the particles is large enough and no argument of the fit function takes negative values. The maxima of the distribution of length are all approximately 45 nm apart, which is exactly the long axis of the smaller akaganeite particles resulting from experiments of double concentration (see **Table 2**). This is in agreement with the results of Frandsen *et al*. The formation mechanism is displayed in **Figure 30**. Note that the small akaganeite particle distribution of the long axis can be fitted using a lognormal function.[4] Since the particle size is relatively small, this method makes sense as it takes into account that particle size cannot go below zero nanometers.

Table 3: Average length and width of particles prepared with different precursor concentrations.

Particle / Concentration	Average length / nm (relative error / %)	Average width / nm (relative error / %)	Ratio long / short axis
Fe_2O_3 / c = 1 (“regular”)	287 (56)	73 (13)	3.9/1
Fe_2O_3 / c = 1/2	171 (24)	39 (15)	4.3/1
Fe_2O_3 / c = 2	44 (27)	13 (19)	3.4/1

---

[3] Shape of the distribution function depends on the number of classes chosen. The number of classes was set by Origin 8™ automatically. This is according to the equation:
(max-min)/(1 + *value* * log10(npts)
http://www.originlab.de/doc/Origin-Help/Create-Histogram#Controlling_the_binning

[4] Lognormal fit function in Origin 8™ (13) and gaussian fit (14)

$$\boldsymbol{y = y_0 + \frac{A}{\sqrt{2\cdot\pi}\cdot w\cdot x}\cdot e^{\left(-\frac{\left(\ln\frac{x}{xc}\right)^2}{2\cdot w^2}\right)}} \tag{13}$$

$$y = y_0 + \frac{A}{w\sqrt{\pi/2}}e^{-2\frac{(x-x_c)^2}{w^2}} \tag{14}$$

Fitfunctions for lognormal (13) and Gaussian fit (14).

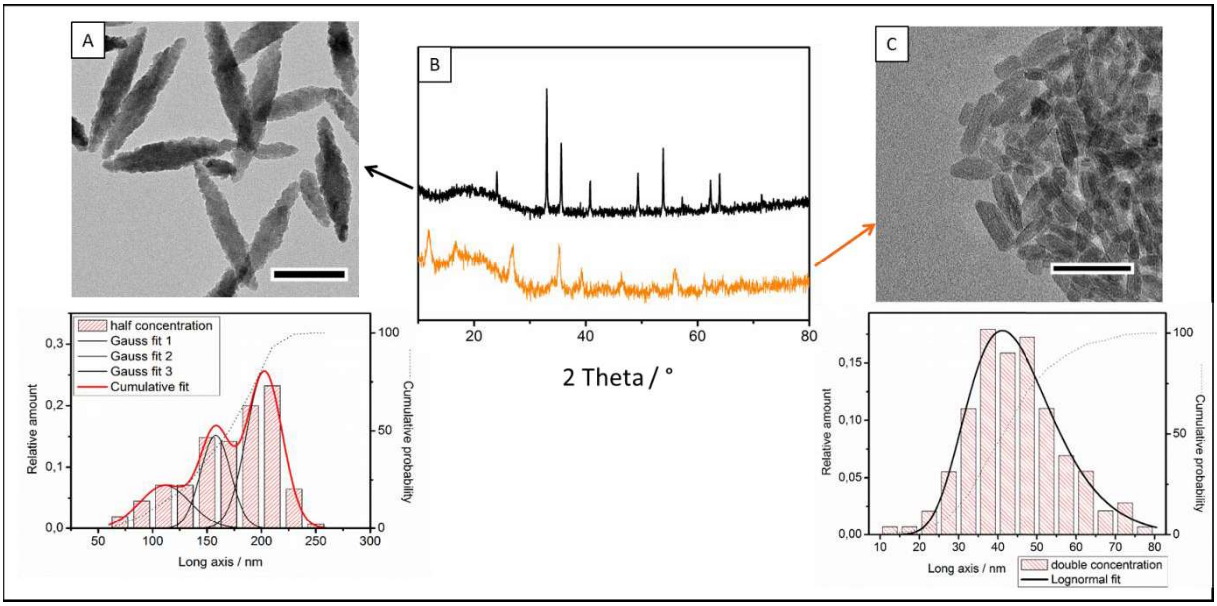

Figure 28: A) Hematite spindle-shaped particles show broad size distribution (long axis) with multiple maxima (scalebar 100 nm). C) Akaganeite particles are smaller in size and have a narrow distribution that can be fitted by a lognormal function (scalebar 50 nm). B) Shows powder XRD patterns of both materials.

Influence of reaction time

The growth mechanism was analyzed by taking serval small aliquots from the reaction solution after 4, 22, and 44 hours, as shown in **Figure 29** C-D. The snapshots show the formation of akaganeite particles at the early stages of the reaction after only 4 hours. Agglomeration of these particles then led to the formation of long rods and small spindle-shaped structures, several micrometers in length. Besides these agglomerates there were spindle-shaped structures with similar size but without sharp edges. In addition precursor akaganeite particles remained. After 44 h, small spherical particles next to the spindle shaped hematite particles could be observed. These spherical particles do not resemble the akaganeite particles from the early stages but rather appear to be parts of larger particles. After three days of reflux there are no small particles left. The color of the dispersion changed from transparent yellow of the $FeCl_3$ aqua complex to a black turbid solution and finally to a dark brown. Size distributions are shown in (A) along with the resulting sum of Gaussian functions used to fit the distribution (inlay). With increasing reaction time, the distribution becomes broader and exhibits multiple maxima. This is similar to the behavior described above. The distances between the maxima correspond to the size of the small precursor units (blue). Picture (B) depicts the size over a certain period of time.

In summary, a reaction time of three days is necessary to obtain phase-pure spindle-shaped particles. During the reaction many different particle morphologies occur. Eventually, hematite was formed.

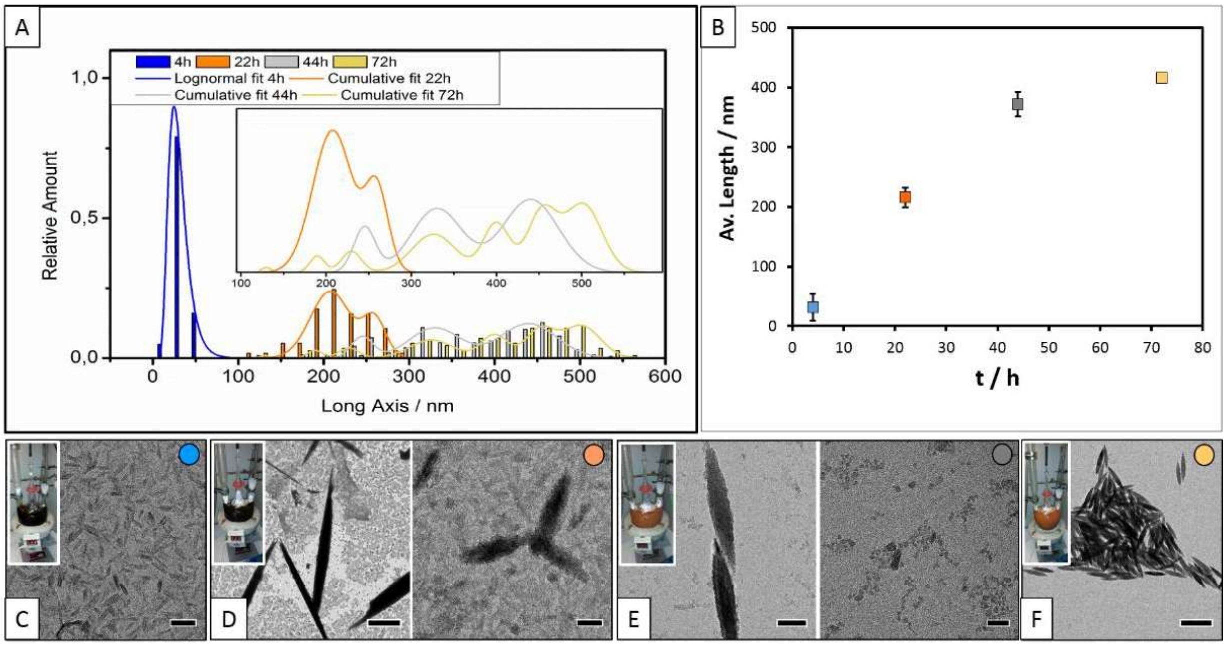

Figure 29: A) Size distribution of aliquots after 4 h (blue), 22 h (orange), 44 h (grey) and 72 h (yellow). B) Plots the average length against reaction time. C) – F) show TEM images of aliquot samples at respective times.

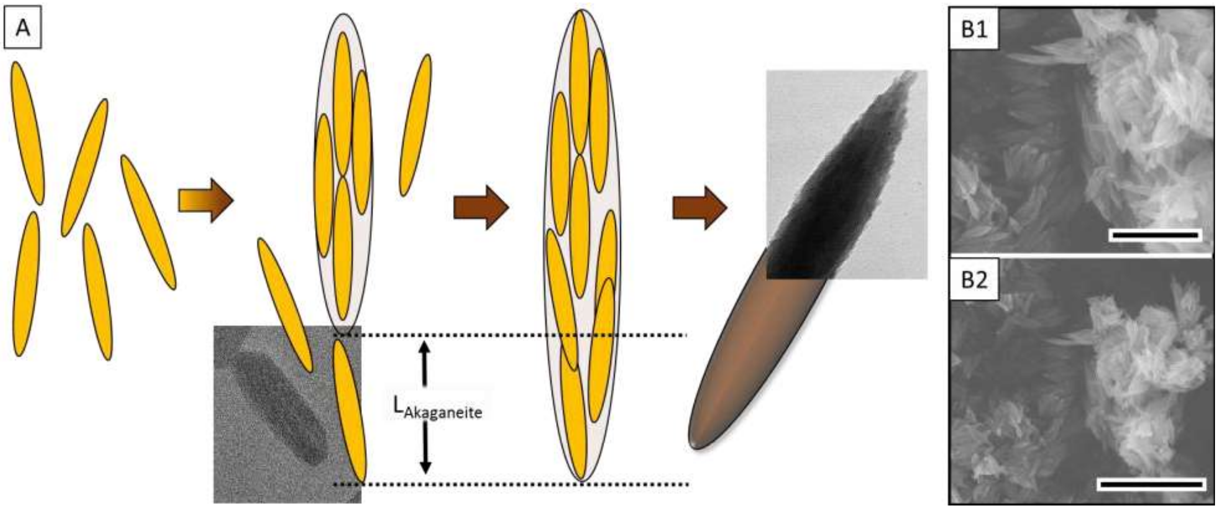

Figure 30: A) Formation of hematite particles by oriented attachment of akganeite particles followed. B) Shows SEM images of resulting hematite particles. The scalebars are 1 µm and 2 µm in B1 and B2 respectively. SEM pictures were taken by Hannah Huesmann.

Influence of stirring speed

Figure 31 shows the influence of different stirring speeds on the particle formation. The average size is plotted against the reaction time. The fit-curves are not shown for reasons of clarity. Two experiments with rather different stirring speed were kept under reflux for 7 days. Stirring has no influence on the particle morphology as seen in the TEM images. A comparison of the average particle size after three days revealed no clear trend. No stirring led to larger particles than rotating at 300 RPM. The particle sizes for high and lower rotation speed are intermediate. Reaction times had no effect on the particle size in the flask with 100 RPM but 700 RPM led to larger particles after longer reaction times. For each aliquot size distributions were broad but show more particles at larger diameters for longer reaction times.

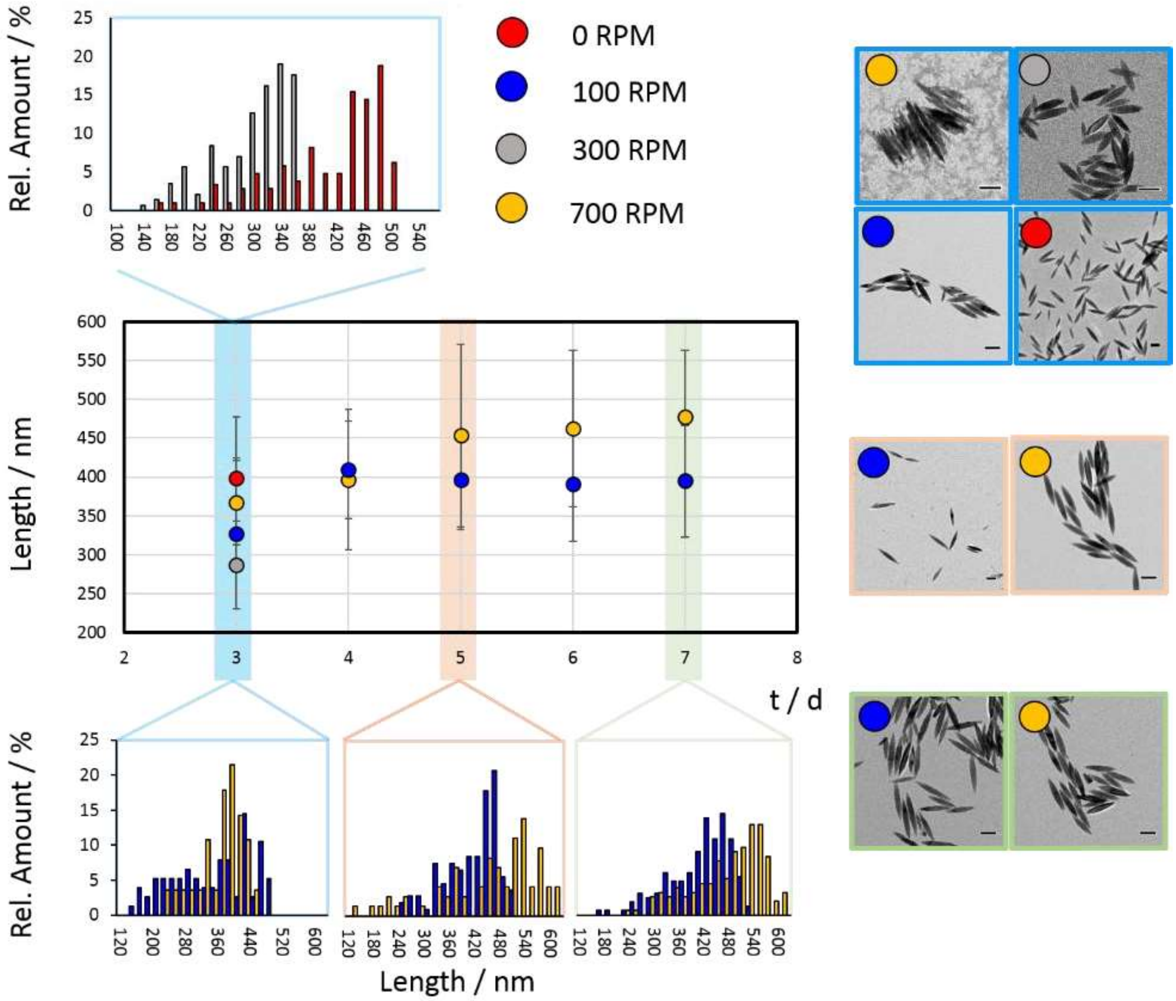

Figure 31: Influence of stirring speed on particle size (average length).

The particle size strongly depends on the concentration of the iron salt. Low concentrations lead to smaller particles, while higher concentrations inhibited the formation of hematite. The reaction stopped at the precursor iron oxide hydroxide which formed small rod-shaped particles. The size of the akaganeite particles was almost independent of the reaction volume (see **Figure 32**). The oriented attachment of the iron oxide hydroxide to form hematite is strongly influenced by the stirring speed and the reaction volume. Upscaling the reaction in larger flasks or increasing the stirring speed lead to larger particles. Even though the synthesis is known for 30 years and the mechanism is clarified, the effect of these reaction parameters is often neglected.

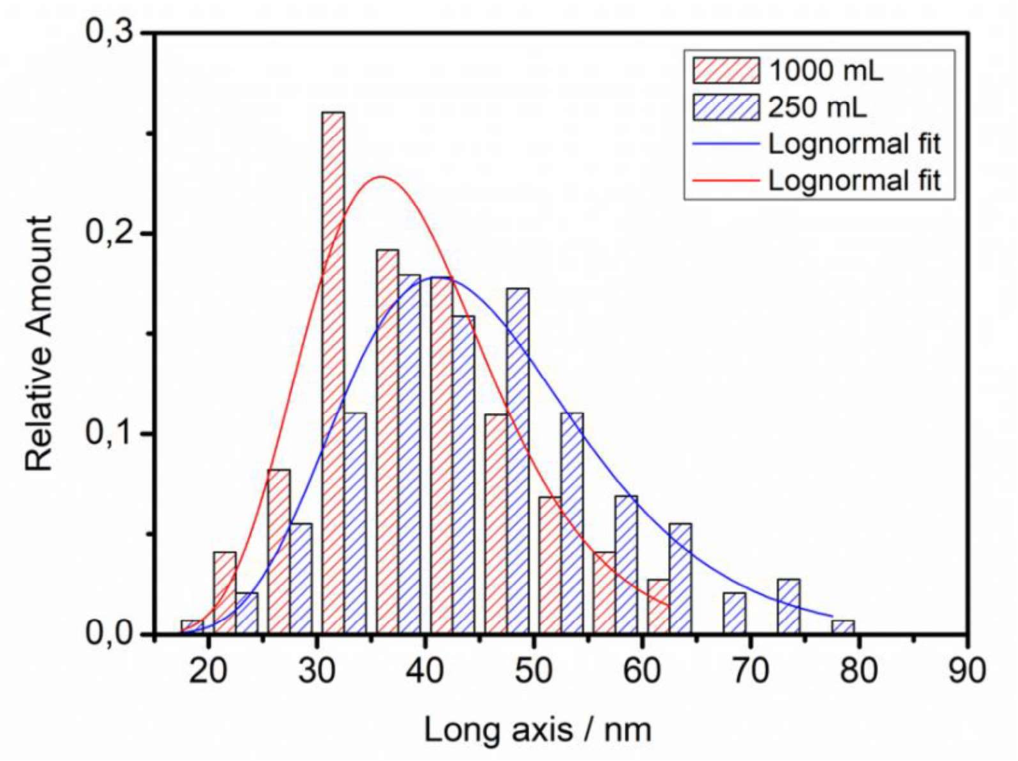

Figure 32: Comparison of akaganeite particles from 250 mL and 1000 mL reaction.

5. Reduction of Spindle-shaped particles

This chapter tackles the synthesis for spindle-shaped magnetic iron oxide particles. Hematite (α-Fe_2O_3) and akaganeite ($FeO(OH/Cl)$) particles proved to be an excellent starting material because they could be reduced in different ways while preserving the particle morphology. They form anisotropic magnetic particles which were used for the preparation of magnetically controlled liquid crystal phases as they are described in chapter 6.

Introduction

Several methods are common to reduce metal ions, complexes or particles. A reported method to generate elemental iron(0) nanoparticles via reverse micelles of CTAB (cetyltrimethylammonium bromide) is the reduction of iron (II) with hydrazine.[116] Yanagisawa *et al.* reduced hematite powder to magnetite under hydrothermal conditions in an autoclave with controlled H_2 content and pressure.[117] Formation of the reduced product is postulated to be a dissolution-reprecipitation process. This is similar to reports of the formation of magnetic metal particles through reduction of metal ions in the presence of stabilizing ligands. Neither method is a suitable approach for the shape-preserving reduction of nanoparticles.

The easiest way to reduce metal chalcogenide (nanoparticle) powder is using hydrogen.[118] Hematite reduction in hydrogen-enriched atmosphere under elevated temperatures in an oven has been investigated with different hydrogen concentrations and temperatures experimentally and theoretically.[119,120] It has been found that the water to hydrogen ratio (equation (15)) plays an important role. Zielinski *et al.* discovered that the number of steps from Fe_2O_3 to Fe(0) varies depending on the ratio of H_2O/H_2.[121] Hematite is reduced directly to iron at temperatures around 300 °C for low ratios (high H_2 concentration). At lower H_2 concentration a three-step reaction was observed. Magnetite was formed from hematite at around 400 °C and iron (0) at 470 °C. With rising temperatures, the content of Fe(0) increases. At 700°C the reduction product was only iron.

$$\mathbf{3Fe_2O_3 + H_2 \rightarrow 2Fe_3O_4 + H_2O} \qquad K_1 = \frac{c(H_2O)}{c(H_2)} \tag{15}$$

In the oven the particles were heated in a crucible for several hours under continuous hydrogen flow. To prevent agglomeration of the particles during this process the nanoparticle powder could be diluted in an inert matrix like NaCl and heat-treated at temperatures below the melting point of the matrix. This increased the interparticle distances. Another approach is the protection of the particles with a porous SiO_2-shell that prevented agglomeration of the metal oxide core but still allowed the reduction with hydrogen gas through the pores.[21]

Reactions in solution under constant stirring prevent particles from "growing together". Hai and co-workers demonstrated the reduction of maghemite (γ-Fe_2O_3) particles, prepared via an iron oleate/iron pentacarbonyl route, with carbon monoxide and carbon dioxide.[122] They used a gas detection system to analyze the amount of gas generated during the reaction of maghemite particles with OA in TOA at temperatures of 260 °C to 350 °C. The detected gas amounts were higher than the OA content would allow, indicating combustion of the solvent at elevated temperatures. The formed CO and CO_2 were able to reduce the γ-Fe_2O_3 to Fe_3O_4 up to 300 °C and even to FeO (wustite structure) at 350 °C under preservation of shape, size and size distribution.[123] In fact, a mixture of FeO and iron oxide spinel phases was observed. Bulk FeO is stable above 560 °C and disproportionate to Fe^0 and Fe_3O_4 at lower temperatures.

A hydrogen/nitrogen gas mixture can also be passed directly into the solution. Chemicals like 1,2-diols also possess reducing properties as well as the solvent itself in some cases.[60] Some studies used hydrogen and organic molecules simultaneously.[56]

In this work, the prepared spindle-shaped particles were reduced from α-Fe_2O_3 to Fe_3O_4 and Fe(0). The reaction was performed in a furnace at elevated temperatures around 400°C to 500°C with and without a salt-matrix. A continuous hydrogen gas flow provided the reactive atmosphere. The particles were filtered prior to the next experiment. A third route was the reduction in organic, high boiling solution with reducing agents. The reaction in high boiling solvents will be described in more detail. Both synthesized form-anisotropic particle types, hematite (Fe_2O_3) and akaganeite (FeO(OH/Cl)) were treated in trioctylamine (TOA), benzyl ether (DBE) and phenyl ether (DPE). Between 20 and 100 mg of particle powder were heated in a three-neck flask with condenser and thermometer up to reflux temperatures of the respective solvent. As a reducing agent 1,2-tetradecandiol was added or hydrogen/nitrogen (5:95) was passed through the solution as gas-bubbles. Under reflux condition the hydrophilic particles were fully dispersed in the solvents and the color changed from clear with brownish particles to turbid black indicating the successful reduction to magnetite. The particles were washed with cyclohexane and ethanol. In some experiments, OA and OAm were added in order to improve the colloidal stability of the magnetic particles in nonpolar solutions, as it is known for the formation of spherical particles (see chapter 1).

Results and discussion

Reduction under H_2/N_2 atmosphere. All reactions were performed in a crucible under hydrogen atmosphere (5/95 H_2/N_2). This resulted in black magnetic powder at temperatures exceeding 400 °C regardless of the presence of an inert matrix. The product was not completely dispersible in water due to particles fusing together under high temperatures. For anisotropic, spindle-shaped particles of around 500 nm, calcination leads to the formation of particle clusters with random alignment of the long axis as shown in **Figure 33**. Particles, diluted in an inert NaCl-matrix, showed fewer agglomerates. Insoluble agglomerates, caused by the direct contact between particles during this process, are the disadvantage of this method. The thermal energy required for the reduction also facilitates the diffusion of atoms at the contact area, resulting in insoluble agglomerates and consequently the properties originating from the small size and high surface to volume ratio are lost. However, after filtration the dispersion was left with single dispersed particles without surfactants. Those particles were used in the manufacturing of liquid crystal phases (see chapter 6)

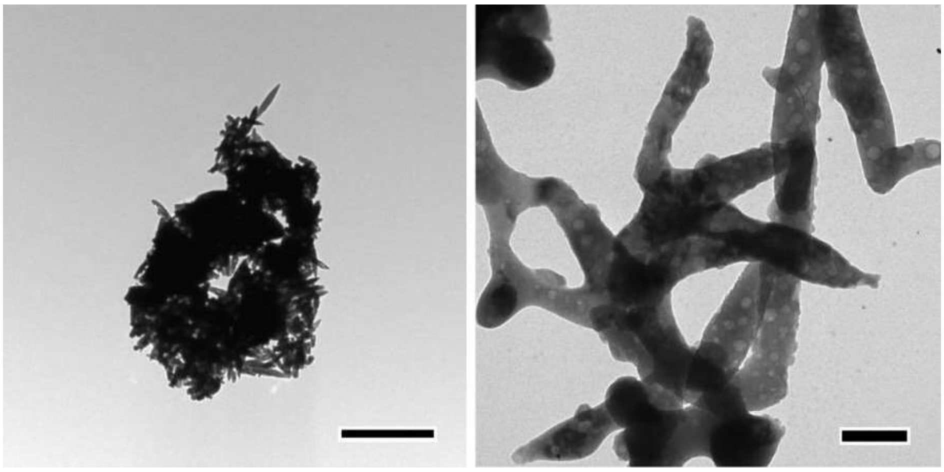

Figure 33: Particles fused together through heat treatment under hydrogen atmosphere at 400 °C. The scalebar is 1 µm (left) and 100 nm (right).

Reduction in high boiling solvents: In high boiling organic solvents like TOA and dibenzyl ether both hematite and akaganeite particles could be reduced to magnetite while preserving size and morphology as seen in TEM images in **Figure 34**. In some cases, low contrast areas are visible under the TEM, leading to the conclusion that areas of lower density formed or two phases of different contrast developed. It is estimated that the areas evolve due to Kirkendall effect[124,125] which describes the diffusion of one phase into an adjacent phase and the shift of the boundary relative to the total volume of the two phase system. An addition of OA and OAm resulted in the decomposition of the spindle-shaped particles. They tend to break into smaller particles as shown in **Figure 35**. The magnetic product contained small, spherical particles. Remnants of the spindle-shaped particles could be precipitated from organic solvents with ethanol. This observation indicates that a dissolution/crystallization process is favored when OA and OAm are present. As in the thermal decomposition route, oleic acid stabilized the formation of particles from dissolved clusters. The length distribution of the long axis illustrates the decomposition. The broad but monomodal distribution of the akaganeite particles broadened and exhibited multiple maxima after reduction. The particles now had an average diameter of 8 nm which is close to the dimensions of spherical particles made from Fe(acac)$_3$ in high boiling ethers (see size distribution in **Figure 35**).

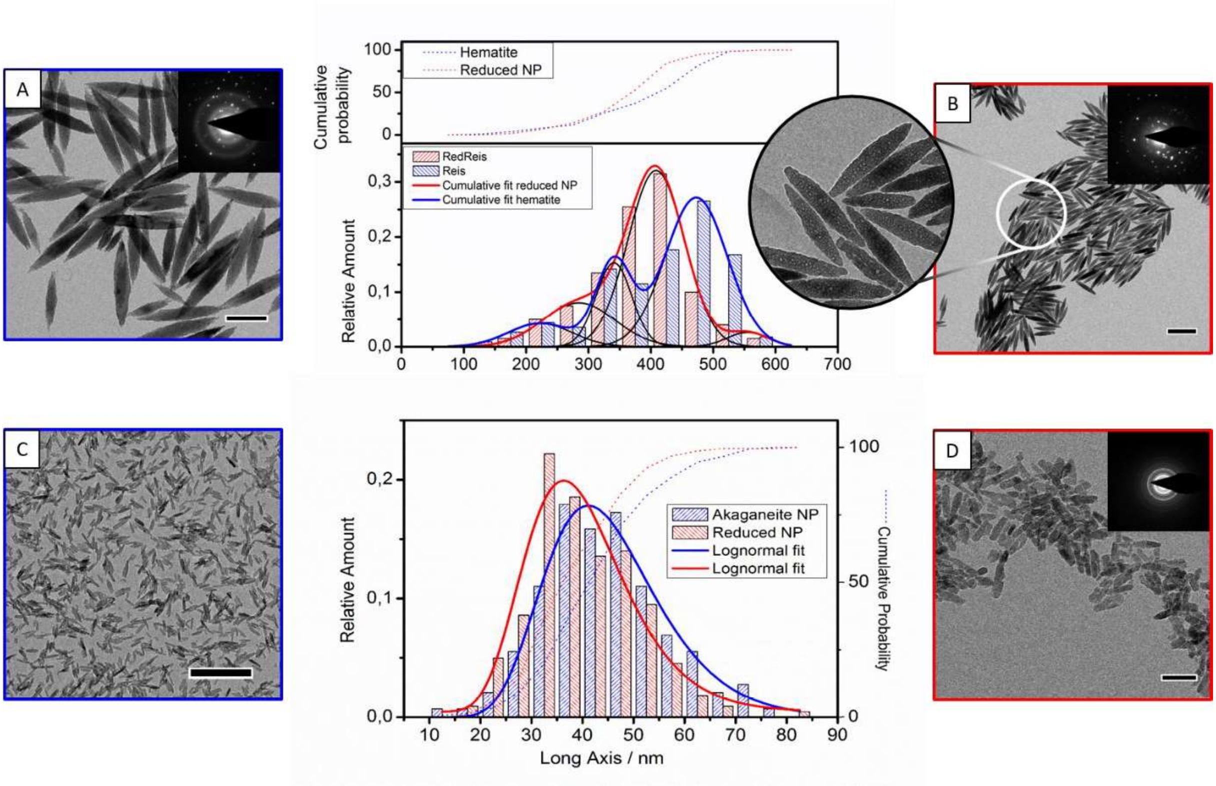

Figure 34: Hematite and akaganeite particles before and after the reduction (A and B, C and D respectively). Magnification shows the porous structure of the magnetic articles due to the Kirkendall effect. Distribution curves of long dimension of the long axis show multiple maxima for Fe$_2$O$_3$ fitted with multiple Gaussian functions and monomodal distribution fitted with lognormal function for shorter akaganeite particles. Scalebar: 500 nm (A and B), 250 nm (C), 100 nm (D).

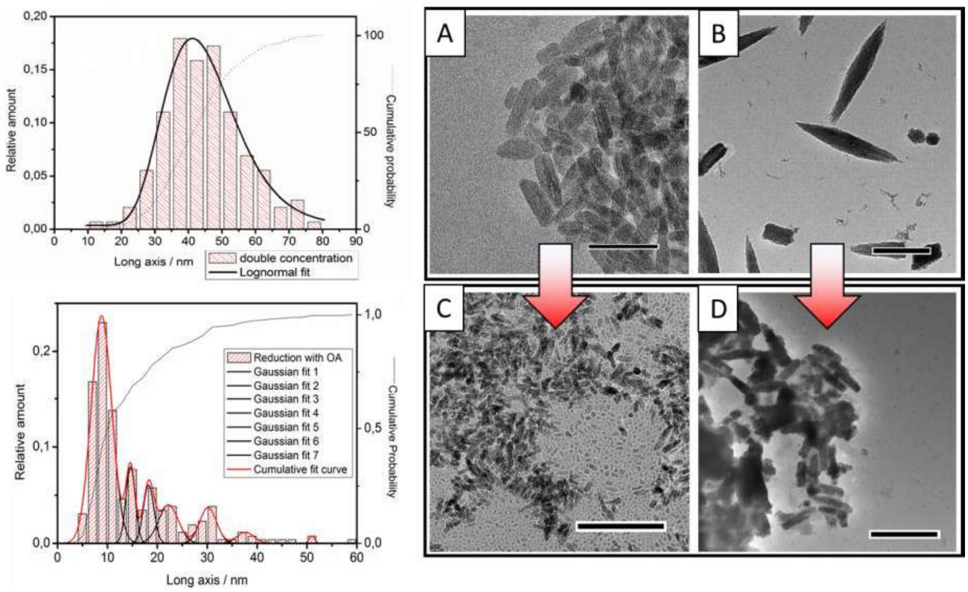

Figure 35: Change of morphology due to reduction in the presence of OA and OAm for akaganeite (A and C) and hematite (B and D). Dimensions of long axis for the akaganeite particles of (A) (before), and (C) (after). Scalebars are 50 nm (A), 250 nm (B), 200 nm(C), and 500 nm (D).

Interestingly, for hematite and akaganeite different minimum temperatures were necessary for reduction. α-Fe_2O_3 spindle-shaped particles needed higher temperatures (300 °C) and therefore could only be reduced in TOA (b.p. 320 °C), while FeOOH could be reduced already in dibenzyl ether (290 °C) with and without diol as an electron source like TDD. This may be due to the different particle sizes of the iron oxide and iron oxide hydroxide species or the different surface structure and composition. Dibenzyl ether (DBE) acted as a reducing agent generating black, magnetic powder after a few hours at boiling temperature. This is an interesting observation because other groups have shown that DBE can decompose in a radical reaction at high temperatures to form toluene and benzaldehyde.[126] This oxidative effect distinguishes DBE from other high boiling (alkane or alkene) solvents like octadecane or octadecene. In nanoparticle synthesis, this causes the formation of inverse spinel, iron oxide phases like maghemite (γ-Fe_2O_3) and magnetite (Fe_3O_4) for example.[127] In case of akaganeite particles a yet unclear reaction leads to particle reduction.

Figure 36 shows the FTIR spectra of the hematite and akaganeite particles (yellow and red) as well as the both reduced products. In case of akaganeite the characteristic band centered at 1040 cm^{-1} and the broad band centered at 850 cm^{-1} were assigned to deformation modes of the O(H)-Fe groups and the Fe-O-Fe bridges (and torsion of surface bound water), respectively.[128,29,129] They disappear as a result of the reduction. The same was observed for hematite. Both reduced samples exhibit similar bands, indicating the successful reaction and multiple bands centered at around 2920 cm^{-1}, 1550 cm^{-1}, 1390 cm^{-1} and 1000 cm^{-1} characterized by C-H vibrations and C-C vibrations of organic molecules on the particle surface after the reduction. Magnetite should feature no significant bands between 1000 cm^{-1} and 4000 cm^{-1} except for the Fe-O(H) and O-H vibrations originating from adsorbed water.[87] The hematite spectrum also shows a broad band centered at around 3350 cm^{-1} originating from water. At low energies Fe-O vibrations absorb at 465 cm^{-1} and 539 cm^{-1}.[79] The broad band is a superposition of multiple bands as it is indicated by the small waves on the curve. It can be related to iron-phosphate arising from complexation of catalytic phosphate (monobasic potassium salt) from the reaction.[130]

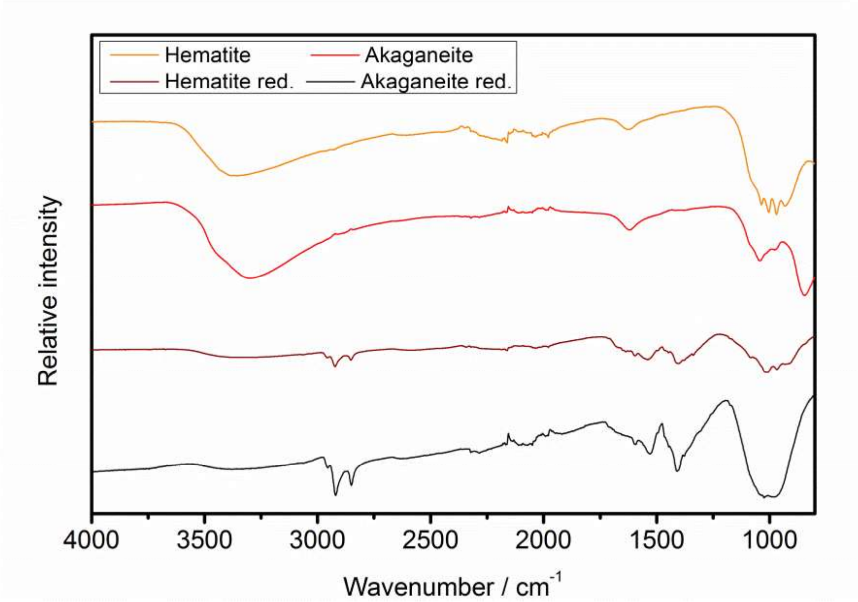

Figure 36: IR spectra of akaganeite and hematite as well as the reduced particles of both samples.

Magnetization measurements as a function of applied magnetic field-strength are shown in **Figure 37**. The prepared particles containing Fe^{3+} had low magnetization values even at high magnetic fields of 3 T. Both akaganeite and hematite particles showed weak ferromagnetic behavior and narrow hysteresis curves which has been reported for similar particle systems.[131,132] Reduced species have a magnetization of 44 emu/g and 47 emu/g for akaganeite and hematite, respectively. The bulk magnetization for magnetite (Fe_3O_4) is reported to be 94 emu/g.[127] This indicates an incomplete reduction of the particles (which was later confirmed by X-ray diffraction) or high surface defects.

X-ray diffraction patterns of the dried particle powders before and after the reduction process are shown in **Figure 38**. Since the samples were measured on different diffractometers using molybdenum ($\lambda(K_{\alpha1})\sim$ 0,73 Å) and copper ($\lambda(K_{\alpha1})\sim$ 1,53 Å) radiation, the 2 theta scales vary depending on the radiation. The small akaganeite particles - here tagged “nanorods” - show broader reflections and less intensity than the approximately 10 times larger hematite particles.

The intensity was normalized, but the akaganeite samples exhibit a smaller signal-to-noise ratio. All reflections of the particles prepared from forced hydrolysis could be assigned to reference patterns for the respective material. The reference patterns are listed in **Table 18**. After reduction in high boiling solvents the diffraction pattern showed multiple reflections that agree with those of magnetite. Reduced hematite particles still show some reflections that agree with these of hematite, indicating the incomplete reduction. The marked reflections can be assigned to carbon that had formed during the heating process.

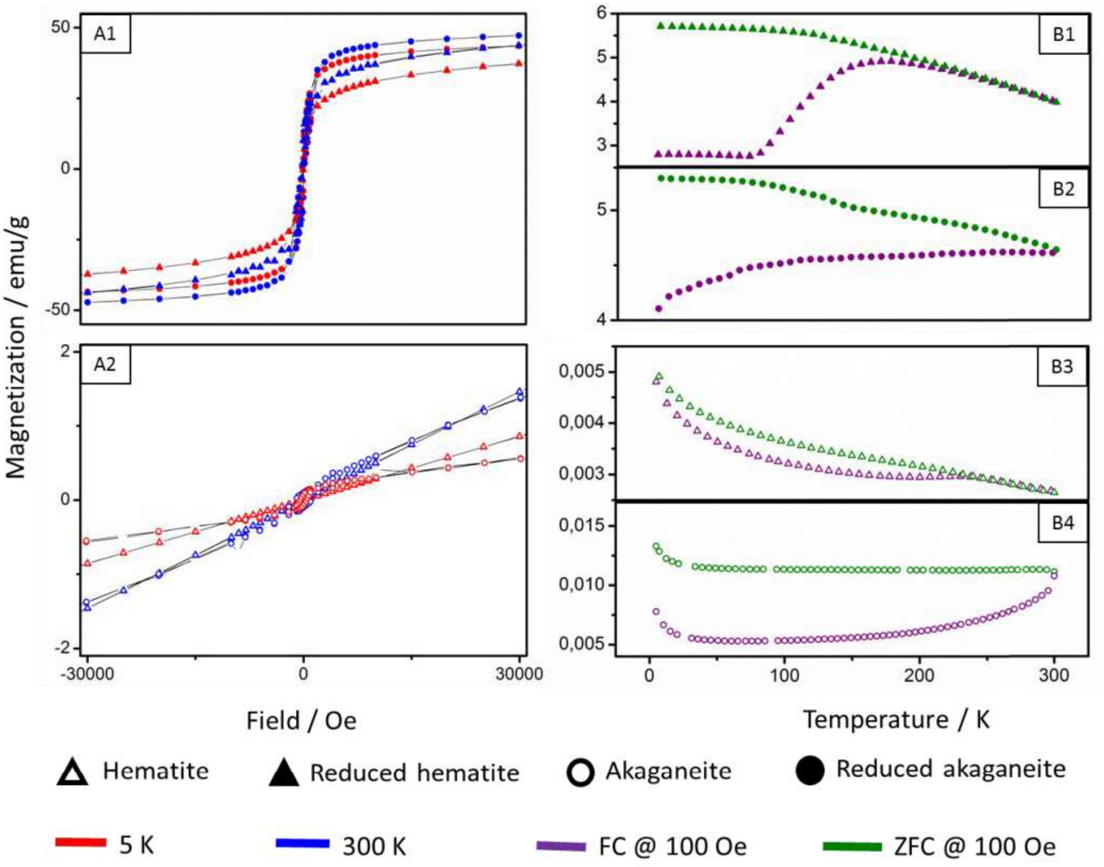

Figure 37: Magnetization measurement of as prepared particles (hollow symbols) and reduced species (full symbols). The color represents the temperature in the magnetization against field measurements (left) and the FC or ZFC curve in the magnetization against temperature measurements (right).

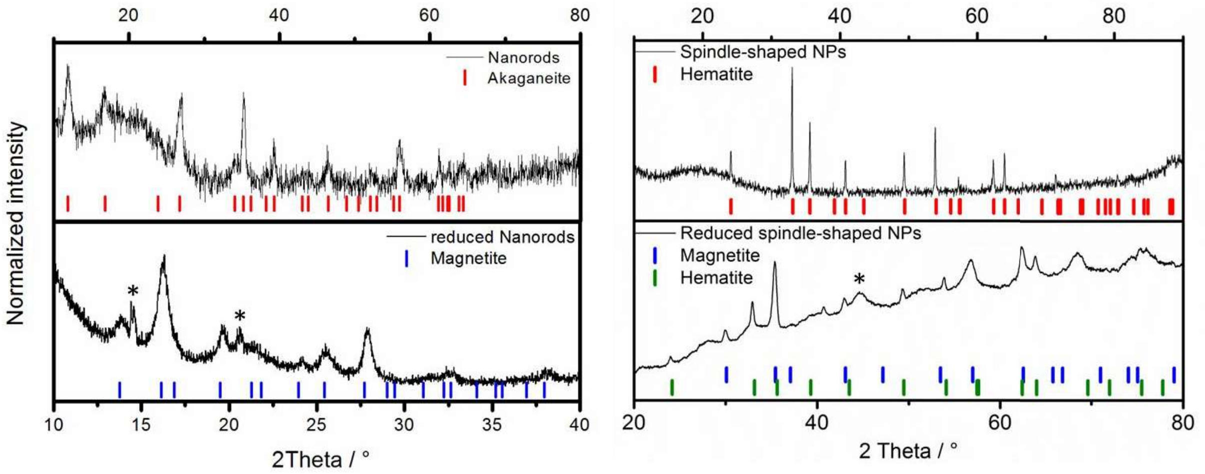

Figure 38: X-ray diffraction data of particle powder. Short nanorods (akaganeite) and their reduced counterpart. (left). Spindle-shaped particles (hematite) and their partially reduced counterpart (right). The marked (*) reflections do not belong to any iron oxide phase. They can be assigned to carbon that formed by pyrolysis.

In summary iron oxide hydroxide and iron (III) oxide particles could be reduced under preservation of morphology by thermal treatment in a high boiling solvent with a diol. Common surfactants like OA decomposed the particles to smaller spherical particles. Akaganeite requires less thermal energy to be reduced and can even react to magnetite in DBE, which then can act as a reducing agent in contrast to previous reports.[126] The reduced particles have a lower magnetization compared to bulk material due to incomplete reduction. The organic layer can partly be removed in a second step with tetramethylammonium hydroxide TMAH or high temperatures (~ 300 °C). Preservation morphology and maintaining separated particles in solution favor this method for applications in which morphology is crucial.

6. Anisotropic magnetic particles as smectic phases in hybrid liquid crystal systems

This part was done in cooperation with [redacted] research team at the [redacted] synthesized the described polymers, linked these to the magnetic, spindle-shaped particles and also did all the polymer characterization as well as the polarization optical microscope (POM) pictures. [redacted], member of the same team, assisted [redacted] with the analysis.

Klöckner, B.; Daniel, P.; Brehmer, M.; Tremel, W.; Zentel, R. Liquid Crystalline Phases from Polymer Functionalized Ferri-Magnetic Fe_3O_4 Nanorods. *J. Mater. Chem. C* **2017**, *5* (27), 6688–6696.

Liquid crystals are widely applied in technology and still form the center of many research projects. The use of magnetic particles as mesogens allows the regulation of the orientation of liquid crystal phases with magnetic fields. For this project anisotropic magnetic particles and diblock copolymers were synthesized to create a magnetic LC phase. The magnetic, spindle-shaped Fe_3O_4 particles were created by reduction of the hematite particles described in chapter 5.

Introduction

Liquid crystals

Liquid crystals (LC) or mesogenic phases were first discovered in 1888 by Friedrich Reinitzer in cholesterol derivatives. LC phases represent the intermediate between anisotropic crystalline and isotropic liquid phases. They can behave like a fluid, but also show different properties depending on the orientation which makes them an anisotropic liquid. Mesogen polymers consist of a flexible and a stiff part, often aromatic molecules, that form the crystalline phases through intermolecular interactions. The flexible part, often alkyl-chains, provides the necessary mobility in the LC phase. The external stimulus, that induces the transition from crystalline to LC to isotropic liquid, determines the kind of the LC phase. Thermotropic liquid crystals are triggered by temperature change. This behavior is above all known in organic substances. Lyotropic LC phases also depend on the concentration of mesogenic phases in a solvent.[133] Polymers with stiff chain parts are usually expected to form thermotropic LC phases but in most cases the melting temperature of the polymer is higher than the decomposition temperature, so that no LC phase can be achieved. For this reason solvent is added to the polymer system, making it a mixture of lyotropic and thermotropic systems. This increases the mobility and decreases the transition temperature to LC phase. **Figure 39** illustrates the thermotropic behavior of calamitic mesogenic liquids.[134] Coming from high temperature (right) the mesogens are randomly oriented and align along a direction (director) with lower thermal energy (left). This nematic phase is the LC phase of lowest ordering. The mesogens hardly align but are randomly positioned. Lower temperature causes order and increase in symmetry. This is seen in smectic phases and phases with highly crystalline properties.

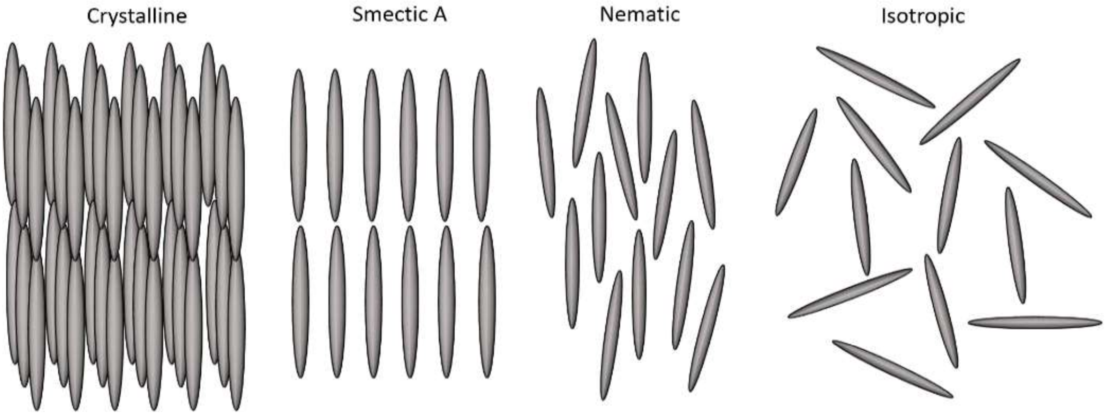

Figure 39: Different phases of anisotropic structures (stiff organic chains or inorganic rod-like particles). From left to right temperature increases while the order is decreasing from a highly symmetric crystalline phase to random orientation in isotropic phases.

Lyotropic phases are LC phases which exhibit ordering by addition of solvent. They usually contain amphiphilic molecules or polymers and in some cases anisotropic inorganic particles. Lyotropic phases with inorganic particles were first discovered in the 1920s by Hans Zocher[135] who analyzed the self-orientation of sols. Such an inorganic LC phase is called mineral liquid crystal.[136,137] The solvent provides the mobility of the particles to form nematic or higher ordered systems. On the other hand, the concentration has to maintain high so that mesophases can form. An aspect ratio of 3,5 (long axis / short axis) for the rod-like mesogens results in stable LC phases.[138,139]

Liquid crystalline phases have birefringent properties due to the anisotropic mesogenic structures. That means that the refractive index depends on the polarization as well as the direction of the incident light. Birefringence is known for many materials that have non-cubic crystal structures like calcite. Elastic materials with large anisotropic elements or under mechanical stress exhibit anisotropy which causes birefringence. Polarized light microscopy (POM) is used to analyze these phases with two orthogonal linear polarizing foils in front of and behind the sample. If the sample does not rotate the polarization vector of the incident light, no light will pass through the second foil and the observation screen remains dark. If, however, a liquid crystalline phase is present, the birefringent properties will cause a rotation of the polarization vector and light passes the filters and forms textures on the screen. A sketch of a POM is shown in **Figure 40**.

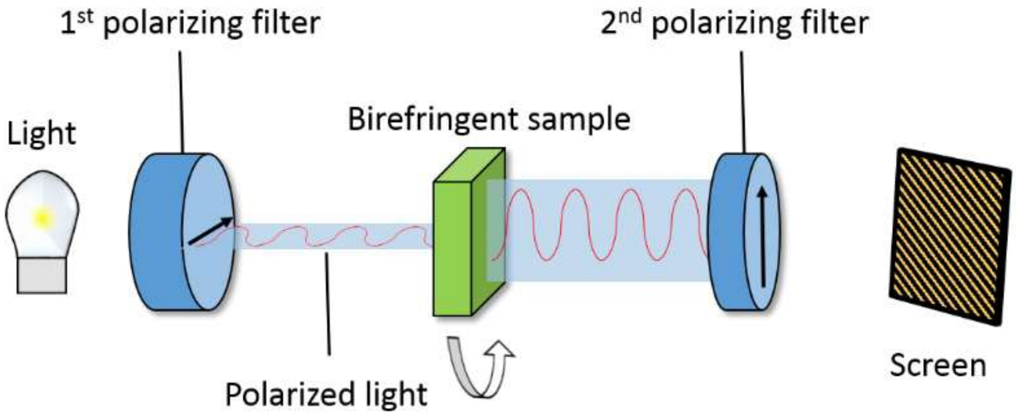

Figure 40: Set-up of a polarization microscope containing two polarizing filters of perpendicular polarization plane. A birefringend sample causes a light pattern to appear on the screen.

Mesogenic phase: Reduction of α-Fe_2O_3 particles

The rigid core of the mesogenic phase can be inorganic, anisotropic particles instead of aromatic molecule parts (mineral liquid crystal). To fulfill the requirements, the particles themselves or aggregates of particles have to be anisotropic and exhibit high aspect ratios. To form mesogenic phases the particles must be able to rotate freely but also need to be packed densely. Several known inorganic liquid crystalline phases involve V_2O_5 ribbons[140] or TiO_2 rods[141]. However, these LC-phases could not be used in electronic devices because the particles were ionically stabilized. In that case, Coulomb interactions prevent agglomeration of nanorods. For the use in electronic devices, ion free mineral liquid crystals from uncharged anisotropic nanoparticles in organic solvents are needed. Not ionically stabilized mesogens can be achieved by steric stabilization. By grafting polymers with one or multiple anchor groups to the particle surface, the “hairy rods” stabilize the anisotropic inorganic particles in solution, granting mobility of the particles in suitable solvents as depicted in Figure 41.[142–145] Furthermore, polymers allow the introduction of tunable properties like stimuli-responsive behavior or conductivity.[146,147] Multiple anchor groups on the polymer offer stable fixation and prevent unwanted detachment or ligand exchange. A long soluble polymer also offers multiple opportunities for polymer-analogue functionalization and the possibility to incorporate the hybrid material into polymer matrices as it has been demonstrated for TiO_2 rods in PMMA.[142]

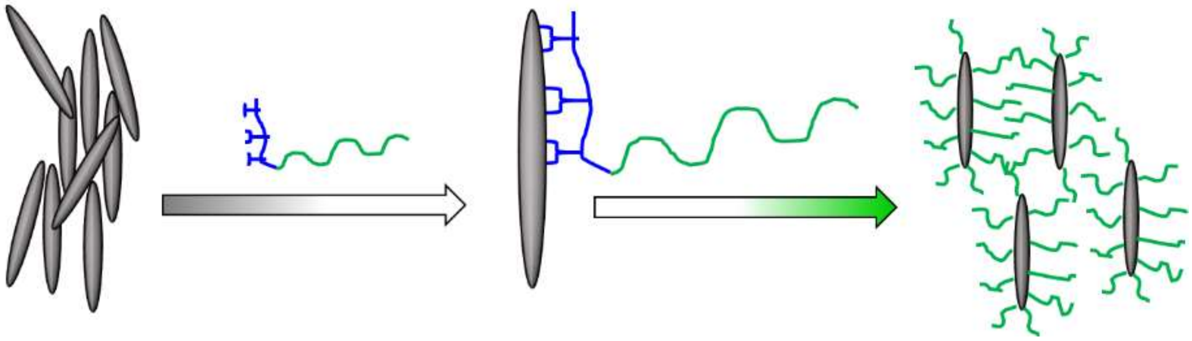

Figure 41: Hairy-rod approach to functionalize spindle-shaped nanoparticles. The block-copolymer consists of a block with anchor groups and a long tail for solubilizing purpose.

Fe_3O_4 particles have already been used alongside different polymers to form hybrid materials that can be controlled with an external magnetic field. This makes these particles an interesting compound for magnetically responsive LCs in displays or polarizers. Amphiphilic cyclodextrin vesicles,[148] double-hydrophilic core-shell polymer brushes[149] or thin elastic polymer-nanoparticles films, which exhibit switchable properties,[150] have already been described. Fe_3O_4 nanoparticles were also used in liquid crystals for their controlled alignment and magnetic addressability, as they were incorporated into hosting liquid crystalline elastomer, nematic liquid crystal matrix.[151,152]

Preparation

Polymers

The anchor block and the solubilizing block containing ester groups were synthesized by radical addition fragmentation transfer (RAFT) polymerization. For the two different solubilizing blocks, the monomers methyl methacrylate (MMA) and (diethylene glycol monomethyl ether) methacrylate (DEGMEMA) were used, respectively. The polymers were soluble in chloroform, dioxane and THF and were used as macro initiators for the second block. In a second RAFT step the anchor polymer block was synthesized from the reactive ester monomer pentafluorophenyl methacrylate. In a polymer analogue reaction the pentafluorophenyl group was substituted with dopamine hydrochloride that forms amide bonds with its primary amine group. The catechol group then provides the anchor to metal ions of the metal oxide nanoparticle surface. Successful substitution was monitored by ^{19}F-NMR and ^{1}H-NMR. All monoblock polymers and final diblock polymers were monitored by GPC (see appendix **Table 22**, **Figure 56**). Formation of amide bond could be observed by IR-spectroscopy through the disappearing of the C=O vibration of ester at 1779 cm^{-1} and the formation of C=O vibration of an amide at 1650 cm^{-1}. All spectra were collected by Benjamin Klöckner and are shown in the appendix **Figure 56**. The diblock copolymer products poly (methyl methacrylate-*b*-dopamine acryl amide) P(MMA-*b*-DOPA) and poly ((diethylenglycol monomethyl ether) methacrylate-*b*-dopamine acryl amide) P(DEGMEMA-*b*-DOPA) were used to functionalize spindle-shaped magnetic iron oxide particles.

Nanoparticles

Spindle-shaped particles as described in chapter 4 in detail were synthesized by forced hydrolysis of $FeCl_3$ over three days in boiling water in the presence of catalytic amounts of H_2KPO_4.[108,21,153] The dried particles were later reduced at 400 °C in H_2/N_2 atmosphere as described in chapter 5. The α-Fe_2O_3 particles had a length of roughly 430 nm, a short axis of around 90 nm and an aspect ratio of 4.9 : 1. After reduction the axis and aspect ratio shortened to 340 nm and 4.4 : 1, respectively (size deviation shown in **Figure 60**). Magnetization as a function of temperature and as a function of applied field was performed on powder samples with a SQUID magnetometer. The results are shown in **Figure 59**. All properties are listed in **Table 21**.

Results and Discussion

Nanoparticle functionalization

With the "hairy-rods" method the inorganic particles are solubilized by crafting the diblock copolymers to the surface in very dilute dispersion in THF. In this procedure the catechol groups of the anchor block strongly coordinate to the particles while the mobile polymer block provides solubility and reduces aggregation behavior due to steric repulsion between polymer chains. High dilution and ultrasonication are useful to prevent agglomeration of unfunctionalized particles. Surface covering was verified by solubility tests. IR and TGA measurements shown in **Figure 57** were used to characterize the polymer loading. IR data show C-H stretching vibrations at 2953 cm^{-1} from CH_2 and CH_3 groups. Additionally, carbonyl vibrations at 1653 cm^{-1} can be observed as well as C-O-C stretching vibrations at 1152 cm^{-1}. All these bands can be assigned to the polymer covering. The relative mass of P(MMA-*b*-DOPA) and P(DEGMEMA-*b*-DOPA) were 11 % and 9 %, respectively. Like the solubilizing polymer block itself, the particles could be dispersed in THF or chloroform and formed stable suspensions for days depending on the concentration. TEM images in **Figure 42** show dispersed functionalized particles in THF. No agglomerations could be observed and even a small organic corona is visible in **Figure 42** (b). SEM images of lower magnification confirm that all particles are randomly oriented without aggregation.

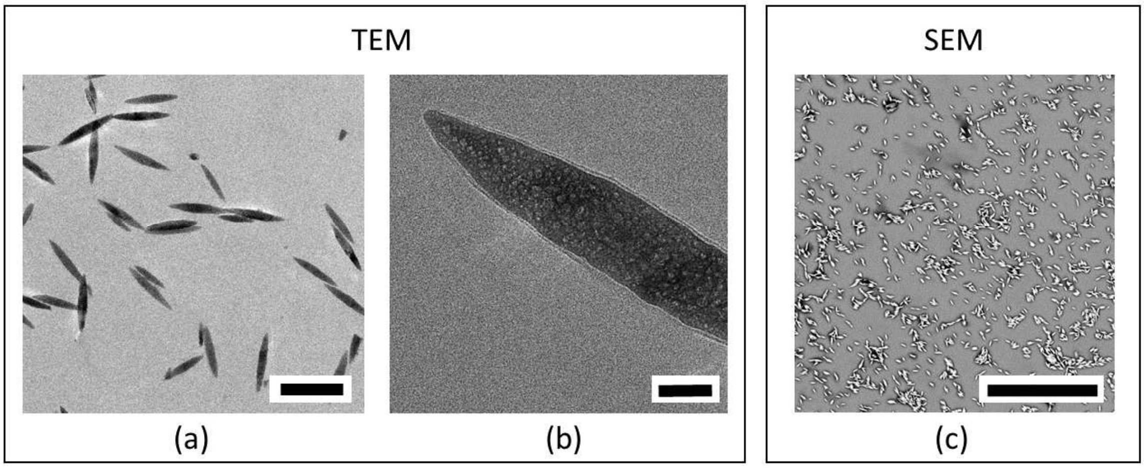

Figure 42: TEM and SEM images of polymer functionalized particles after hairy-rod approach. (a) and (b) show non-aggregated particles with a visible polymer corona. SEM image in (c) show low magnification of dispersed particles. The scalebars are 500 nm (a), 50 nm (b) and 10 µm (c).

Formation of LC phases

Dispersions of functionalized particles in THF were drop-casted on glass slides and analyzed, using the polarized optical microscope (POM) with crossed polarizers while the solvent evaporated. During evaporation birefringent areas appeared as light patterns on the screen of the POM. Such birefringent areas are well known for rod-like structures in lyotropic phases that separate into LC-phases and isotropic phases with high and low particle concentration, respectively, as seen in **Figure 43** (a). This experiment was repeated with an applied external magnetic field to observe orientation of the particles. As shown in **Figure 43** (b) the whole area appeared bright, indicating a birefringent phase. After rotating by 45°, the same area appeared dark (c). Rotating to 90° made it bright again. This indicates that the particles were all aligned in a common direction. In both experiments the solvent evaporated quickly which increased the concentration and led to the formation of the birefringent phases.

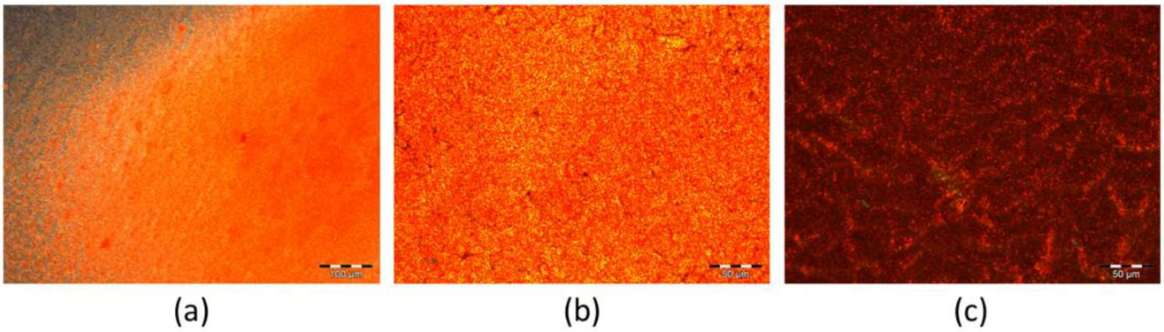

Figure 43: POM Images of dried dispersions of polymer-nanoparticle composites without (a) and with (b) an external magnetic field. Image (c) depicts (b) after a 45° rotation. Scalebars are 100 µm (a), 50 µm in (b) and (c). All images were taken by [redacted]

To avoid evaporation of the solvent, the functionalized particles were dispersed in polyethylene glycol (PEG) 400, which has a higher viscosity than THF but does not evaporate at room temperature or at high temperatures. Both polymers can be mixed in any ratio in PEG 400, making it an excellent solvent to observe the dynamic and responsive behavior of the mesophase. The investigation of the particle assembly under POM (with crossed polarizers) with and without an external field is shown in **Figure 44**. The bright colors indicate large birefringent regions. Upon applying a magnetic field, the hybrid material aligned along the field flow into long birefringent stripes with several hundred microns in length. Moving the magnet in plane around the sample forced the composite “wires” to follow the new direction of the field. The formation of these “wires” can be explained by magnetic dipole-dipole interactions between adjacent particles causing a segregation of the homogeneous dispersion into clusters and areas of low particle concentration in between (**Figure 44** II). After removing the magnetic field, the “wires” remained but randomly aligned to some degree in other directions. Switching the magnetic field on and off repeatedly transferred the system from II to III, but never back to the homogeneous distribution in I. This may be due to the magnetization of the particles inside the external field, which caused them to align along the flow and reduced interparticle distances. Because the spindle-shaped particles are quite large, they are not superparamagnetic and possess a small hysteresis loop with a remanence of 12 emu/g (see **Figure 59**). The remaining magnetization holds the particle-assembly together. The long-range interactions and the alignment of the particles inside the “wires” were analyzed with SEM and TEM. Most of the spindle-shaped particles were oriented along the long axis next to each other, as seen in the picture series (a) to (d) in **Figure 44**. The mesogenic phase that was observed under the POM can be directed with a magnet. This means that the “wires” align along the magnetic field and so do the particles inside. The magnetic axis therefore appears to be the long axis of the particle.

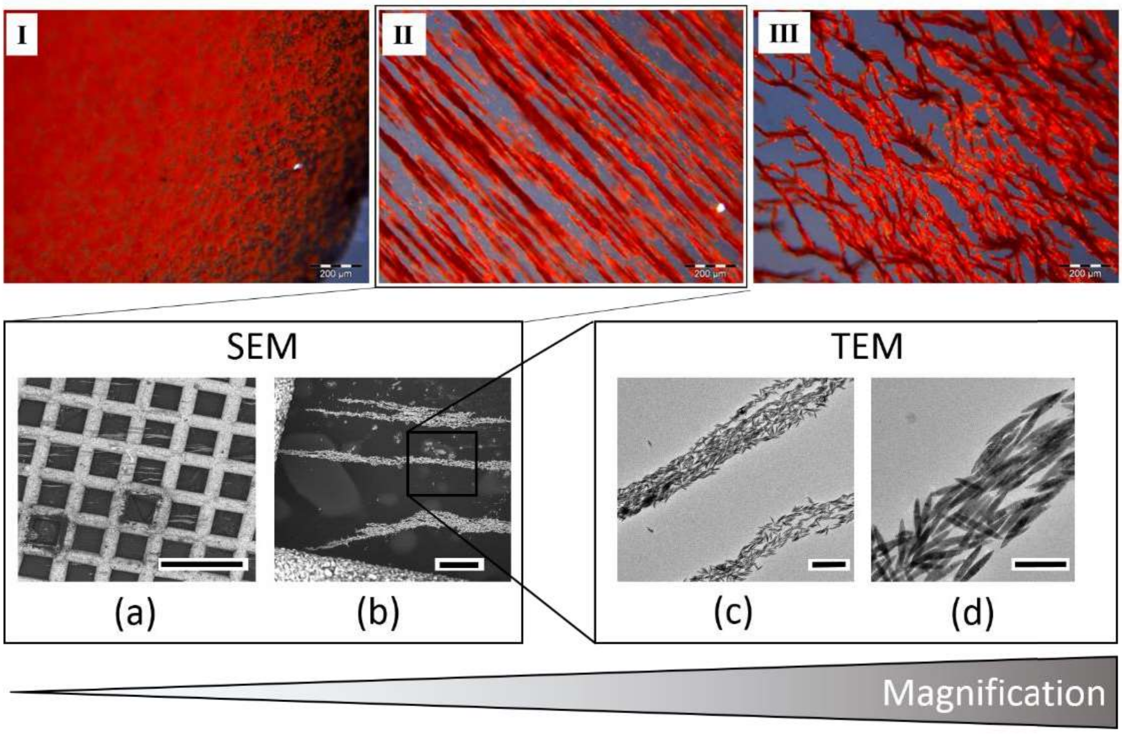

Figure 44: POM images of isotropic dispersion of mesogens in PEG (I), during in an external magnetic field (II) and after removal of the external field (III). SEM and TEM images show the orientation of the particles inside the assembly with increasing magnification. Scalebars are 200 µm (a), 10 µm (b), 2 µm (c) and 500 nm (d). Images I-III were taken by [redacted].

A demagnetizing device ("degausser") is a device that generates alternating magnetic fields thereby reducing residual magnetism to a minimum. It can be used to break the ordering and return the system to a homogeneous dispersion. **Figure 45** shows POM images of a sample of NP-polymer hybrid in PEG 400 with a magnetic field and the application of the demagnetization device afterwards. The orientation of the wire-like assemblies was destroyed using the hand demagnetizer. Repeating the process of magnetizing and demagnetizing granted identical results. These observations show the possibility to switch and control the magnetization of the nanoparticles with magnetizing or demagnetizing external fields.

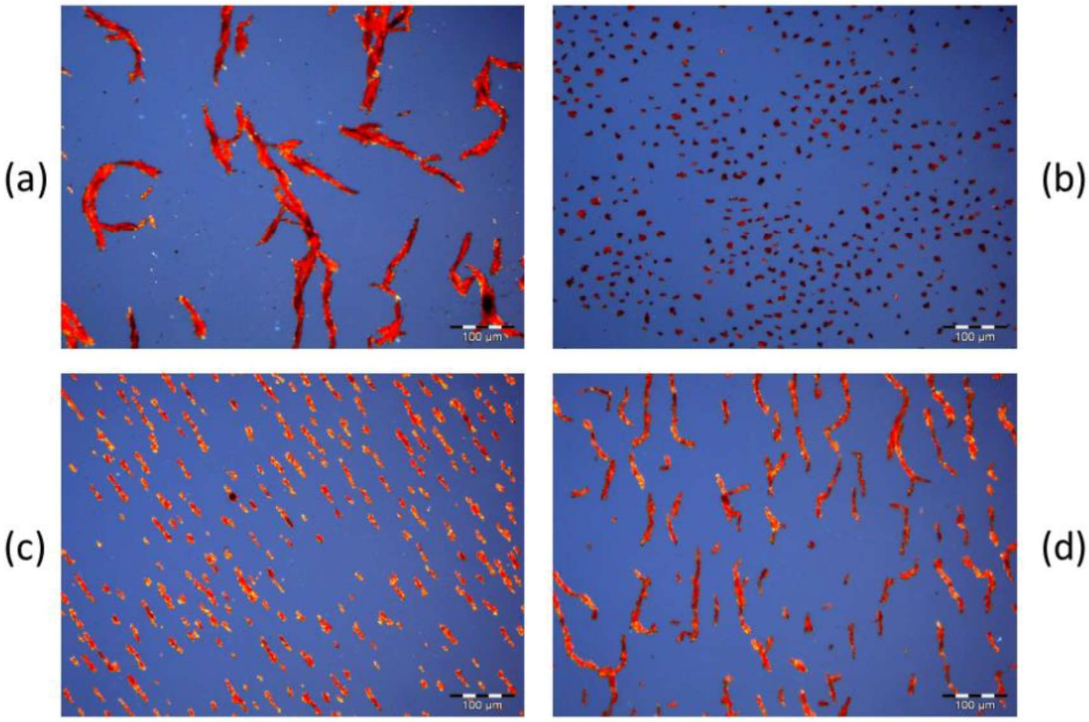

Figure 45: POM images of aligned particle chains after magnetization (a) and after the use of the degausser (b). (c) Shows the realignment when the field is switched back on. After the field is removed a second time (d) the structures are similar to (a). All images were taken by [redacted].

Conclusion

This project demonstrates the application of spindle-shaped magnetic nanoparticles as mesogenic phases in liquid crystal systems. Utilizing diblock copolymers containing a catechol-carrying anchor block and a solubilizing hydrophobic block in a hairy-rod approach form stable colloidal suspensions of nanoparticles in THF or PEG 400. During evaporation of organic solvents like THF the formation of birefringent areas with high particle concentration can be observed under polarization microscope. PEG 400 is used as a non-evaporating matrix for the composite material and allowed reorientation of the anisotropic particles. Applying a magnetic field segregate the homogeneous dispersion and long wire-like structures form. These “wires” are all aligned along the magnetic field flow. Removal of the magnet only slightly disturbs the orientation of the wires. To turn the system back into the original homogeneous state a handheld demagnetizer can be used. The process of magnetization and demagnetization is reversible. This allows the formation of magnetically controlled liquid crystals with inorganic nanoparticles as mesogenic phases.

7. Spindle shaped α-Fe_2O_3 in PVA fibers

This research has been done in cooperation with [redacted] research group at [redacted] He was doing the fluorescence measurements. [redacted] from the [redacted] were responsible for the electrospinning process, the bacteria tests, the wound healing experiments and the contact angle measurements.

Hu, M.; Korschelt, K.; Daniel, P.; Landfester, K.; Tremel, W.; Bannwarth, M. B. Fibrous Nanozyme Dressings with Catalase-like Activity for H_2O_2 Reduction to Promote Wound Healing. *ACS Appl. Mater. Interfaces* **2017**.

Introduction

Electrospinning is a process that creates meshes of thin polymer fibers. In this procedure, a polymer is dissolved in a solvent with a high polarity, preferably water or acetonitrile, and then sprayed through a tiny notch and will be accelerated in an electrical field of several kV towards an electrode, as shown in **Figure 46**. The solvent evaporates during the flight leaving behind the thin polymer fiber. The impressed voltage determines the speed of the fiber and thereby its thickness. The particles, that are included in the polymer solution, will later be imbedded in the polymer fibers. Due to the spinning process through a tiny nozzle, anisotropic particles will arrange parallel inside the polymer fibers and the long axis parallel to the direction of the fiber. The fibers are randomly oriented on the target. A common polymer for the electrospinning process is poly(vinyl alcohol) (PVA). Because the polymer is merely drying on the target electrode, the fiber mesh will be water-soluble. To ensure applications in aqueous media, the PVA is cross-linked in a second step. This facile method of electrospinning is suitable for small amounts of fibers on variable geometric forms.[154–156]

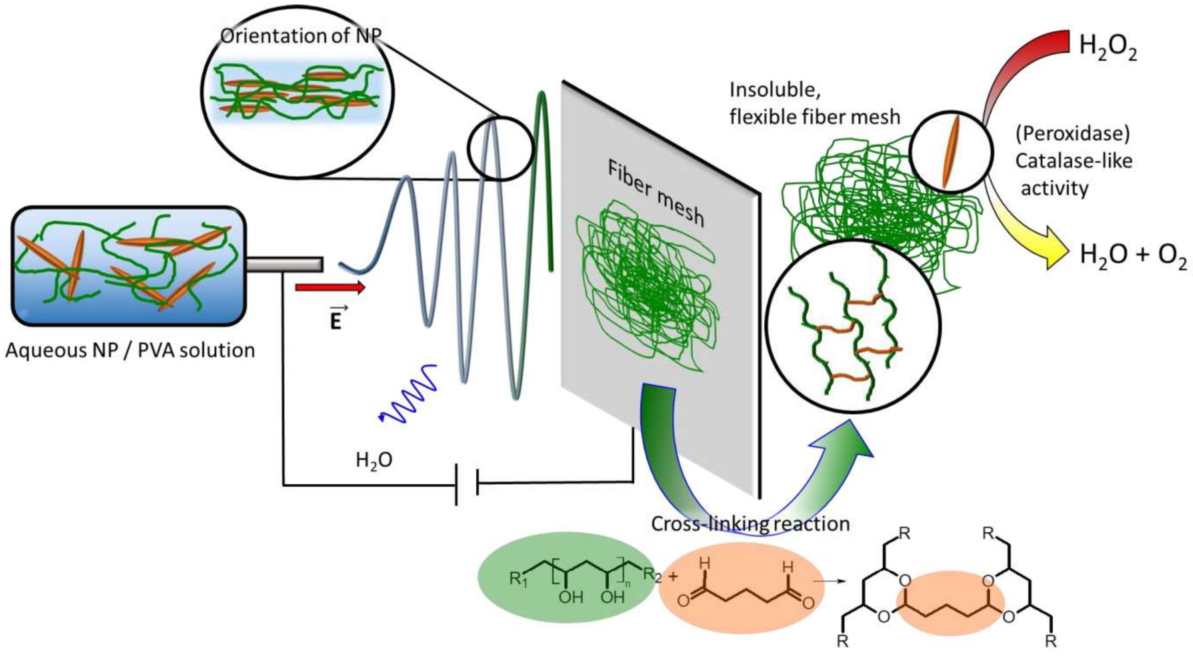

Figure 46: Schematic illustration of electrospinning process. The aqueous solution is accelerated in an electric field towards an electrode covered with aluminum foil. Water evaporates during the flight and the NP orient along the resulting PVA fiber. The mesh is then treated with an α,ω-dialdehyde which cross-links the PVA fibers.

Here electrospinning was used to make meshes of PVA fibers with different concentrations of spindle-shaped nanoparticles. It was tested if the particles keep their catalytic properties for peroxidase-like reactions. Catalytically active fiber meshes could be applied in wound dressing material.

Wound dressing materials should improve the healing process by creating an environment that remains moist and oxygen rich.[157] They also should prevent infections and support the formation of new skin tissue.[158] Reactive oxygen species, like H_2O_2 and its oxidized redox-partner O_2, are two important metabolites, which are involved in wound healing process. Reactive H_2O_2 in high concentration inhibits the wound healing process due to the prevention of the connective tissue formation.[159] O_2 on the other hand improves the course of healing.[160] Therefore, a dressing material that decreases concentration of reactive H_2O_2 while simultaneously increasing O_2 levels through catalytic conversion seems to be applicable for e.g. a band-aid.[161]

There are natural enzymes, like peroxidase and catalase that convert reactive oxygen species (ROS) like H_2O_2 into O_2 (triplet oxygen). But extraction of natural enzymes is costly and the enzymes need to be stored under cooled conditions to ensure their functionality.[7,162,163] Imitating the functionality of natural enzymes with inorganic particles has become a large field of study over the past decades.[164–168] Unlike natural enzymes these nano-scale enzyme mimics, also known as “nanozymes”[7], are robust, easy to produce in large scale and sometimes exhibit even higher reactivity than their natural counterpart.[163,169] In contrast to natural enzymes, that normally have one site, inorganic nanoparticles provide high numbers of catalytic active ions at the particle surface. The downside of higher reactivity is the loss of selectivity compared to enzymes.[170]

Hematite NPs can be applied as nanozymes to reduce H_2O_2 levels by converting it to H_2O and O_2.[171,172] Hematite is non-toxic and a stable oxide. The rather large sizes of the synthesized particles provide an excellent material for wound treatment applications because they cannot be taken up by cells and remain inside the fibers (**Figure 46**).

Electrospinning techniques have already been used to fabricate wound dressing materials.[156,173] The fibers exhibit high surface-to-volume ratios and porosity, which enables them to absorb high amounts of water and thus provide the necessary surface for catalytic reactions on the particles in the membrane.

Results and Discussion

The α-Fe_2O_3 particles were prepared by forced hydrolysis of $FeCl_3$ in a one liter round bottom flask under reflux for three days. The product was precipitated with THF in several small aliquots, filtered and dried. The particles were then divided into three batches to create dispersions of 5 wt.%, 25 wt.%, and 50 wt.% in water. The high concentrated samples 25 wt.% and 50 wt.% were later diluted to 15 wt.% and 25 wt.% for electrospinning procedures because the starting concentrations were too high for electrospinning. The particles had no surface ligands, but were readily dispersible in water, allowing a direct, unhindered access of substrate molecules to the active surface. Electrospinning was done by Minghan Hu at the MPIP in Mainz. For TEM analysis a small amount of fibers was directly spun onto a TEM sample holder (copper mesh with carbon foil) during the process. Four meshes were prepared on aluminum foil containing 0 wt.%, 5 wt.%, 15 wt.%, and 25 wt.% Fe_2O_3 particles. The color of the mesh correlated with the concentration and became darker from low to high loading. They resembled the color of the dry particle powder at high concentrations while pure PVA remained colorless. All meshes were cross-linked under equal conditions with 1,5-pentandial (**Figure 46**) to enable the stability in water by reacting with –OH groups (see **Figure 46**). The polymer meshes were cut in half and one half again into four eighths as shown in **Figure 47**. The composite was removed from the foil and washed with deionized water several times to remove remaining crosslinking agent and unbound PVA and NPs. Because after washing the composition of the fibers differs from the starting concentrations the batches will be named “low”, “medium” and “high” corresponding to the starting particle concentrations 5 wt.%, 15 wt.%, and 25 wt.% respectively. The exact mass was determined by TGA (**Figure 49**). The particles in PVA will be called “NP@PVA” for easier description. Small amounts of the meshes were analyzed with IR (in KBr) to ensure that hematite is present in all fibers.

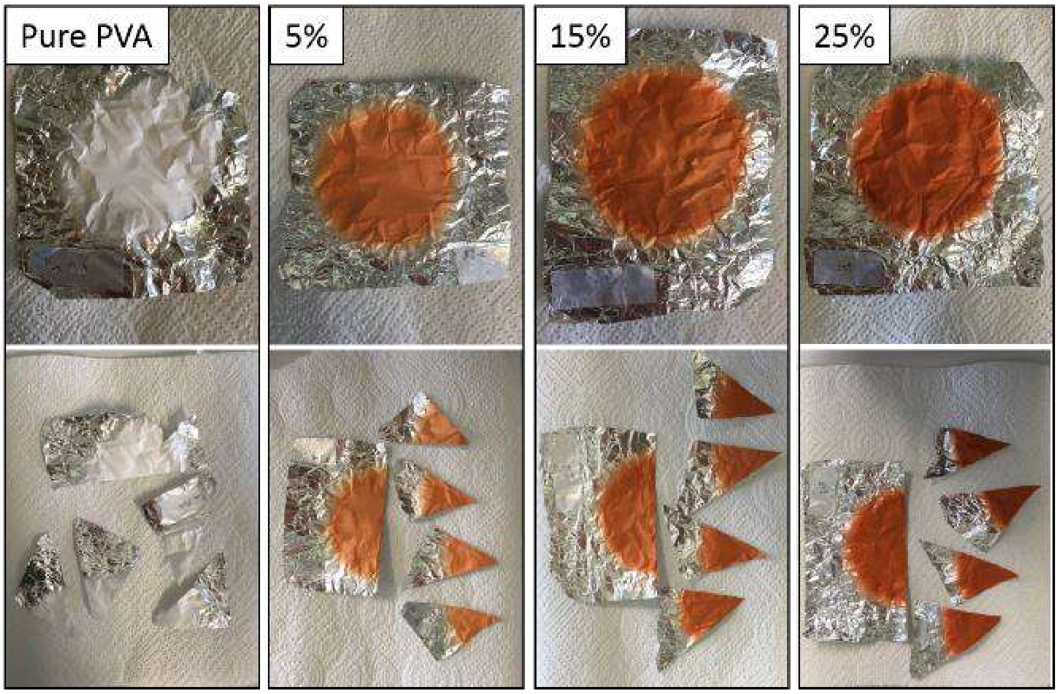

Figure 47: Cross-linked PVA fiber meshes from NP dispersions with different concentration.

The crystalline phase of the particles is pure hematite as proven by the powder XRD shown in **Figure 48** B. The prepared hematite NPs, PVA and “NP@PVA” were analyzed using transmission electron microscopy and are shown in **Figure 48**. Increasing the concentration of the spun dispersion will increase the concentration of particles inside the fibers as shown in the **Figure 48** C. A variation of the NP concentration did not affect the orientation of NPs inside the fibers. Some agglomerates are visible for the samples of high concentration.

When the dry NP@PVA samples were wetted with water, they crumbled and formed little wet droplets. This was observed during sample preparation in a wet medium. The size of those droplets increased from “low” to “high” particle loading. Pure PVA holds little water and formed a small wet drop when taken out of solution. The higher the particle concentration the bigger the wet composite samples were. This demonstrated the high wettability and hydrophobic character of the meshes only.

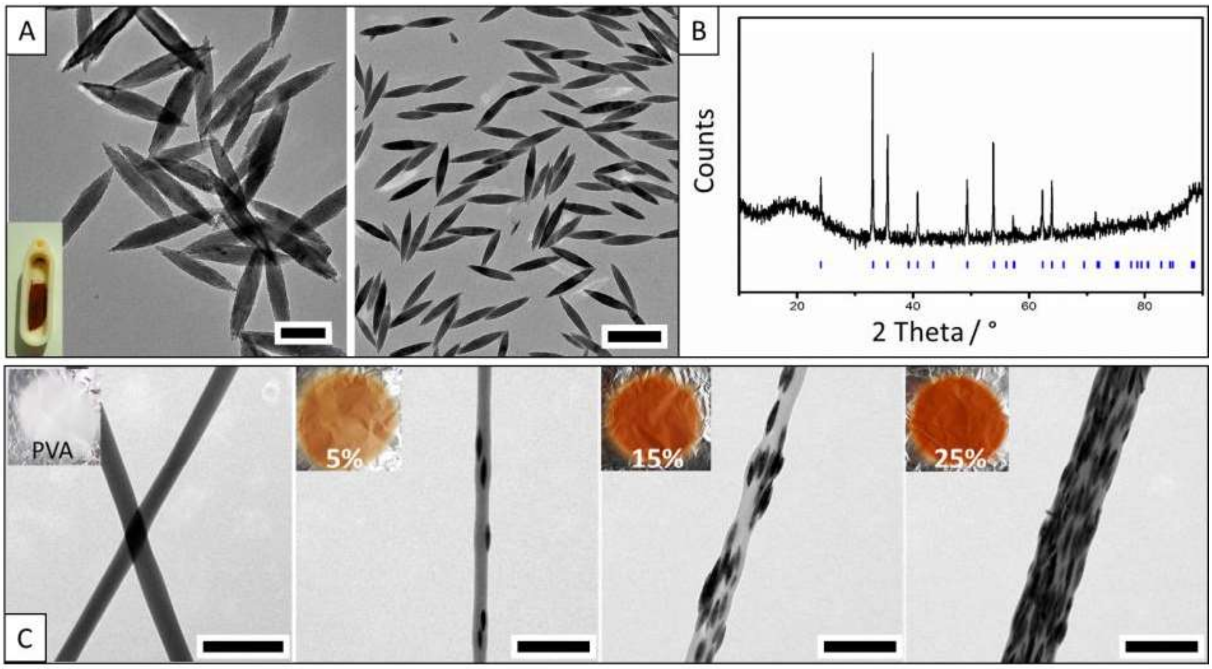

Figure 48: TEM images of synthesized Fe_2O_3 NPs. Scalebars 200 nm and 500 nm left and right respectively (A). Powder XRD pattern (B). TEM images of fibers with different particle concentrations (C). Note that these TEM samples were prepared directly during the electrospinning process and are therefore not cross-linked. TEM images in (C) taken by [redacted]. Scalebars equals 1000 nm for every image in (C).

Figure 49 shows SEM images of the fibers before and after water immersion (A and B). The fiber structure was preserved in aqueous environment because the cross-linking prevents solvation. **Figure 49** C shows NP@PVA fibers with low, medium and high particle concentration in aqueous media. The meshes swelled stronger the more particles are inside the fibers. **Figure 49** D illustrates the wettability tests. Due to the good wettability of the PVA meshes, a water droplet added to the surface spread completely within 20 s. FTIR analysis probed the permanent entrapment of the NP after the washing process (**Figure 49** E). In all spectra except that of pure PVA, bands at 479 cm^{-1} and 535 cm^{-1} could be assigned to Fe-O vibrations characteristic for hematite.[115] This confirmed that NPs were present in all fibers. Characteristic bands for PVA can be observed at 1095 cm^{-1} and 1437 cm^{-1} corresponding to C-O-C vibrations of cross-linked PVA and C-H bending vibrations respectively.[174] **Figure 49** F plots all thermogravimetric measurements of pure NP, pure PVA and all three different loadings. The mass after the heating process at 700 °C was normalized between 0 % for pure NP and 100 % for PVA. The curves look similar for all samples. There is a larger mass loss between 250 °C and 450 °C which can be correlated to the decomposition of most of the PVA. From pure PVA to "high" the decrease in mass starts at lower temperatures, respectively. A possible explanation is the increasing particle content that accelerates the heating and decomposition of the polymer. The observed weight loss before 250 °C occurs due to the evaporation of water. You can see clearly that the actual particle loading is higher than the starting concentration of nanoparticles would allow. A possible explanation would be the loss of PVA due to incomplete cross-linking and washing. The cross-linking might be hindered by the many particles inside the fiber. The actual loading is 71 wt.%, 58 wt.%, and 19 wt.% for high, medium and low concentrations, respectively.

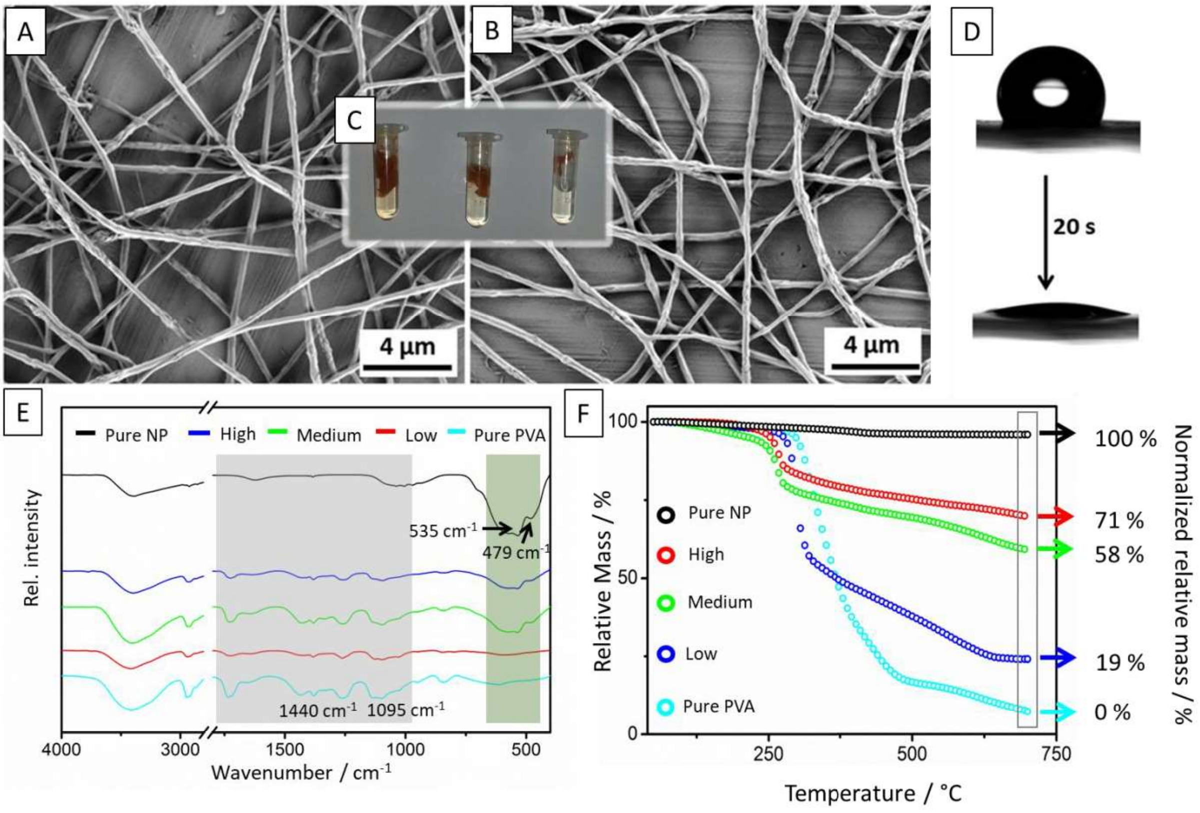

Figure 49: Fibers before and after cross-linking with 1,5-pentadial in (A) and (B)respectively. PVA with high, medium and low particle loading swell differently in water. The cross-linked fibers all exhibit hydrophilic surfaces as seen in contact-angle measurements (D). IR measurements of all fibers and the pure NP are plotted in (E). Thermogravimetric measurements of all samples are shown in (F). Images (A), (B) and (D) taken by [redacted]

To test the catalase-like catalytic activity, small, equally cut areas of the meshes were placed inside a 96 wellplate and 3-(N-morpholino)propansulfone acid (MOPS) buffer was added. To monitor the degenerateration of H_2O_2 an europium tetracycline (EuTc) based fluorescence catalase assay was used.[175] The structure of tetracycline is shown in **Figure 50** A together with the possible reaction paths during the reduction of H_2O_2. EuTc has no fluorescent activity but EuTc-H_2O_2 is highly fluorescent. After adsorption of H_2O_2 to the EuTc complex the fluorescent EuTc-HP (hydrogen peroxide) complex forms, which has an emission maximum at $\lambda_{max} = 620$ nm (**Figure 51** A). The complex was previously formed by incubating EuTc solution with H_2O_2 for several minutes.The EuTc-H_2O_2 solution was rapidly added in the end and the fluorescence at the emission maximum at $\lambda_{max} = 620$ nm was monitored over a period of 10 minutes. For every NP concentration four pieces of the same batch were measured rapidly. Monitoring the change in fluorescence intensity at 620 nm over a defined time period directly shows the catalase-like activity of a tested material.[175]

Catalase is a native enzyme that facilitates the decomposition of H_2O_2, forming O_2 and H_2O. After the measurement the composite was removed from the sample holder and washed with water several times.

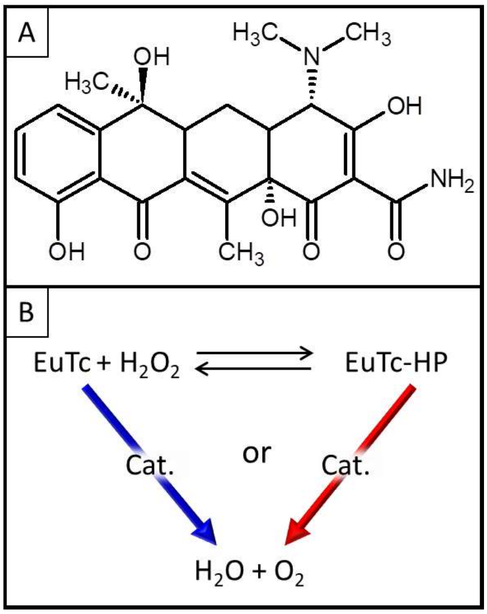

Figure 50: (A) Tetracycline molecule. (B) Both reactions are possible. Either the catalyst induces the reaction of the H_2O_2 bound to the europium tetracycline complex (EuTC-HP) or of the free H_2O_2 which is in equilibrium with the complex, red and blue route respectively.

After adsorption of H_2O_2 to the EuTc complex the fluorescent EuTc-HP (hydrogen peroxide) complex forms, which has an emission maximum at $\lambda_{max} = 620$ nm (**Figure 51** A). If H_2O_2 is decomposed either as the free H_2O_2 in solution or as a ligand in the EuTc-HP complex (**Figure 50** B) the fluorescence intensity decreases rapidly. The results are plotted in **Figure 51** D. Pure NP and the native catalase enzyme were used in control measurements (**Figure 51** C and B respectively). In presence of the native catalase enzyme H_2O_2 is decomposed, resulting in the expected decrease of fluorescence intensity. With higher enzyme concentrations the obsered curves start at lower values and gradually decrease faster. Different first measured values can be explained by he fast decomposition reaction of H_2O_2 catalyzed by native enzyme. A similar trend is observed for the pure particles in different amounts, when the fluorescence intensity decreases with the same behavior. NP@PVA meshes showed catalase-like activity while pure PVA fibers without NPs exhibit no significant effect. Hematite NP concentration related to higher activity.

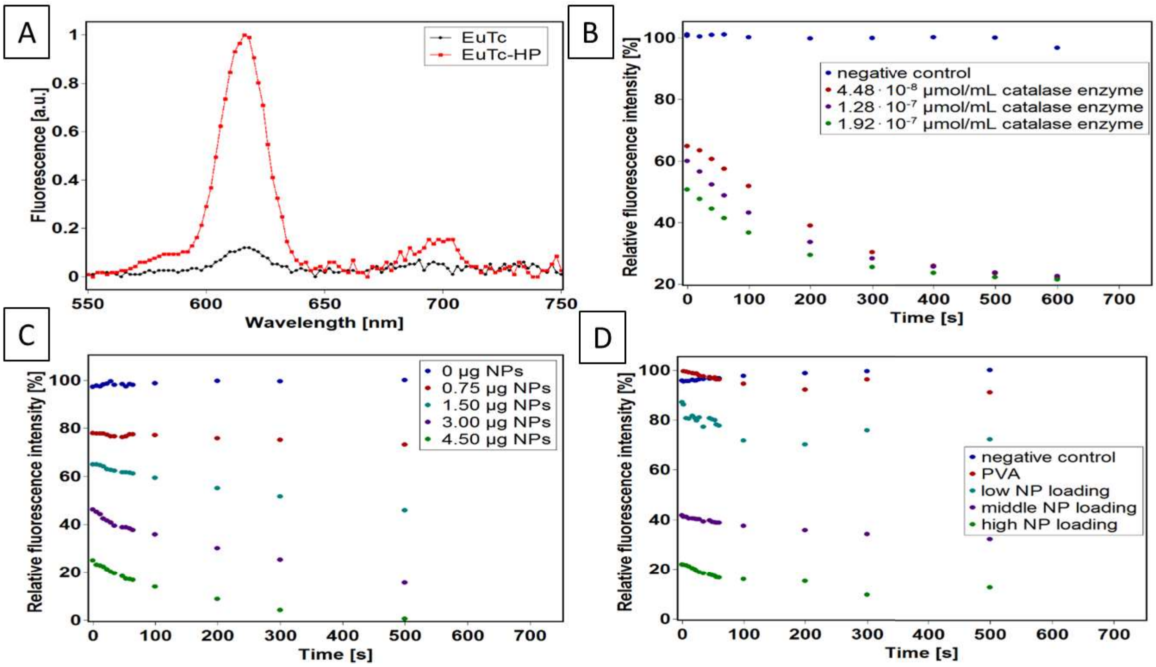

Figure 51: (A) Fluorescence scan ($\lambda_{ex} = 405$ nm) of the EuTC-HP complex with a maximum signal at $\lambda_{max} = 620$ nm. H_2O_2 decomposition, recorded at λ_{max}, catalyzed by the natural catalase enzyme (B), the pure hematite NP (C) and the prepared NP/PVA meshes (D). All Graphs were plotted by [redacted]

By plotting the fluorescence intensity of every sample after five minutes of reaction time the dependence on the concentration was further analyzed (**Figure 52**). This is shown for the natural enzyme, the hematite NPs and the NP@PVA meshes. H_2O_2 was decomposed faster the more catalyst was present in the sample. With the highest NP loading the fluorescence intensity went down to 9.5 % (related to a 100 % control). In a catalase-like reaction hydrogen peroxide is decomposed to water and molecular oxygen as described in the following equation

$$2\ H_2O_2 \rightarrow 2H_2O + O_2$$

Using an oxygen sensitive electrode the formation of molecular oxygen as one product of the catalase-like reaction was monitored (**Figure 52** D). Every NP@PVA sample generated molecular oxygen, which led to the conclusion that the catalytic mechanism is catalase-like.

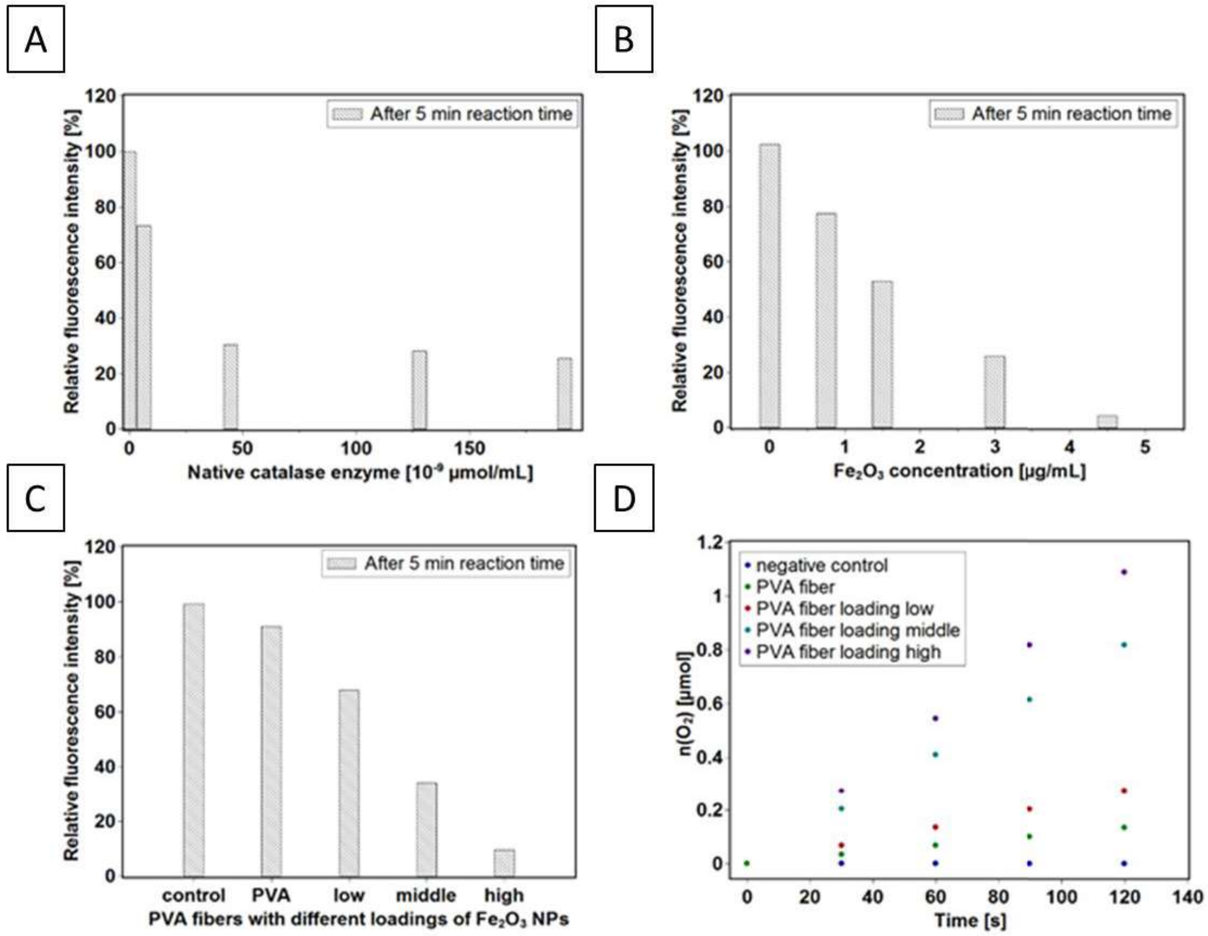

Figure 52: Fluorescence intensity after 5 minutes with different concentrations of (A) the natural enzyme, (B) pure NPs, (C) NP@PVA. The gradual formation of oxygen was measured with an oxygen sensitive electrode. This was performed only for the NP@PVA meshes (D). All graphs were plotted by [redacted]

A fibroblast cell line NIH-3T3 was used to investigate wound healing properties of NP@PVA meshes. For these experiments the high loading was used. The cells were incubated overnight with meshes previously incubated with H_2O_2. As depicted in **Figure 53** the NP@PVA meshes showed cell viability almost as high as the negative control sample. Pure PVA meshes had no protecting effect. This confirmed the degradation of harmful H_2O_2 by hematite NPs.

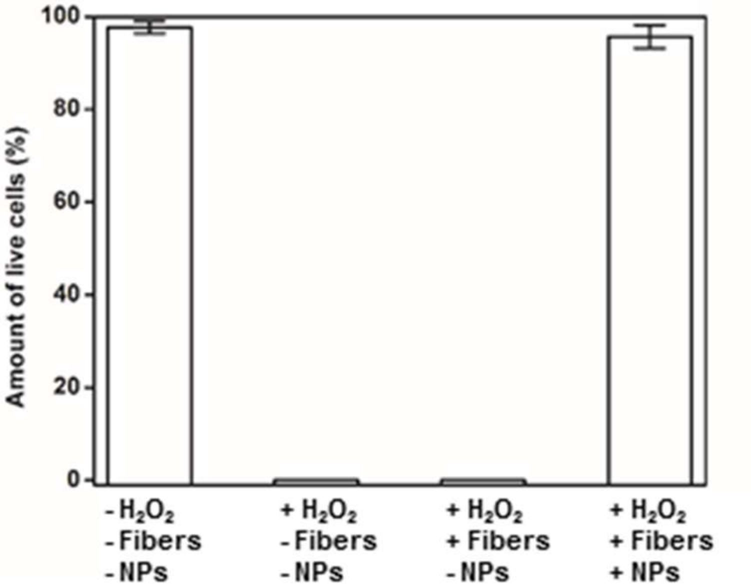

Figure 53: From left to right the cell viability was probed for control sample, H_2O_2, PVA in H_2O and NP@PVA in H_2O. Graph plotted by [redacted].

Conclusion

The spindle-shaped hematite nanoparticles were imbedded in PVA fibers through an electrospinning process. To ensure insolubility of the fiber meshes the PVA was cross-linked with 1,5-pentadial. Four meshes with different particle loading concentrations (pure PVA, low, medium and high) have been prepared. The catalase-like catalytic activity of the pure NP and the fiber meshes were tested using a fluorescent assay with a europium tetracycline complex. It could be shown that the NP remain catalytically active inside the cross-linked PVA stings. Using an oxygen sensitive electrode the formation of oxygen could be proven which shows that the peroxidase-like activity is in fact similar to that of catalase. With the highest concentrations after five minutes a reduction of the fluorescence intensity down to 9.5 % compared to the negative sample could be achieved. These NP@PVA meshes may find possible applications in bandages that support wound healing by reducing H_2O_2 levels and increasing O_2 concentrations, thus protecting the cells.

V. CONCLUSION

In this work spherical and spindle-shaped iron oxide particles were prepared. It was shown that size and size distribution of spherical particles strongly depend on the solvent and the corresponding reaction temperature. The particles were functionalized with different ligands like DHCA TMAH and PDAm. The functionalization with DHCA was improved by pretreating the particles with TMAH, which replaces all OA form the synthesis. The catechol-carrying DHCA could also be substituted by TMAH in a large excess. This opened up a different view on the catechol-nanoparticle bonding.

Particles with different ligands fixed inside a matrix showed different magnetic behavior depending on the ligand. PDAm, a polymer containing multiple catechol anchor groups, caused the greatest reduction of the saturation magnetization at 3 T by approximately 50 % and also showed the greatest content of nonmagnetic iron in the Mössbauer spectra. This suggests that the polymer attaches to the particles via the catechol units and reduces the outer particle shell from γ-Fe_2O_3 maghemite to magnetite Fe_3O_4 with a magnetic moment opposite to that of the core. Thus the reduction of the total magnetization of nanoparticles through chemical functionalization could be achieved.

Spindle-shaped hematite particles were prepared in water by forced hydrolysis. It was found that the formation was sensitive to variables like stirring speed and reaction volume. Larger volumes led to larger particles and different stirring speed affects the average size and distributions in a non-linear fashion.

It could also be shown that the precursor akaganeite particles that form the hematite spindles can be acquired for higher the iron salt and phosphate concentrations.

Due to the activity as a peroxidase-like catalyst the hematite particles were incorporated in PVA fibers by electrospinning. The PVA was cross-linked to form a water-insoluble polymer. Those fibers showed peroxidase like activity and also showed cell protecting properties. Such NP@ PVA meshes have potential use as a wound healing substrate because of the H_2O_2 content-reducing properties.

The spindle-shaped particles could be reduced by hydrogen gas or an alkane diol at high temperatures in an Al_2O_3 crucible or in a high boiling organic solvent, respectively. Hematite as well as akaganeite particles could be reduced to magnetite. The magnetic particles were used as a mesogenic phase to form lyotropic liquid crystalline phases with different polymers. Those birefringent phases could be stabilized in PEG and the orientation could be controlled by an external magnetic field. The magnetic dipole-dipole interaction caused the particles to remain in agglomerated strings until a demagnetizing field is applied. This behavior was reversible and repeatable. This result is of interest with regard to magnetically switchable liquid crystal systems.

VI. LITERATURE

(1) Coey, J. M. D.; Venkatesan, M.; Xu, H. Introduction to Magnetic Oxides. In *Functional Metal Oxides: New Science and Novel Applications*; Ogale, Satishchandra B.; Venkatesan, Thirumalai V.; Blamire, M. G., Ed.; Wiley-VCH Verlag GmbH & Co. KGaA, 2013; pp 3–50.

(2) Sattler, K. D. *Nanoparticles and Quantum Dots*; 2013; Vol. 53.

(3) Niederberger, M.; Pinna, N. *Metal Oxide Nanoparticles in Organic Solvents*; 2009.

(4) Lu, A.-H.; Salabas, E. L.; Schüth, F. Magnetic Nanoparticles: Synthesis, Protection, Functionalization, and Application. *Angew. Chem. Int. Ed. Engl.* **2007**, *46* (8), 1222–1244.

(5) Barber, A. H.; Lu, D.; Pugno, N. M. Extreme Strength Observed in Limpet Teeth. *Interface* **2015**, 0–5.

(6) Sanchez, C.; Boissiere, C.; Cassaignon, S.; Chaneac, C.; Durupthy, O.; Faustini, M.; Grosso, D.; Laberty-Robert, C.; Nicole, L.; Portehault, D.; Ribot, F.; Rozes, L.; Sassoye, C. Molecular Engineering of Functional Inorganic and Hybrid Materials. *Chem. Mater.* **2013**, *26* (1), 221–238.

(7) Wei, H.; Wang, E. Nanomaterials with Enzyme-like Characteristics (Nanozymes): Next-Generation Artificial Enzymes. *Chem. Soc. Rev.* **2013**, *42* (14), 6060–6093.

(8) Klöckner, B.; Daniel, P.; Brehmer, M.; Tremel, W.; Zentel, R. Liquid Crystalline Phases from Polymer Functionalized Ferri-Magnetic Fe_3O_4 Nanorods. *J. Mater. Chem. C* **2017**, *5* (27), 6688–6696.

(9) Dumestre, F. Superlattices of Iron Nanocubes Synthesized from $Fe[N(SiMe_3)_2]_2$. *Science.* **2004**, *303* (5659), 821–823.

(10) Mascolo, M.; Pei, Y.; Ring, T. Room Temperature Co-Precipitation Synthesis of Magnetite Nanoparticles in a Large pH Window with Different Bases. *Materials (Basel).* **2013**, *6* (12), 5549–5567.

(11) Rodríguez-Cabo, B.; Rodil, E.; Soto, A.; Arce, A. Preparation of Metal Oxide Nanoparticles in Ionic Liquid Medium. *J. Nanoparticle Res.* **2012**, *14* (7), 939.

(12) Liu, X.; Duan, X.; Qin, Q.; Wang, Q.; Zheng, W. Ionic Liquid-Assisted Solvothermal Synthesis of Oriented Self-Assembled Fe_3O_4 Nanoparticles into Monodisperse Nanoflakes. *CrystEngComm* **2013**, *15* (17), 3284.

(13) Wang, Y.; Yang, H. Synthesis of Iron Oxide Nanorods and Nanocubes in an Imidazolium Ionic Liquid. *Chem. Eng. J.* **2009**, *147* (1), 71–78.

(14) Laurent, S.; Forge, D.; Port, M.; Roch, A.; Robic, C.; Vander Elst, L.; Muller, R. N. Magnetic Iron Oxide Nanoparticles: Synthesis, Stabilization, Vectorization, Physicochemical Characterizations, and Biological Applications. *Chem. Rev.* **2008**, *108* (6), 2064–2110.

(15) Wichmann, K. Synthese, Funktionalisierung Und Anwendung von Magnetischen Eisenoxidnanopartikeln, Dissertation, Mainz, 2016.

(16) Lynch, J.; Zhuang, J.; Wang, T.; Lamontagne, D.; Wu, H.; Cao, Y. C. Gas-Bubble Effects on the Formation of Colloidal Iron Oxide Nanocrystals. *J. Am. Chem. Soc.* **2011**, *133* (32), 12664–12674.

(17) Kim, D.; Lee, N.; Park, M.; Kim, B. H.; An, K.; Hyeon, T. Synthesis of Uniform Ferrimagnetic Magnetite Nanocubes. *J. Am. Chem. Soc.* **2009**, *131* (2), 454–455.

(18) Sajanlal, P. R.; Sreeprasad, T. S.; Samal, A. K.; Pradeep, T. Anisotropic Nanomaterials: Structure, Growth, Assembly, and Functions. *Nano Rev.* **2011**, *2*, 1–62.

(19) Kovalenko, M. V; Bodnarchuk, M. I.; Lechner, R. T.; Hesser, G.; Schäffler, F.; Heiss, W. Fatty Acid Salts as Stabilizers in Size- and Shape-Controlled Nanocrystal Synthesis: The Case of Inverse Spinel Iron Oxide. *J. Am. Chem. Soc.* **2007**, *129* (20), 6352–6353.

(20) Özdemir, Ö.; Dunlop, D. J.; Berquo, T. S. Morin Transition in Hematite: Size Dependence and Thermal Hysteresis. *Geochemistry, Geophys. Geosystems* **2008**, *9* (10).

(21) Reufer, M.; Dietsch, H.; Gasser, U.; Grobety, B.; Hirt, a M.; Malik, V. K.; Schurtenberger, P. Magnetic Properties of Silica Coated Spindle-Type Hematite Particles. *J. Phys. Condens. Matter* **2011**, *23* (6), 65102.

(22) Gubin, S. P. *Magnetic Nanoparticles*; Gubin, S. P., Ed.; Wiley-VCH Verlag GmbH & Co. KGaA: Weinheim, Germany, 2009.

(23) Bødker, F.; Hansen, M.; Koch, C.; Lefmann, K.; Mørup, S. Magnetic Properties of Hematite Nanoparticles. *Phys. Rev. B* **2000**, *61* (10), 6826–6838.

(24) Blake, R. L.; Hessevick, R. E.; Zoltai, T.; Finger, L. W. Refinement of the Hematite Structure. *Am. Mineral.* **1966**, *51*, 123–129.

(25) Alexe, M.; Ziese, M.; Hesse, D.; Esquinazi, P.; Yamauchi, K.; Fukushima, T.; Picozzi, S.;

Gösele, U. Ferroelectric Switching in Multiferroic Magnetite (Fe_3O_4) Thin Films. *Adv. Mater.* **2009**, *21* (44), 4452–4455.

(26) Shokrollahi, H. A Review of the Magnetic Properties, Synthesis Methods and Applications of Maghemite. *J. Magn. Magn. Mater.* **2017**, *426*, 74–81.

(27) Prewitt, Barry; Wechsler, A.; H. Lindsley, Donald; T., C. Crystal Structure and Cation Distribution in Titanomagnetites ($Fe_{3-x}Ti_xO_4$). *Am. Mineral.* **1984**, *69*, 754–770.

(28) Morales, M. P.; Veintemillas-Verdaguer, S.; Montero, M. I.; Serna, C. J.; Roig, A.; Casas, L.; Martínez, B.; Sandiumenge, F. Surface and Internal Spin Canting in γ-Fe_2O_3 Nanoparticles. *Chem. Mater.* **1999**, *11* (11), 3058–3064.

(29) Alario-Franco, J. M.; Gonzalez-Calbet, M. A. The Porous Structure of Synthetic Akaganeite. *J. Inorg. Nucl. Chem.* **1981**, *43*, 257–264.

(30) Tadic, M.; Milosevic, I.; Kralj, S.; Saboungi, M. L.; Motte, L. Ferromagnetic Behavior and Exchange Bias Effect in Akaganeite Nanorods. *Appl. Phys. Lett.* **2015**, *106* (18).

(31) Zhao, J.; Lin, W.; Chang, Q.; Li, W.; Lai, Y. Adsorptive Characteristics of Akaganeite and Its Environmental Applications: A Review. *Environ. Technol. Rev.* **2012**, *1* (1), 114–126.

(32) Pankhurst, Q. a; Connolly, J.; Jones, S. K.; Dobson, J. Applications of Magnetic Nanoparticles in Biomedicine. *J. Phys. D. Appl. Phys.* **2003**, *36* (13), R167–R181.

(33) Dong Kee Yi, G. C. P. *Nanomaterials: Development and Applications*; Dong Kee Yi, G. C. P., Ed.; CRC Press: Boca Raton, 2010.

(34) Soon, G. K.; Piao, Y.; Park, J.; Angappane, S.; Jo, Y.; Hwang, N. M.; Park, J. G.; Hyeon, T. Kinetics of Monodisperse Iron Oxide Nanocrystal Formation By “heating-Up” process. *J. Am. Chem. Soc.* **2007**, *129* (41), 12571–12584.

(35) Van Embden, J.; Chesman, A. S. R.; Jasieniak, J. J. The Heat-up Synthesis of Colloidal Nanocrystals. *Chem. Mater.* **2015**, *27* (7), 2246–2285.

(36) Frey, N. A.; Peng, S.; Cheng, K.; Sun, S. Magnetic Nanoparticles: Synthesis, Functionalization, and Applications in Bioimaging and Magnetic Energy Storage. *Chem. Soc. Rev.* **2009**, *38* (9), 2532–2542.

(37) Dubois, F.; Mahler, B.; Dubertret, B.; Doris, E.; Mioskowski, C. A Versatile Strategy for Quantum Dot Ligand Exchange A Versatile Strategy for Quantum Dot Ligand Exchange. *J. Am. Chem. Soc.* **2007**, *129* (3), 482–483.

(38) Dong, A.; Ye, X.; Chen, J.; Kang, Y.; Gordon, T.; Kikkawa, J. M.; Murray, C. B. A Generalized Ligand-Exchange Strategy Enabling Sequential Surface Functionalization of Colloidal Nanocrystals. *J. Am. Chem. Soc.* **2011**, *133* (4), 998–1006.

(39) Vargas, J. M.; Nunes, W. C.; Socolovsky, L. M.; Knobel, M.; Zanchet, D. Effect of Dipolar Interaction Observed in Iron-Based Nanoparticles. *Phys. Rev. B - Condens. Matter Mater. Phys.* **2005**, *72* (18), 2–7.

(40) Hwang, D. S.; Harrington, M. J.; Lu, Q.; Masic, A.; Zeng, H.; Waite, J. H. Mussel Foot Protein-1 (Mcfp-1) Interaction with Titania Surfaces. *J. Mater. Chem.* **2012**, *22* (31), 15530–15533.

(41) Lee, B. P.; Messersmith, P. B.; Israelachvili, J. N.; Waite, J. H. Mussel-Inspired Adhesives and Coatings. *Annu. Rev. Mater. Res.* **2011**, *41*, 99–132.

(42) Sedo, J.; Saiz-Poseu, J.; Busque, F.; Ruiz-Molina, D. Catechol-Based Biomimetic Functional Materials. *Adv. Mater.* **2013**, *25* (5), 653–701.

(43) Yu, M.; Hwang, J.; Deming, T. J. Role of L -3,4-Dihydroxyphenylalanine in Mussel Adhesive Proteins. *J. Am. Chem. Soc.* **1999**, *121* (24), 5825–5826.

(44) Shultz, M. D.; Reveles, J. U.; Khanna, S. N.; Carpenter, E. E. Reactive Nature of Dopamine as a Surface Functionalization Agent in Iron Oxide Nanoparticles. *J. Am. Chem. Soc.* **2007**, *129* (9), 2482–2487.

(45) Faure, E.; Falentin-Daudre, C.; Jerome, C.; Lyskawa, J.; Fournier, D.; Woisel, P.; Detrembleur, C. Catechols as Versatile Platforms in Polymer Chemistry. *Prog. Polym. Sci.* **2013**, *38* (1), 236–270.

(46) Liaqat, F.; Tahir, M. N.; Schechtel, E.; Kappl, M.; Auernhammer, G. K.; Char, K.; Zentel, R.; Butt, H.-J.; Tremel, W. High-Performance TiO_2 nanoparticle/DOPA-Polymer Composites. *Macromol. Rapid Commun.* **2015**, *36* (11), 1129–1137.

(47) Liaqat, F.; Tahir, M. N.; Huesmann, H.; Daniel, P.; Kappl, M.; Auernhammer, G. K.; Schneider, D.; Lieberwirth, I.; Char, K.; Fytas, G.; Butt, H.-J.; Tremel, W. Ultrastrong Composites from Dopamine Modified-Polymer-Infiltrated Colloidal Crystals. *Mater. Horiz.* **2015**, *2* (4), 434–441.

(48) Xu, H.; Nishida, J.; Ma, W.; Wu, H.; Kobayashi, M.; Otsuka, H.; Takahara, A. Competition between Oxidation and Coordination in Cross-Linking of Polystyrene Copolymer Containing Catechol Groups. *ACS Macro Lett.* **2012**, *1* (4), 457–460.

(49) Schladt, T. D.; Koll, K.; Prüfer, S.; Bauer, H.; Natalio, F.; Dumele, O.; Raidoo, R.; Weber, S.; Wolfrum, U.; Schreiber, L. M.; Radsak, M. P.; Schild, H.; Tremel, W. Multifunctional Superparamagnetic MnO@SiO_2 Core/shell Nanoparticles and Their Application for Optical and Magnetic Resonance Imaging. *J. Mater. Chem.* **2012**, *22* (18), 9253.

(50) Moridani, M. A.; Scobie, H.; Jamshidzadeh, A.; Salehi, P.; O'Brien, P. J. Caffeic Acid, Chlorogenic Acid, and Dihydrocaffeic Acid Metabolism: Glutathione Conjugate Formation. *Drug Metab. Dispos.* **2011**, *29* (11), 1432–1439.

(51) Amstad, E.; Gillich, T.; Bilecka, I.; Textor, M.; Reimhult, E. Ultrastable Iron Oxide Nanoparticle Colloidal Suspensions Using Dispersants with Catechol-Derived Anchor Groups. *Nano Lett.* **2009**, *9* (5), 4042–4048.

(52) Sun, S.; Zeng, H. Size-Controlled Synthesis of Magnetite Nanoparticles. *J. Am. Chem. Soc.* **2002**, No. 31, 8204–8205.

(53) Viau, G.; Fiévet-Vincent, F. Nucleation and Growth of Bimetallic CoNi and FeNi Monodisperse Particles Prepared in Polyols. *Solid State Ionics* **1996**, *84* (3–4), 259–270.

(54) Fievet, F.; Lagier, J. P.; Figlarz, M. Preparing Monodisperse Metal Powders in Micrometer and Submicrometer Sizes by the Polyol Process. *MRS Bull.* **1989**, *14* (12), 29–34.

(55) Sun, S.; Murray, C. B.; Weller, D.; Folks, L.; Moser, A. Monodisperse FePt Nanoparticles and Ferromagnetic FePt Nanocrystal Superlattices. *Science (80-.).* **2000**, *287* (5460), 1989–1992.

(56) Sergeev, G. B. Synthesis and Stabilization of Nanoparticles. *Nanochemistry* **2006**, 7–36.

(57) Murray, C. B.; Sun, S.; Doyle, H.; Betley, T. Monodisperse 3d Transition-Metal (Co, Ni, Fe) Nanoparticles and Their Assembly into Nanoparticle Superlattices. *MRS Bull.* **2001**, *26* (12), 985–991.

(58) You, H.; Yang, S.; Ding, B.; Yang, H. Synthesis of Colloidal Metal and Metal Alloy Nanoparticles for Electrochemical Energy Applications. *Chem. Soc. Rev.* **2013**, *42* (7), 2880–2904.

(59) Sun, S.; Zeng, H.; Robinson, D. Monodisperse MFe_2O_4 (M= Fe, Co, Mn) Nanoparticles. *J. Am. Cemical Soc.* **2004**, *4* (1), 126–132.

(60) Crouse, C. A.; Barron, A. R. Reagent Control over the Size, Uniformity, and Composition of Co–Fe–O Nanoparticles. *J. Mater. Chem.* **2008**, *18* (35), 4146–4153.

(61) Ahrenstorf, K. Nukleations- und Wachstumsmechanismus von Ni_xPt_{1-x}-Nanopartikel und ihre Charakteristischen Eigenschaften, Dissertation, Hamburg, 2007.

(62) Park, J.; An, K.; Hwang, Y.; Park, J.-G.; Noh, H.-J.; Kim, J.-Y.; Park, J.-H.; Hwang, N.-M.; Hyeon, T. Ultra-Large-Scale Syntheses of Monodisperse Nanocrystals. *Nat. Mater.* **2004**, *3* (12), 891–895.

(63) Xu, Z.; Shen, C.; Hou, Y.; Gao, H.; Sun, S. Oleylamine as Both Reducing Agent and Stabilizer in a Facile Synthesis of Magnetite Nanoparticles. *Chem. Mater.* **2009**, *21* (9), 1778–1780.

(64) Yang, H.; Ogawa, T.; Hasegawa, D.; Takahashi, M. Synthesis and Magnetic Properties of Monodisperse Magnetite Nanocubes. *J. Appl. Phys.* **2008**, *103* (7), 3.

(65) Bao, L.; Low, W.-L.; Jiang, J.; Ying, J. Y. Colloidal Synthesis of Magnetic Nanorods with Tunable Aspect Ratios. *J. Mater. Chem.* **2012**, *22* (15), 7117–7120.

(66) Millan, A.; Urtizberea, A.; Silva, N. J. O.; Palacio, F.; Amaral, V. S.; Snoeck, E.; Serin, V. Surface Effects in Maghemite Nanoparticles. *J. Magn. Magn. Mater.* **2007**, *312* (1).

(67) Fiorani, D.; Testa, A. M.; Lucari, F.; D'Orazio, F.; Romero, H. Magnetic Properties of Maghemite Nanoparticle Systems: Surface Anisotropy and Interparticle Interaction Effects. *Phys. B Condens. Matter* **2002**, *320* (1–4), 122–126.

(68) Singamaneni, S.; Bliznyuk, V. N.; Binek, C.; Tsymbal, E. Y. Magnetic Nanoparticles: Recent Advances in Synthesis, Self-Assembly and Applications. *J. Mater. Chem.* **2011**, *21* (42), 16819–16845.

(69) Vidal-Vidal, J.; Rivas, J.; López-Quintela, M. A. Synthesis of Monodisperse Maghemite Nanoparticles by the Microemulsion Method. *Colloids Surfaces A Physicochem. Eng. Asp.* **2006**, *288* (1–3), 44–51.

(70) Hyeon, T.; Lee, S. S.; Park, J.; Chung, Y.; Na, H. B. Synthesis of Highly Crystalline and Monodisperse Maghemite Nanocrystallites without a Size-Selection Process. *J. Am. Chem. Soc.* **2001**, *123* (51), 12798–12801.

(71) Frison, R.; Cernuto, G.; Cervellino, A.; Zaharko, O.; Colonna, G. M.; Guagliardi, A.; Masciocchi, N. Magnetite-Maghemite Nanoparticles in the 5-15 nm Range: Correlating the Core-Shell Composition and the Surface Structure to the Magnetic Properties. A Total Scattering Study. *Chem. Mater.* **2013**, *25* (23), 4820–4827.

(72) Turta, C.; Melnic, S.; Prodius, D.; Macaev, F.; Stoeckli-Evans, H.; Ruiz, P.; Muraviev, D.;

Pogrebnoi, S.; Ribkovskaia, Z.; Mereacre, V.; Lan, Y.; Powell, A. K. Sunflower Oil Coating on the Nanoparticles of iron(III) Oxides. *Inorg. Chem. Commun.* **2010**, *13* (12), 1402–1405.

(73) Ramos Guivar, J. A.; Bustamante, A.; Flores, J.; Mejia Santillan, M.; Osorio, A. M.; Martinez, A. I.; de Los Santos Valladares, L.; Barnes, C. H. W. Mössbauer Study of Intermediate Superparamagnetic Relaxation of Maghemite (γ-Fe_2O_3) Nanoparticles. *Hyperfine Interact.* **2014**, *224* (1–3), 89–97.

(74) Yathindranath, V.; Rebbouh, L.; Moore, D. F.; Miller, D. W.; van Lierop, J.; Hegmann, T. A Versatile Method for the Reductive, One-Pot Synthesis of Bare, Hydrophilic and Hydrophobic Magnetite Nanoparticles. *Adv. Funct. Mater.* **2011**, *21* (8), 1457–1464.

(75) Lee, S. Y.; Harris, M. T. Surface Modification of Magnetic Nanoparticles Capped by Oleic Acids: Characterization and Colloidal Stability in Polar Solvents. *J. Colloid Interface Sci.* **2006**, *293* (2), 401–408.

(76) Qu, H.; Caruntu, D.; Liu, H.; O'Connor, C. J. Water-Dispersible Iron Oxide Magnetic Nanoparticles with Versatile Surface Functionalities. *Langmuir* **2011**, *27* (6), 2271–2278.

(77) Limaye, M. V.; Singh, S. B.; Date, S. K.; Kothari, D.; Reddy, V. R.; Gupta, A.; Sathe, V.; Choudhary, R. J.; Kulkarni, S. K. High Coercivity of Oleic Acid Capped $CoFe_2O_4$ Nanoparticles at Room Temperature. *J. Phys. Chem. B* **2009**, *113* (27), 9070–9076.

(78) Basti, H.; Ben Tahar, L.; Smiri, L. S.; Herbst, F.; Vaulay, M. J.; Chau, F.; Ammar, S.; Benderbous, S. Catechol Derivatives-Coated Fe_3O_4 and γ-Fe_2O_3 Nanoparticles as Potential MRI Contrast Agents. *J. Colloid Interface Sci.* **2010**, *341* (2), 248–254.

(79) Darezereshki, E. One-Step Synthesis of Hematite (α-Fe_2O_3) Nano-Particles by Direct Thermal-Decomposition of Maghemite. *Mater. Lett.* **2011**, *65* (4), 642–645.

(80) Yang, K.; Peng, H.; Wen, Y.; Li, N. Re-Examination of Characteristic FTIR Spectrum of Secondary Layer in Bilayer Oleic Acid-Coated Fe_3O_4 Nanoparticles. *Appl. Surf. Sci.* **2010**, *256* (10), 3093–3097.

(81) Nikiforov, V.; Koksharov, Y. Magnetism and Verwey Transition in Magnetite Nanoparticles in Thin Polymer Film. *J. Alloys Compd.* **2013**, *2* (569), 58–61.

(82) Bae, C. J.; Angappane, S.; Park, J. G.; Lee, Y.; Lee, J.; An, K.; Hyeon, T. Experimental Studies of Strong Dipolar Interparticle Interaction in Monodisperse Fe_3O_4 Nanoparticles. *Appl. Phys. Lett.* **2007**, *91* (10), 1–4.

(83) Tronc, E.; Nogues, M.; Chaneac, C.; Lucari, F.; D'Orazio, F.; Greneche, J. M.; Jolivet, J. P.; Fiorani, D.; Testa, A. M. Magnetic Properties of Y-Fe2O3 Dispersed Particles: Size and Matrix Effects. *J. Magn. Magn. Mater.* **2004**, *272–276*, 1474–1475.

(84) Benz, M. Superparamagnetism : Theory and Applications. *Superparamagnetism Theory Appl.* **2012**, 1–27.

(85) Papaefthymiou, G. C. The Mössbauer and Magnetic Properties of Ferritin Cores. *Biochim. Biophys. Acta* **2010**, *1800* (8), 886–897.

(86) Schweitzer, M. Synthese von Fe_xO_y - und TiO_2 Nanopartikeln und deren Funktionalisierung mit 3,4-Dihydroxyhydrozimtsäure und Tetramethylammoniumhydroxid, Bachelor Thesis, Mainz, 2016.

(87) Mürbe, J.; Rechtenbach, A.; Töpfer, J. Synthesis and Physical Characterization of Magnetite Nanoparticles for Biomedical Applications. *Mater. Chem. Phys.* **2008**, *110* (2–3), 426–433.

(88) Hatakeyama, M.; Kishi, H.; Kita, Y.; Imai, K.; Nishio, K.; Karasawa, S.; Masaike, Y.; Sakamoto, S.; Sandhu, A.; Tanimoto, A.; Gomi, T.; Kohda, E.; Abe, M.; Handa, H. A Two-Step Ligand Exchange Reaction Generates Highly Water-Dispersed Magnetic Nanoparticles for Biomedical Applications. *J. Mater. Chem.* **2011**, *21* (16), 5959.

(89) Li, F.; Zhi, D.; Luo, Y.; Zhang, J.; Nan, X.; Zhang, Y.; Zhou, W.; Qiu, B.; Wen, L.; Liang, G. Core/shell Fe_3O_4/Gd_2O_3 Nanocubes as T_1 –T_2 Dual Modal MRI Contrast Agents. *Nanoscale* **2016**, *8* (25), 12826–12833.

(90) Mendoza Zélis, P.; Muraca, D.; Gonzalez, J. S.; Pasquevich, G. A.; Alvarez, V. A.; Pirota, K. R.; Sánchez, F. H. Magnetic Properties Study of Iron-Oxide nanoparticles/PVA Ferrogels with Potential Biomedical Applications. *J. Nanoparticle Res.* **2013**, *15* (5), 1613.

(91) Liu, Y.; Chen, T.; Wu, C.; Qiu, L.; Hu, R.; Li, J.; Cansiz, S.; Zhang, L.; Cui, C.; Zhu, G.; You, M.; Zhang, T.; Tan, W. Facile Surface Functionalization of Hydrophobic Magnetic Nanoparticles. *J. Am. Chem. Soc.* **2014**, *136* (36), 12552–12555.

(92) Babes, L.; Denizot, B.; Tanguy, G.; Le Jeune, J. J.; Jallet, P. Synthesis of Iron Oxide Nanoparticles Used as MRI Contrast Agents: A Parametric Study. *J. Colloid Interface Sci.* **1999**, *212* (2), 474–482.

(93) Qian, L.; Zheng, Y.; Xue, J.; Holloway, P. H. Stable and Efficient Quantum-Dot Light-Emitting Diodes Based on Solution-Processed Multilayer Structures. *Nat. Photonics* **2011**,

5 (9), 543–548.

(94) Alonso-Redondo, E.; Huesmann, H.; El Boudouti, E.-H.; Tremel, W.; Djafari-Rouhani, B.; Butt, H.-J.; Fytas, G. Phoxonic Hybrid Superlattice. *ACS Appl. Mater. Interfaces* **2015**, *7* (23), 12488–12495.

(95) Cheng, B.; Shi, W.; Russell-Tanner, J. Synthesis of Variable-Aspect-Ratio, Single-Crystalline ZnO Nanostructures. *Inorg. Chem.* **2006**, *45* (3), 1208–1214.

(96) Kim, T. H.; Jang, E. Y.; Lee, N. J.; Choi, D. J.; Lee, K. J.; Jang, J. T.; Choi, J. S.; Moon, S. H.; Cheon, J. Nanoparticle Assemblies as Memristors. *Nano Lett.* **2009**, *9* (6), 2229–2233.

(97) Murray, C. B.; Sun, S.; Doyle, H.; Betley, T. Monodisperse 3d Transition-Metal (Co,Ni,Fe) Nanoparticles and Their Assembly intoNanoparticle Superlattices. *MRS Bull.* **2001**, *26* (12), 985–991.

(98) Sadamura, H.; Yamashita, K.; Nagai, N. Crystallographic Study of Cobalt Treatment on γ-Fe_2O_3. *J. Appl. Phys.* **1993**, *73* (10), 6731.

(99) Fjellvåg, H.; Grønvold, F.; Stølen, S.; Hauback, B. On the Crystallographic and Magnetic Structures of Nearly Stoichiometric Iron Monoxide. *J. Sol. Stat. Chem.* **1996**, *124* (124), 52–57.

(100) Roonasi, P.; Holmgren, A. A Fourier Transform Infrared (FTIR) and Thermogravimetric Analysis (TGA) Study of Oleate Adsorbed on Magnetite Nano-Particle Surface. *Appl. Surf. Sci.* **2009**, *255* (11), 5891–5895.

(101) Lu, C.; Park, M. K.; Lu, C.; Lee, Y. H.; Chai, K. Y. A Mussel-Inspired Chitooligosaccharide Based Multidentate Ligand for Highly Stabilized Nanoparticles. *J. Mater. Chem. B* **2015**, *3* (18), 3730–3737.

(102) Andrade, Â. L.; Fabris, J. D.; Ardisson, J. D.; Valente, M. A.; Ferreira, J. M. F. Effect of Tetramethylammonium Hydroxide on Nucleation, Surface Modification and Growth of Magnetic Nanoparticles. *J. Nanomater.* **2012**, *2012*.

(103) Gao, F.; Qu, H.; Duan, Y.; Wang, J.; Song, X.; Ji, T.; Cao, L.; Nie, G.; Sun, S. Dopamine Coating as a General and Facile Route to Biofunctionalization of Superparamagnetic Fe_3O_4 Nanoparticles for Magnetic Separation of Proteins. *RSC Adv.* **2014**, *4* (13), 6657.

(104) Lee, G.; Cho, Y.-S.; Park, S.; Yi, G.-R. Synthesis and Assembly of Anisotropic Nanoparticles. *Korean J. Chem. Eng.* **2011**, *28* (8), 1641–1650.

(105) Xu, X.; Cao, R.; Jeong, S.; Cho, J. Spindle-like Mesoporous α-Fe_2O_3 Anode Material Prepared from MOF Template for High-Rate Lithium Batteries. *Nano Lett.* **2012**, 10–13.

(106) Zhang, W. M.; Wu, X. L.; Hu, J. S.; Guo, Y. G.; Wan, L. J. Carbon Coated Fe_3O_4 Nanospindles as a Superior Anode Material for Lithium-Ion Batteries. *Adv. Funct. Mater.* **2008**, *18* (24), 3941–3946.

(107) Liu, G.; Young, K. L.; Liao, X.; Personick, M. L.; Mirkin, C. A. Anisotropic Nanoparticles as Shape-Directing Catalysts for the Chemical Etching of Silicon. *J. Am. Chem. Soc.* **2013**, *135* (33), 12196–12199.

(108) Ozaki, M.; Kratohvil, S.; Matijević, E. Formation of Monodispersed Spindle-Type Hematite Particles. *J. Colloid Interface Sci.* **1984**, *102* (1), 146–151.

(109) Wang, H.; Brandl, D. W.; Le, F.; Nordlander, P.; Halas, N. J. Nanorice: A Hybrid Plasmonic Nanostructure. *Nano Lett.* **2006**, *6* (4), 827–832.

(110) Sánchez-Ferrer, A.; Reufer, M.; Mezzenga, R.; Schurtenberger, P.; Dietsch, H. Inorganic-Organic Elastomer Nanocomposites from Integrated Ellipsoidal Silica-Coated Hematite Nanoparticles as Crosslinking Agents. *Nanotechnology* **2010**, *21* (18), 185603.

(111) Frandsen, C.; Legg, B. a; Comolli, L. R.; Zhang, H.; Gilbert, B.; Johnson, E.; Banfield, J. F. Aggregation-Induced Growth and Transformation of β-FeOOH Nanorods to Micron-Sized α-Fe_2O_3 Spindles. *Crystengcomm* **2014**, *16* (8), 1451–1458.

(112) Bailey, J. K.; Brinker, C. J.; Mecartney, M. L. Growth Mechanisms of Iron Oxide Particles of Differing Morphologies from the Forced Hydrolysis of Ferric Chloride Solutions. *Journal of Colloid and Interface Science*. 1993, pp 1–13.

(113) Musić, S.; Krehula, S.; Popović, S. Effect of HCl Additions on Forced Hydrolysis of $FeCl_3$ Solutions. *Mater. Lett.* **2004**, *58* (21), 2640–2645.

(114) Musić, S.; Krehula, S.; Popović, S.; Skoko, Ž. Some Factors Influencing Forced Hydrolysis of $FeCl_3$ Solutions. *Mater. Lett.* **2003**, *57* (5–6), 1096–1102.

(115) Zhang, X.; Liu, H.; Wei, Y. Catalytic Synthesis and Characterization of Spindle-Type α–Fe_2O_3 Particles. *J. Mater. Res.* **2011**, *20* (3), 628–635.

(116) Seip, C. T.; O'Connor, C. J. Fabrication and Organization of Self-Assembled Metallic Nanoparticles Formed in Reverse Micelles. *Nanostructured Mater.* **1999**, *12* (1), 183–186.

(117) Yanagisawa, K.; Yamasaki, N. Reduction of Hematite to Magnetite under Controlled

Hydrothermal Conditions with Hydrogen Gas. *J. Mater. Sci.* **1991**, *26* (2), 473–478.

(118) Wu, J.; Yang, H. Synthesis and Electrocatalytic Oxygen Reduction Properties of Truncated Octahedral Pt_3Ni Nanoparticles. *Nano Res.* **2011**, *4* (1), 72–82.

(119) Wimmers, O. J.; Arnoldy, P.; Moulijn, J. A. Determination of the Reduction Mechanism by Temperature-Programmed Reduction: Application to Small Iron Oxide (Fe_2O_3) Particles. *J. Phys. Chem* **1986**, *90* (1963), 1331–1337.

(120) H.Lin, Y.Chen, C. l. The Mechanism of Reduction of Iron Oxide by Hydrogen. *Thermochim. Acta* **2003**, *400*, 61–67.

(121) Zieliński, J.; Zglinicka, I.; Znak, L.; Kaszkur, Z. Reduction of Fe_2O_3 with Hydrogen. *Appl. Catal. A Gen.* **2010**, *381* (1–2), 191–196.

(122) Hai, H. T.; Kura, H.; Takahashi, M.; Ogawa, T. Facile Synthesis of Fe_3O_4 Nanoparticles by Reduction Phase Transformation from γ-Fe_2O_3 Nanoparticles in Organic Solvent. *J. Colloid Interface Sci.* **2010**, *341* (1), 194–199.

(123) Zieliński, J.; Zglinicka, I.; Znak, L.; Kaszkur, Z. Reduction of Fe_2O_3 with Hydrogen. *Appl. Catal. A Gen.* **2010**, *381* (1–2), 191–196.

(124) Fan, H. J.; Knez, M.; Scholz, R.; Nielsch, K.; Pippel, E.; Hesse, D.; Zacharias, M.; Goesele, U. Monocrystalline Spinel Nanotube Fabrication Based on the Kirkendall Effect. *Nat. Mater.* **2006**, *5* (8), 627–631.

(125) Zeng, S.; Tang, K.; Li, T.; Liang, Z.; Wang, D.; Wang, Y.; Zhou, W. Hematite Hollow Spindles and Microspheres: Selective Synthesis, Growth Mechanisms, and Application in Lithium Ion Battery and Water Treatment. *J. Phys. Chem. C* **2007**, *111* (28), 10217–10225.

(126) Gilbert, K. E.; Gajewski, J. J. Coal Liquefaction Model Studies: Free Radical Chain Decomposition of Diphenylpropane, Dibenzyl Ether, and Phenethyl Phenyl Ether via .beta.-Scission Reactions. *J. Org. Chem.* **1982**, *47* (25), 4899–4902.

(127) Chen, R.; Christiansen, M. G.; Sourakov, A.; Mohr, A.; Matsumoto, Y.; Okada, S.; Jasanoff, A.; Anikeeva, P. High-Performance Ferrite Nanoparticles through Nonaqueous Redox Phase Tuning. *Nano Lett.* **2016**, *16* (2), 1345–1351.

(128) Murad, E. Mössbauer and X-Ray Data on β-FeOOH (Akaganeite). *Clay Miner.* **1979**, *14*, 273–283.

(129) Cai, J.; Liu, J.; Gao, Z.; Navrotsky, A.; Suib, S. L. Synthesis and Anion Exchange of Tunnel Structure Akaganeite. *Chem. Mater.* **2001**, *13* (12), 4595–4602.

(130) Elzinga, E. J.; Sparks, D. L. Phosphate Adsorption onto Hematite: An in Situ ATR-FTIR Investigation of the Effects of pH and Loading Level on the Mode of Phosphate Surface Complexation. *J. Colloid Interface Sci.* **2007**, *308* (1), 53–70.

(131) Roberts, A. P.; Liu, Q.; Rowan, C. J.; Chang, L.; Carvallo, C.; Torrent, J.; Horng, C. S. Characterization of Hematite (α-Fe2O3), Goethite (α-FeOOH), Greigite (Fe_3S_4), and Pyrrhotite (Fe_7S_8) Using First-Order Reversal Curve Diagrams. *J. Geophys. Res. Solid Earth* **2006**, *111* (12), 1–16.

(132) Tadic, M.; Milosevic, I.; Kralj, S.; Saboungi, M. L.; Motte, L. Ferromagnetic Behavior and Exchange Bias Effect in Akaganeite Nanorods. *Appl. Phys. Lett.* **2015**, *106* (18).

(133) Ballauff, M. Kettensteife Polymere - Struktur, Phasenverhalten, Eigenschaften. *Angew. Chem.* **1989**, *101* (3), 261–276.

(134) D. Demus, J. W. Goodby, G. W. Gray, H. W. S. and V. V. *Handbook of Liquid Crystals, Low Molecular Weight Liquid Crystals I: Calamitic Liquid Crystals*; John Wiley & Sons, 2011.

(135) Zocher, V. H. Über Freiwillige Strukturbildung in Solen. *Zeitschrift für Anorg. und Allg. Chemie* **1925**, *147*, 91–110.

(136) Davidson, P.; Batail, P.; Gabriel, J. C. P.; Livage, J.; Sanchez, C.; Bourgaux, C. Mineral Liquid Crystalline Polymers. *Prog. Polym. Sci.* **1997**, *22* (97), 913–936.

(137) Davidson, P.; Gabriel, J. C. P. Mineral Liquid Crystals. *Curr. Opin. Colloid Interface Sci.* **2005**, *9* (6), 377–383.

(138) Pisula, W.; Zorn, M.; Chang, J. Y.; Müllen, K.; Zentel, R. Liquid Crystalline Ordering and Charge Transport In Semiconducting Materials. *Macromol. Rapid Commun.* **2009**, *30* (14), 1179–1202.

(139) Flory, P. J.; Ronca, G. Theory of Systems of Rodlike Particles: I. Athermal Systems. *Mol. Cryst. Liq. Cryst.* **1979**, *54* (3), 289–309.

(140) Giorgetti, M.; Passerini, S.; Smyrl, W. H.; Berrettoni, M. Evidence of Bilayer Structure in V_2O_5 Xerogel. *Inorg. Chem.* **2000**, *39* (7), 1514–1517.

(141) Dessombz, A.; Chiche, D.; Davidson, P.; Panine, P.; Chaneac, C.; Jolivet, J. P. Design of

Liquid-Crystalline Aqueous Suspensions of Rutile Nanorods: Evidence of Anisotropic Photocatalytic Properties. *J. Am. Chem. Soc.* **2007**, *129* (18), 5904–5909.

(142) Meuer, S.; Fischer, K.; Mey, I.; Janshoff, A.; Schmidt, M.; Zentel, R. Liquid Crystals from Polymer-Functionalized TiO_2 Nanorod Mesogens. *Macromolecules* **2008**, *41* (21), 7946–7952.

(143) Mathias, F.; Fokina, A.; Landfester, K.; Tremel, W.; Schmid, F.; Char, K.; Zentel, R. Morphology Control in Biphasic Hybrid Systems of Semiconducting Materials. *Macromol. Rapid Commun.* **2015**, *36* (11), 959–983.

(144) Zorn, M.; Meuer, S.; Tahir, M. N.; Khalavka, Y.; Sönnichsen, C.; Tremel, W.; Zentel, R. Liquid Crystalline Phases from Polymer Functionalised Semiconducting Nanorods. *J. Mater. Chem.* **2008**, *18* (25), 3050.

(145) Tahir, M. N.; Zink, N.; Eberhardt, M.; Therese, H. A.; Kolb, U.; Theato, P.; Tremel, W. Overcoming the Insolubility of Molybdenum Disulfide Nanoparticles through a High Degree of Sidewall Functionalization Using Polymeric Chelating Ligands. *Angew. Chem.* **2006**, *45* (29), 4809–4815.

(146) Zorn, M.; Weber, S. A. L.; Tahir, M. N.; Tremel, W.; Butt, H. J.; Berger, R.; Zentel, R. Light Induced Charging of Polymer Functionalized Nanorods. *Nano Lett.* **2010**, *10* (8), 2812–2816.

(147) Zorn, M.; Zentel, R. Liquid Crystalline Orientation of Semiconducting Nanorods in a Semiconducting Matrix. *Macromol. Rapid Commun.* **2008**, *29* (11), 922–927.

(148) Schenkel, J. H.; Samanta, A.; Ravoo, B. J. Self-Assembly of Soft Hybrid Materials Directed by Light and a Magnetic Field. *Adv. Mater.* **2014**, *26* (7), 1076–1080.

(149) Xu, Y.; Yuan, J.; Fang, B.; Drechsler, M.; Müllner, M.; Bolisetty, S.; Ballauff, M.; Müller, A. H. E. Hybrids of Magnetic Nanoparticles with Double-Hydrophilic Core/shell Cylindrical Polymer Brushes and Their Alignment in a Magnetic Field. *Adv. Funct. Mater.* **2010**, *20* (23), 4182–4189.

(150) Haberl, J. M.; Sánchez-Ferrer, A.; Mihut, A. M.; Dietsch, H.; Hirt, A. M.; Mezzenga, R. Liquid-Crystalline Elastomer-Nanoparticle Hybrids with Reversible Switch of Magnetic Memory. *Adv. Mater.* **2013**, *25* (12), 1787–1791.

(151) Winkler, M.; Kaiser, A.; Krause, S.; Finkelmann, H.; Schmidt, A. M. Liquid Crystal Elastomers with Magnetic Actuation. *Macromol. Symp.* **2010**, *291–292* (1), 186–192.

(152) Wang, M.; He, L.; Zorba, S.; Yin, Y. Magnetically Actuated Liquid Crystals. *Nano Lett.* **2014**, *14* (7), 3966–3971.

(153) Reufer, M.; Dietsch, H.; Gasser, U.; Hirt, A.; Menzel, A.; Schurtenberger, P. Morphology and Orientational Behavior of Silica-Coated Spindle-Type Hematite Particles in a Magnetic Field Probed by Small-Angle X-Ray Scattering. *J. Phys. Chem. B* **2010**, *114* (14), 4763–4769.

(154) Li, D.; Xia, Y. Electrospinning of Nanofibers: Reinventing the Wheel? *Adv. Mater.* **2004**, *16* (14), 1151–1170.

(155) Rieger, K. A.; Birch, N. P.; Schiffman, J. D. Designing Electrospun Nanofiber Mats to Promote Wound Healing – a Review. *J. Mater. Chem. B* **2013**, *1* (36), 4531.

(156) Greiner, A.; Wendorff, J. H. Electrospinning: A Fascinating Method for the Preparation of Ultrathin Fibers. *Angew. Chem.* **2007**, *46* (30), 5670–5703.

(157) Griffin, D. R.; Weaver, W. M.; Scumpia, P. O.; Di Carlo, D.; Segura, T. Accelerated Wound Healing by Injectable Microporous Gel Scaffolds Assembled from Annealed Building Blocks. *Nat Mater* **2015**, *14* (7), 737–744.

(158) Fan, Z.; Liu, B.; Wang, J.; Zhang, S.; Lin, Q.; Gong, P.; Ma, L.; Yang, S. A Novel Wound Dressing Based on Ag/graphene Polymer Hydrogel: Effectively Kill Bacteria and Accelerate Wound Healing. *Adv. Funct. Mater.* **2014**, *24* (25), 3933–3943.

(159) Loo, A. E. K.; Wong, Y. T.; Ho, R.; Wasser, M.; Du, T.; Ng, W. T.; Halliwell, B. Effects of Hydrogen Peroxide on Wound Healing in Mice in Relation to Oxidative Damage. *PLoS One* **2012**, *7* (11), 49215–49228.

(160) Sen, C. Wound Healing Essentials: Let There Be Oxygen. *Wound Repair Regen.* **2009**, *17* (1), 1–18.

(161) Kanta, J. The Role of Hydrogen Peroxide and Other Reactive Oxygen Species in Wound Healing. *Acta Medica (Hradec Kralove)* **2011**, *54*, 97–101.

(162) Grunwald, P. *Biocatalysis and Nanotechnology*; Pan Stanford Publishing Pte. Ltd, 2017.

(163) Gao, L.; Zhuang, J.; Nie, L.; Zhang, J.; Zhang, Y.; Gu, N.; Wang, T.; Feng, J.; Yang, D.; Perrett, S.; Yan, X. Intrinsic Peroxidase-like Activity of Ferromagnetic Nanoparticles. *Nat. Nanotechnol.* **2007**, *2* (9), 577–583.

(164) Que Jr, L.; Tolman, W. B. Biologically Inspired Oxidation Catalysis. *Nature* **2008**, *455*

(7211), 333–340.

(165) Comba, P.; Gahan, L. R.; Hanson, G. R.; Westphal, M. Phosphatase Reactivity of a dicopper(II) Complex of a Patellamide Derivative--Possible Biological Functions of Cyclic Pseudopeptides. *Chem. Commun.* **2012**, *48* (75), 9364–9366.

(166) Wiester, M. J.; Ulmann, P. A.; Mirkin, C. A. Enzyme Mimics Based upon Supramolecular Coordination Chemistry. *Angew. Chem.* **2011**, *50* (1), 114–137.

(167) André, R.; Natálio, F.; Humanes, M.; Leppin, J.; Heinze, K.; Wever, R.; Schröder, H. C.; Müller, W. E. G.; Tremel, W. V_2O_5 Nanowires with an Intrinsic Peroxidase-like Activity. *Adv. Funct. Mater.* **2011**, *21* (3), 501–509.

(168) Korsvik, C.; Patil, S.; Seal, S.; Self, W. T. Superoxide Dismutase Mimetic Properties Exhibited by Vacancy Engineered Ceria Nanoparticles. *Chem. Commun.* **2007**, No. 10, 1056–1058.

(169) Fan, K.; Cao, C.; Pan, Y.; Lu, D.; Yang, D.; Feng, J.; Song, L.; Liang, M.; Yan, X. Magnetoferritin Nanoparticles for Targeting and Visualizing Tumour Tissues. *Nat. Nanotechnol.* **2012**, *7* (7), 459–464.

(170) Wang, X.; Hu, Y.; Wei, H. Nanozymes in Bionanotechnology: From Sensing to Therapeutics and beyond. *Inorg. Chem. Front.* **2016**, *3* (1), 41–60.

(171) Chaudhari, K. N.; Chaudhari, N. K.; Yu, J.-S. Peroxidase Mimic Activity of Hematite Iron Oxides (α-Fe2O3) with Different Nanostructres. *Catal. Sci. Technol.* **2012**, *2* (1), 119–124.

(172) Dutta, A. K.; Maji, S. K.; Srivastava, D. N.; Mondal, A.; Biswas, P.; Paul, P.; Adhikary, B. Peroxidase-like Activity and Amperometric Sensing of Hydrogen Peroxide by Fe_2O_3 and Prussian Blue-Modified Fe_2O_3 Nanoparticles. *J. Mol. Catal. A Chem.* **2012**, *360*, 71–77.

(173) Mi, F. L.; Shyu, S. S.; Wu, Y. B.; Lee, S. T.; Shyong, J. Y.; Huang, R. N. Fabrication and Characterization of a Sponge-like Asymmetric Chitosan Membrane as a Wound Dressing. *Biomaterials* **2001**, *22* (2), 165–173.

(174) Mansur, H. S.; Sadahira, C. M.; Souza, A. N.; Mansur, A. A. P. FTIR Spectroscopy Characterization of Poly (Vinyl Alcohol) Hydrogel with Different Hydrolysis Degree and Chemically Crosslinked with Glutaraldehyde. *Mater. Sci. Eng. C* **2008**, *28* (4), 539–548.

(175) Wu, M.; Lin, Z.; Wolfbeis, O. S. Determination of the Activity of Catalase Using a europium(III)-Tetracycline-Derived Fluorescent Substrate. *Anal. Biochem.* **2003**, *320* (1), 129–135.

(176) Eberhardt, M.; Mruk, R.; Zentel, R.; Théato, P. Synthesis of Pentafluorophenyl(meth)acrylate Polymers: New Precursor Polymers for the Synthesis of Multifunctional Materials. *Eur. Polym. J.* **2005**, *41* (7), 1569–1575.

(177) Wang, J.; Tahir, M. N.; Kappl, M.; Tremel, W.; Metz, N.; Barz, M.; Theato, P.; Butt, H. J. Influence of Binding-Site Density in Wet Bioadhesion. *Adv. Mater.* **2008**, *20* (20), 3872–3876.

VII. APPENDIX

Appendix of III-1

Experimentals

2 mmol iron(III) acetylacetonate was dissolved in 20 mL of phenyl ether and benzyl ether in the presence of 1,2-hexadecandiole or 10 mmol 1,2-tetradecandiole or 1,2-hexadecandiol, oleic 5 mmol acid and 5 mmol oleyl amine. Volatile compounds were removed under reduced pressure, and the flask was flooded with argon for the reaction. The heating protocol contained two plateaus of 200 °C and 260 °C (boiling temperature). After refluxing for 45 minutes the mixture was cooled to room temperature by removing the heat source. The black particles were precipitated with the help of ethanol. The solid was separated by centrifugation and washed several times with cyclohexane. The precipitation and centrifugation was repeated and the nanoparticles were dried in air. Dried samples were used for magnetization and Mössbauer analysis.

Tables and Figures

Table 4: Elemental analysis of OA capped NP.

Sample	Mass / mg	% C	% H	% N	% S
OA capped NP	4.100	14.72	2.63	0	0
	5.129	14.74	2.64	0	0

Table 5: Parameters of lognormal fit in Figure 11

	BE		PE	
y0	0	0	0	0
xc	7.09636	0.19945	4.38251	0.01483
w	0.23395	0.03653	0.1268	0.00227
A	1.02768	0.12107	0.98177	0.01521

Table 6: Parameters of lognormal fit in **Figure 12**

	HDD		PE	
y0	0	0	0	0
xc	4.53759	0.17547	5.35296	0.10274
w	0.32776	0.03626	0.21817	0.01882
A	1.03351	0.09949	0.9961	0.07419

Table 7: Parameter of lognormal fit in **Figure 13**

	With TDD		Without TDD	
y0	0	0	0	0
xc	7.40295	0.22448	8.42354	0.08509
w	0.2397	0.03001	0.21169	0.00988
A	1.03362	0.10903	1.01091	0.04087

Table 8: Mössbauer parameters of Fe Ox nanoparticles with TDD

Fit Summary

no. of data points: 512
no. of HFD sites in model: 2
no. of parameters in model: 22
no. of refined parameters: 10
reduced $\chi^2 = 3.97711$
uncertainties calculated using the covariance matrix

Global Parameters

Background = 1575610(200) counts
Lorentzian HWHM = 0.2165(42) mm/s

Site Distribution Parameters

	δ_0 (mm/s)	**δ_1**	**ε_0 (mm/s)**	**ε_1**
HFD site 1	0.4414(23)	0*	0*	0*
HFD site 2	0.4343(60)	0*	0*	0*

	A (counts·mm/s)	**A_2/A_3**	**A_1/A_3**
HFD site 1	311000(33000)	2*	3*
HFD site 2	194000(34000)	2*	3*

		p (%)	**$\langle H\rangle$ (kOe)**	**σ_H (kOe)**
HFD site 1	comp 1	100*	511.27(43)	13.08(82)
HFD site 2	comp 1	100*	470.9(61)	29.6(34)

Compiled Site Properties

	Site Populations (%)
HFD site 1	61.6(48)
HFD site 2	38.4(48)

	<CS> (mm/s)	**<ε>** (mm/s)	**<|H|>** (kOe)	**stdev(|H|)** (kOe)	**skew(|H|)**
HFD site 1	0.441395	0	511.269	13.0849	-1.9174e-12
HFD site 2	0.434311	0	470.879	29.5838	1.12647e-12

Table 9: Mössbauer parameters of Fe Ox nanoparticles with HDD

Fit Summary

no. of data points: 512
no. of HFD sites in model: 2
no. of parameters in model: 22
no. of refined parameters: 10
reduced $\chi^2 = 6.71768$
uncertainties calculated using the covariance matrix

Global Parameters

Background = 1659440(190) counts
Lorentzian HWHM = 0.2077(29) mm/s

Site Distribution Parameters

	δ_0 (mm/s)	**δ_1**	**ε_0 (mm/s)**	**ε_1**
HFD site 1	0.4027(41)	0*	0*	0*
HFD site 2	0.4506(42)	0*	0*	0*

	A (counts·mm/s)	**A_2/A_3**	**A_1/A_3**
HFD site 1	277000(44000)	2*	3*
HFD site 2	383000(44000)	2*	3*

		p (%)	**⟨H⟩ (kOe)**	**σ_H (kOe)**
HFD site 1	comp 1	100*	495.2(36)	20.1(17)
HFD site 2	comp 1	100*	519.41(31)	9.81(62)

Compiled Site Properties

	Site Populations (%)
HFD site 1	41.9(48)
HFD site 2	58.1(48)

	<CS> (mm/s)	**<ε>** (mm/s)	**<|H|>** (kOe)	**stdev(|H|)** (kOe)	**skew(|H|)**
HFD site 1	0.402707	0	495.204	20.0607	-5.68911e-13
HFD site 2	0.450636	0	519.411	9.81196	-6.29612e-12

Appendix of III-2

Experimental

Chemicals

Iron acetylacetonate, phenyl ether, oleic acid (technical grade), 1,2-tetradecandiole, oleyl amine (technical grade), 3,4-dihydroxyhydrocinnamic acid (DHHCA), triethylamine, dopamin-hydrochlorid, acrylacid chloride, benzyldithiobenzoat (BDTB), 1,4-dioxane, PMMA (Mw = 35.000 g/mol) dichlormethane, 2,6-Lutidin, 2,2′-Azobis(2-methylpropionitrile) (AIBN), hexane, cyclohexane and dimethylformamide (DMF) were obtained from Sigma Aldrich Germany. Pentafluorphenol was obtained from Fluorochem (fluorochem.co.uk). All chemicals were used without further purification.

Synthesis of maghemite particles

The iron oxide nanoparticles were synthesized with some alterations to a method reported by Sun *et al.* [5259] Briefly, 2 mmol iron acetyl acetonate were mixed in 20 mL phenyl ether (DPE) with 10 mmol 1,2-tetradecanediol, 6 mmol oleic acid, and 6 mmol oleylamine in a 100 mL three neck flask and degassed in vacuum under constant stirring. The reaction mixture was then heated in argon atmosphere to 200 °C and the contents were stirred magnetically at this temperature for 120 min followed by 45 min under reflux conditions 260 °C. The resulting black dispersion was cooled to room temperature. To remove the high boiling solvent and surfactant the particles were precipitated from solution with the help of ethanol. The precipitate was then dispersed in cyclohexane. To extract most of the DPE this washing procedure was repeated two times. The oleate-functionalized particles were carefully dried for further experiments and the dry powder was weighed accurately for Mössbauer spectroscopy and SQUID measurements.

Ligand exchange

The oleate ligand on the surface of the prepared particles was partially replaced with 3,4-dihydroxyhydrocinnamic acid (DHCA). The particles were dispersed in THF. DHCA dissolved in ethanol (p.a.) was added under constant stirring. The ligand was used in abundance to ensure almost complete ligand exchange. The particles were then collected with a magnet and washed with ethanol two times.

PDAm synthesis

The monomer pentafluorophenylacrylate was synthesized by reaction of pentafluorphenol with acrylacid chloride in Cl_2CH_2 in the presence of 2,6-lutidin as a base. The catechol-polymer forming the organic matrix was prepared by a synthesis developed by Theato *et al.* through a RAFT polymerization in 1,4-dioxan of the prepared pentafluorophenylacrylate using AIBN as an initiator and benzyldithiobenzoate (BBDT) as a chain transfer agent leading to the polymer polypentafluorphenylacrylate (PPFA).[176177] The polymer was washed several times with hexane to ensure that no monomer was present during the last step. The ester groups of the pre-polymer were substituted by 3-hydroxytyramine anchor groups in DMF with triethylamine, leading to the final "catechol-polymer" polydoamineacrylate (PDAm) used as the actively binding organic matrix.

Preparation of composites in Mössbauer sampleholder

Hybrid materials were prepared inside a cylindrical PMMA sample holder (1 cm diameter, 0.4 cm deep.). To compare the influence of various ligands and matrices, three different samples were prepared numbered 1-3. Sample (1) contained iron oxide particles inside a passive PMMA matrix, (2) the water soluble particles functionalized with DHHCA were covered in passive polymer PMMA (M_w~ 35000 g/mol, Sigma Aldrich). As a reference the third sample (3) contained nanoparticles covered in an active polymer (PDAm) matrix.

All combinations are listed **Figure 14**. The composites were prepared by diluting 100 mg of the active or passive polymer and 10 mg of the nanoparticles in 0,5 mL DMA or toluene, respectively. All dispersions were carefully filled into the sample holders and then dried at room temperature for 24 h and then for another 6 hours at 50 °C. The sample holders took no damage from the solvent during the drying process.

Preparation of XPS samples

For the XPS measurements three glass slides were sputtered with a thin gold film of several nanometers (thicker than the average penetration depth of XPS electrons). Three concentrated solutions of nanoparticles with oleic acid, DHHCA and PDAm in cyclohexane, ethanol and DMA respectively were prepared. For the PDAm functionalized particles the same particle to polymer ratio as in the before described hybrid composites (10:100) was used. The particles were functionalized with the active polymer in DMA under constant stirring for a day. They were collected by using a strong magnet and then washed with DMA several times to ensure no excess polymer is left in solution. The solutions were poured dropwise onto the glass slides and dried at 80 °C to form a homogeneous film of particles.

Tables and Figures

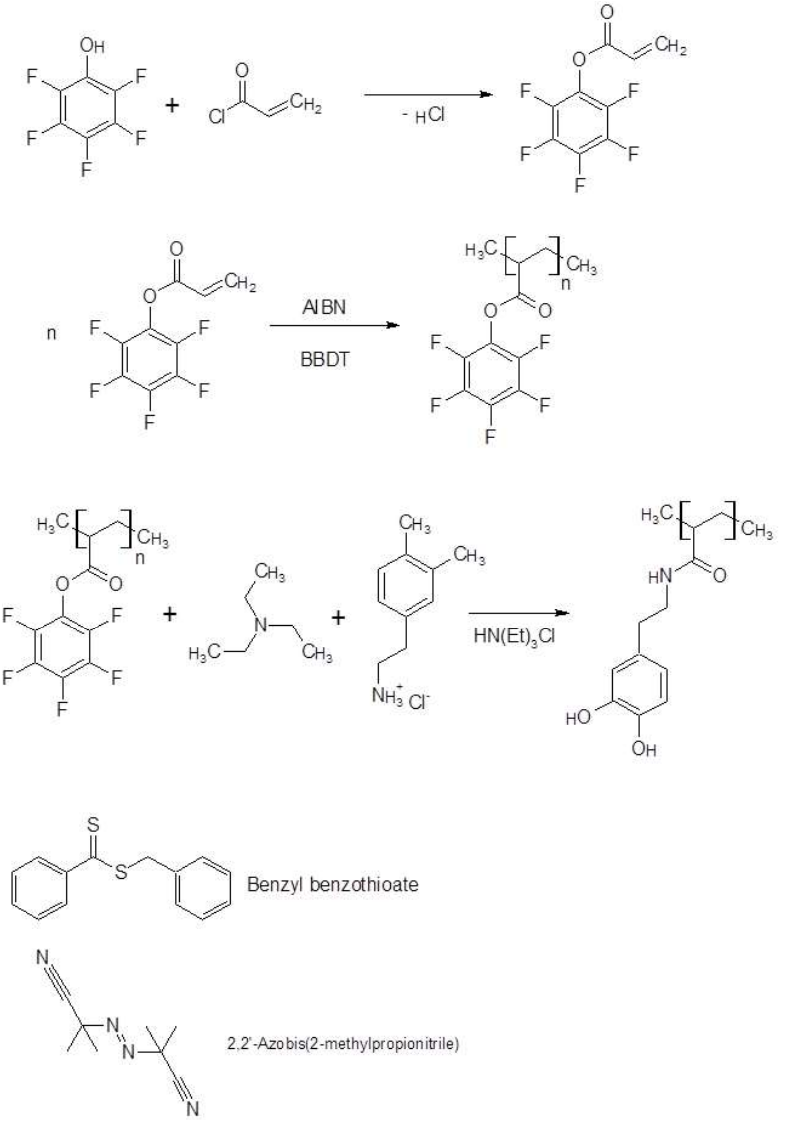

Figure 54: PDAm synthesis. In the first step a reactive ester monomer is formed. By controlled radical polymerization a polymer with narrow molecular weight deviation is produced. In a last polymer analogue reaction dopamine replaces pentafluorophenol. The catechol anchor group later binds to the particle surface.[176,177]

Table 10: Fit-results from lognormal fit of size distribution of OA functionalized NP

Parameter	Value	Deviation
y0	0	0
xc	6.7652	0.07136
w	0.20841	0.01033
A	0.98337	0.0422

Table 11: T_{max} and T_{irr} of OA capped NP and embedded NP in PMMA and PDAm

Sample	T_{max}/K	T_{irr}/K
NP	48	128
1	53	109
2	47	75
3	47	65

Calculation of shell-thickness

$$\frac{\boldsymbol{magnetite}}{\boldsymbol{maghemite}} \cdot \frac{\mathbf{4}}{\mathbf{3}} \boldsymbol{\pi r^3} = \boldsymbol{V_{core}} = \frac{\mathbf{4}}{\mathbf{3}} \boldsymbol{\pi r_{core}}^{\mathbf{3}} \tag{11}$$

$$\sqrt[3]{\frac{\boldsymbol{magnetite}}{\boldsymbol{maghemite}}} \cdot \boldsymbol{r} = \boldsymbol{r_{core}} \leftrightarrow \boldsymbol{r_{shell}} = \boldsymbol{r} - \boldsymbol{r_{core}} \tag{12}$$

Appendix of III-3

Experimental

Chemicals

Iron acetylacetonate (97 %), phenyl ether, oleic acid (technical grade), 1,2-tetradecandiole (technical grade, 90 %), oleyl amine (technical grade), 3,4-dihydroxyhydrocinnamic acid (DHCA) (98 %), TMAH (25 %w in H_2O) were purchased from Sigma Aldrich Germany.

Synthesis of maghemite particles

The OA functionalized iron oxide nanoparticles were synthesized by mixing 2 mmol of iron acetyl acetonate in 20 mL phenyl ether with 10 mmol of 1,2-tetradecanediol, 6 mmol of oleic acid, and 6 mmol of oleylamine in a 100 mL three neck flask and degassed in vacuum under constant stirring. The reaction mixture was then heated in argon atmosphere to 200 °C and the contents were stirred magnetically at this temperature for 120 min followed by 45 min under reflux conditions (260 °C). The resulting black dispersion was cooled down to room temperature. To remove the high boiling solvent and surfactant the particles were precipitated from the solution with ethanol and dispersed in cyclohexane. The washing procedure was repeated two times.

Ligand exchange with excess ligand

TMAH: For the exchange with large ligand excess 10 mg of the prepared particles were added to 1 mL of water inside a 15 mL glass vessel. 250 µL of 25 %w TMAH solution was added dropwise. After a few seconds the film of hydrophobic particles on the surface of the solution began to distribute slowly. Sonication achieved complete dispersion for a short time (for hydrophobic particles). In all cases some precipitate was left at the bottom of the vessel. The particles were precipitated with 14 mL of THF and washed with water twice.

DHCA: 10 mg of as prepared particles were dispersed in THF and 30 mg of DHCA were added. The dispersion was sonicated for 20 minutes and the particles were precipitated with cyclohexane. They were dispersed in water and were precipitated with a THF/cyclohexane mixture. This was repeated two times.

Ligand exchange with small amounts of TMAH

10 mg of the particles were dissolved 1 mL of water and 300 µL, 600 µL, of TMAH-solution (0.025 wt% in H_2O) for “10 %” and “20 %” and 1.5 µL and 3 µL of 25 wt% in H_2O for “50 %” and “100 %” solutions were added. After 20 minutes of sonication the dispersion was decanted carefully and the particles were precipitated with THF. Undispersed and precipitated particles were dried in air at ambient temperatures.

Tables and Figures

Table 12: Fit-parameter of lognormal fit seen in **Figure 21**

Parameter	Value	Standard Error
y0	0	0
xc	9.15811	0.09627
w	0.20235	0.01032
A	101.68959	4.48388

Appendix of IV-4

Experimental

Chemicals

Ferric chloride ($FeCl_3$ 99.9%) and potassium phosphate monobasic powder (KH_2PO_4, > 99 %) were obtained from Sigma Aldrich Germany.

Particle preparation

Ferric chloride and potassium dihydrogen phosphate were slowly dissolved in deionized water and put in a round flask with the respective volume. For 100 mL experiments a 1 cm magnetic stirrer was used. For 250 mL to 1 L experiments a 4 cm magnetic dumbbell stirrer and for 2 L experiment a mechanical stirrer with a 10 cm paddle inside a three-neck flask was used. 100 mL to 1 L were heated in an oil bath. The 2 L flask was heated in a heat mantle. Each flask was equipped with a reflux condenser. Molar amounts of all chemicals are listed in **Table 13**.

Tables and Figures

Table 13: The quantity of precursor chemicals in different experiments.

Reaction volume / mL	Size	n($FeCl_3$) / mmol	n(KH_2PO_4) / mmol
2000	1	40	0.8
1000	1	20	0.4
500	2	20	0.4
500	1	10	0.2
500	1/2	5	0,1
250	1	5	0.1
100	1	2	0.04

Table 14: Parameters of LogNorm fit of akaganeite NP in 250 mL and 1000 mL.

Akaganeite	y0	Δy0	xc	Δxc	w	Δw	A	ΔA
250 mL	0	0	44.02	0.55	0.26	0.01	4.95	0.19
1000 mL	0	0	37.97	0.93	0.24	0.02	4.97	0.43

Appendix of IV-5

Experimental

Chemicals

1,2-Tetradecandiol (90 %), trioctylamine (98 %), phenyl ether (99 %) and benzyl ether (98 %) were purchased from Sigma Aldrich, Germany. H_2/N_2 was obtained from Westfalen AG.

Reduction under H_2/N_2 atmosphere

100 mg of hematite particles were placed in an Al_2O_3 crucible inside a quarts pipe in a tube furnace. A gas flow of approximately 10 mL per minute of H_2/N_2 (5/95) was passed through the pipe and the temperature was increased to 500 °C at a rate of 5 °C/min and kept at this temperature for 3 h. After cooling under H_2/N_2 atmosphere the particles were dispersed in water, filtered (3.1 µm, CME, Roth) and dried in air.

Reduction with 1,2-tetradecandiol

100 mg of hematite or akaganeite particles were dispersed in 20 mL of high boiling solvent (benzyl ether, phenyl ether or trioactyl amine). A fivefold molar amount of 1,2-tetradecandiol was added. The mixture was degassed in a three neck flask under reduced pressure and then heated under argon atmosphere to the respective boiling temperature within 30 min. The mixture was kept under reflux for 45 min and was then cooled down by removing the heat source. The dark dispersion was transferred into 50 mL centrifuge vessels (PP) and precipitated with a threefold volume of ethanol. The particles were washed by repeating the precipitation step in cyclohexane two times, after washing the particles were dried in air.

Tables and Figures

Table 15: Fit parameters of multiple Gaussian fits of as prepared and reduced spindle-shaped nanoparticles in **Figure 34**

spindle-shaped NP			aberration
Basislinie(Constant)	y0	0	0
Impuls1(Gaussian)	xc	222,5271	61,43583
Impuls1(Gaussian)	A	5,48513	5,53871
Impuls1(Gaussian)	w	120,3737	117,37544
Impuls2(Gaussian)	xc	340,7621	16,90715
Impuls2(Gaussian)	A	11,0473	5,78156
Impuls2(Gaussian)	w	67,57553	54,30534
Impuls3(Gaussian)	xc	472,9091	3,04368
Impuls3(Gaussian)	A	34,01493	1,82609
Impuls3(Gaussian)	w	117,4993	7,27579

reduced spindle-shaped NP			
Basislinie(Constant)	y0	0	0
Impuls1(Gaussian)	xc	284,5739	0
Impuls1(Gaussian)	A	11,70365	1,8573
Impuls1(Gaussian)	w	136,5721	24,1856
Impuls2(Gaussian)	xc	408,3843	0
Impuls2(Gaussian)	A	36,35085	1,77014
Impuls2(Gaussian)	w	106,3891	5,63665
Impuls3(Gaussian)	xc	555,1811	0
Impuls3(Gaussian)	A	2,15624	1,30873
Impuls3(Gaussian)	w	77,58472	71,58336

Table 16: Lognormal fit parameters for long axis of short particles in **Figure 34**

	y0	Δy0	xc	Δxc	w	Δw	A	ΔA
Akaganeite lognormal fit	0	0	440	0.52	0.26	0.01	494.59	0.18
Reduced Akaganeite lognormal fit	0	0	3,887	0.81	0.26	0.02	479.09	0.32

Table 17: Lognormal fit of long axis of akaganeite NP in **Figure 35**.

	y0	Δy0	xc	Δxc	w	Δw	A	ΔA
Akaganeite	0	0	43,99468	0,50448	0,25991	0,01112	4,94163	0,18282

Table 18: Parameters of Gaussian fit of desintegrated NPs with OA in **Figure 35**.

	y(0)	xc	A	w
Baseline	0			
Gauss fit 1	-	14,63959	0,18499	218,837
Gauss fit 2	-	881,888	121,465	481,347
Gauss fit 3	-	1,825162	0,16034	249,091
Gauss fit 4	-	3,017557	0,15808	399,227
Gauss fit 5	-	2,222966	0,19654	461,994
Gauss fit 6	-	5,099958	0,01049	12,857
Gauss fit 7	-	3,767203	0,05003	407,574

Table 19: Magnetic properties of akaganeite, hematite and reduced particles. T_{branch} represents the temperature where the ZFC and FC curves merge (see **Figure 37**).

M_{sat} @ 3 T								T_{branch}			
Reduced spindle-shaped NP		Reduced nanorods		Spindle-shaped NP		Nanorods		Reduced spindle-shaped NP	Reduced nanorods	Spindle-shaped NP	Nanorods
5 K	300 K	5 K	300 K	5 K	300 K	5 K	300 K	300 K	260 K	300 K	242 K
47,1	43,5	43,4	37,2	2,0	0,8	2,4	1,4				

Table 20: Reference diffraction pattern shown in **Figure 38**.

Figure	**Compund**	**Source**	**No and database**
Figure 38	Hematite Fe_2O_3	Pauling L, Hendricks S B, "The Structure of Hematite", Journal of the American Chemical Society 47, 781-790 (1925)	96-101-1241 COD (Crystallography Open Database)
Figure 38	Magnetite Fe_3O_4	Haavik C., Stolen S., Fjellvag H., Hanfland M., Hausermann D., "Equation of state of magnetite and its high-pressure modification: Thermodynamics of the Fe-O system at high pressure Sample at P = 0", Amrican Mineralogist 85, 514-523 (2000)	96-900-2317 COD (Crystallography Open Database)
Figure 38	Akaganeite $Cl_{0.42}Fe_2H_{2.32}O_4$	Post J. E., Heaney P. J., Von Dreele R. B., Hanson J. C., "Neutron and temperature-resolved synchrotron X-ray powder diffractionstudy of akaganeite", American Mineralogist 88, 782-788 (2003)	96-900-2991 COD (Crystallography Open Database)
Figure 38	Iron Fe	Nishihara Y., Nakajima Y., Akashi A., Tsujino N., Takahashi E., Funakoshi K., Higo Y., "Isothermal compression of face-centered cubic ironNote: gamma iron, Sample M605, P = 20.64 GPa, T = 1273 K", American Mineralogist 97, 1417-1420 (2012)	96-901-6185 COD (Crystallography Open Database)
Figure 38	Hematite Fe_2O_3	Blake R. L., Hessevick R. E., Zoltai T., Finger L. W., "Refinement of the hematite structure", American Mineralogist 51, 123-129 (1966)	96-900-0140 COD (Crystallography Open Database)

Appendix of IV-6

Tables and Figures

Table 21: GPC data of both used diblock polymers.

Polymer	M_n [g mol^{-1}] [a]	M_w [g mol^{-1}] [a]	PDI [a]	n:m [b]
P(MMA-*b*-DOPA)	17 000	18 400	1.08	11.1:1
P(DEGMEMA-*b*-DOPA)	11 400	14 100	1.24	14.3:1

Table 22: Magnetic properties of α-Fe_2O_3 and reduces particles (mostly Fe_3O_4)

compound	L_{long} / nm	L_{short} / nm	ratio	T_B / K	M_{Sat} / emu/g at 5 T		Remanence / emu/g		Coercitivity / Oe	
					5 K	300 K	5 K	300 K	5 K	300 K
α-Fe_2O_3	428 (27 %)	87 (16 %)	~4,9	>300	2,0	0,8	0,09	0,07	950	450
Fe_3O_4	340 (30 %)	77 (27 %)	~4,4	>300	53,8	48,8	12	8	150	150

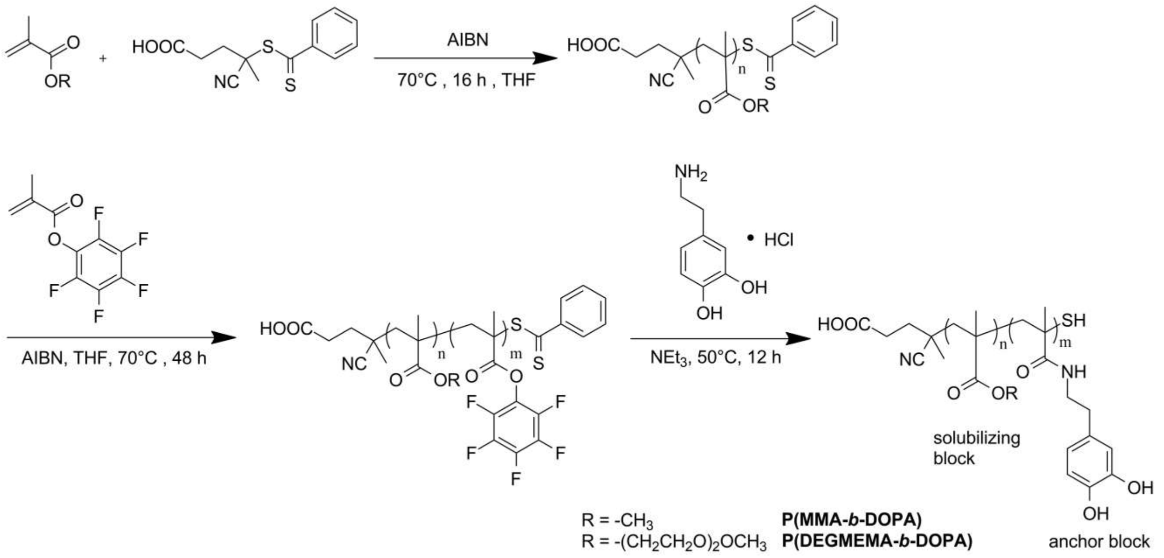

Figure 55: Reaction scheme of P(MMA-b-DOPA) and P(DEGMEMA-b-DOPA). Using RAFT polymerization both polymers are synthesized in two steps. First the solubilizing part is formed and then the anchor block is polymerized using the reactive ester monomer. In the final step pentafluorphenol is substituted with dopamine.

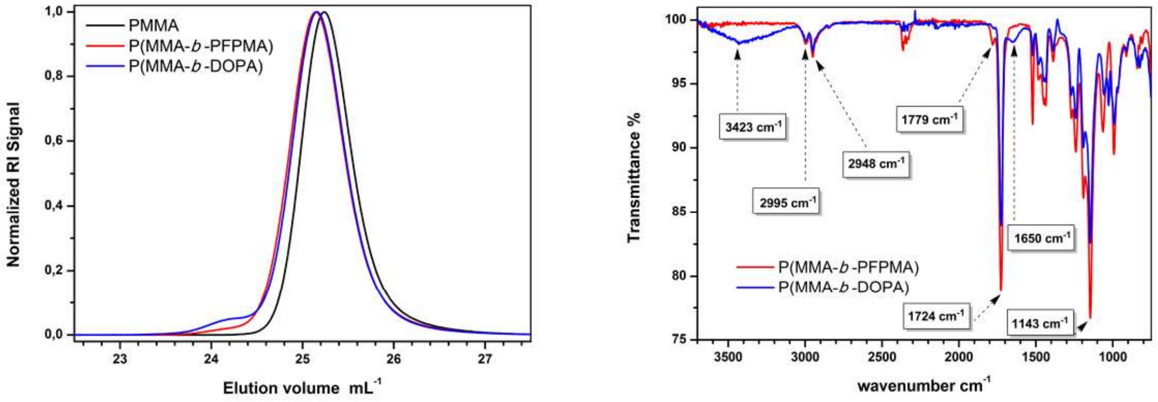

Figure 56: GPC curves of all reaction steps of the polymer synthesis measured in THF with polystyrene standards (left). IR spectra of pure polymers with highlighted characteristic bands on the right. All data collected and plotted by [redacted].

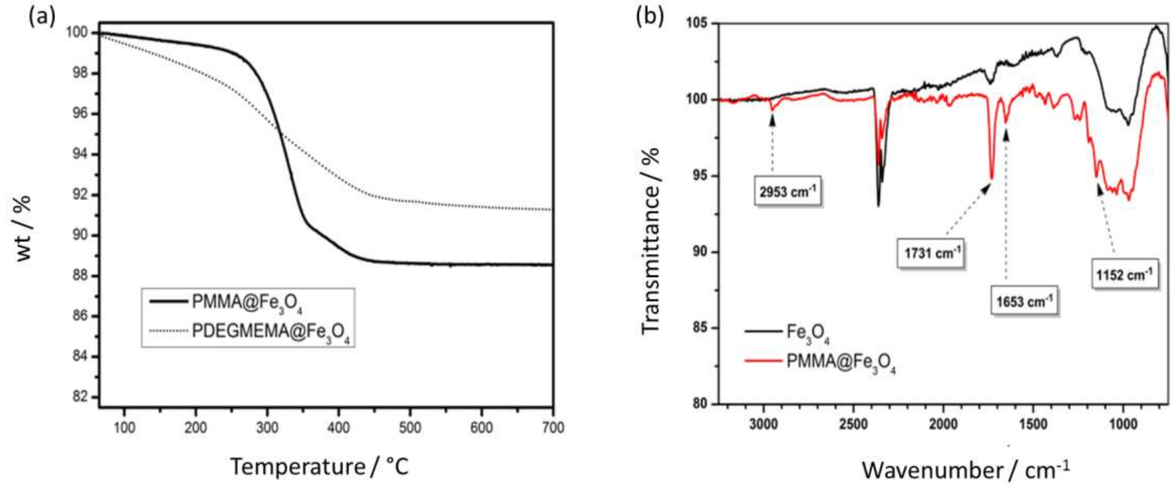

Figure 57: (a) TGA measurement of PMMA and PDEGMEMA on iron oxide nanoparticles. (b) IR spectra of pure Fe_3O_4 NP (black) and PMMA coated NP (red). Characteristic bands of the organic compounds are highlighted. All data collected and plotted by [redacted]

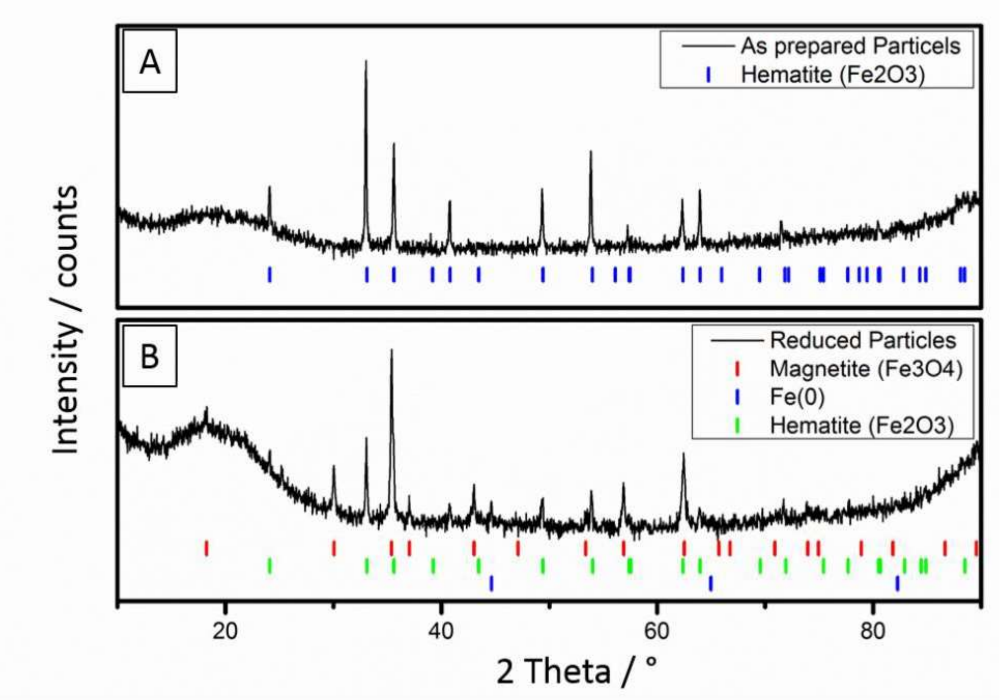

Figure 58: (A) Shows X-ray diffraction data of α-Fe_2O_3 particles, (B) shows diffraction data of reduced particles used in the liquid crystal preparation. The main phase appears to be magnetite but many reflexes can be assigned to remaining hematite and iron (0).

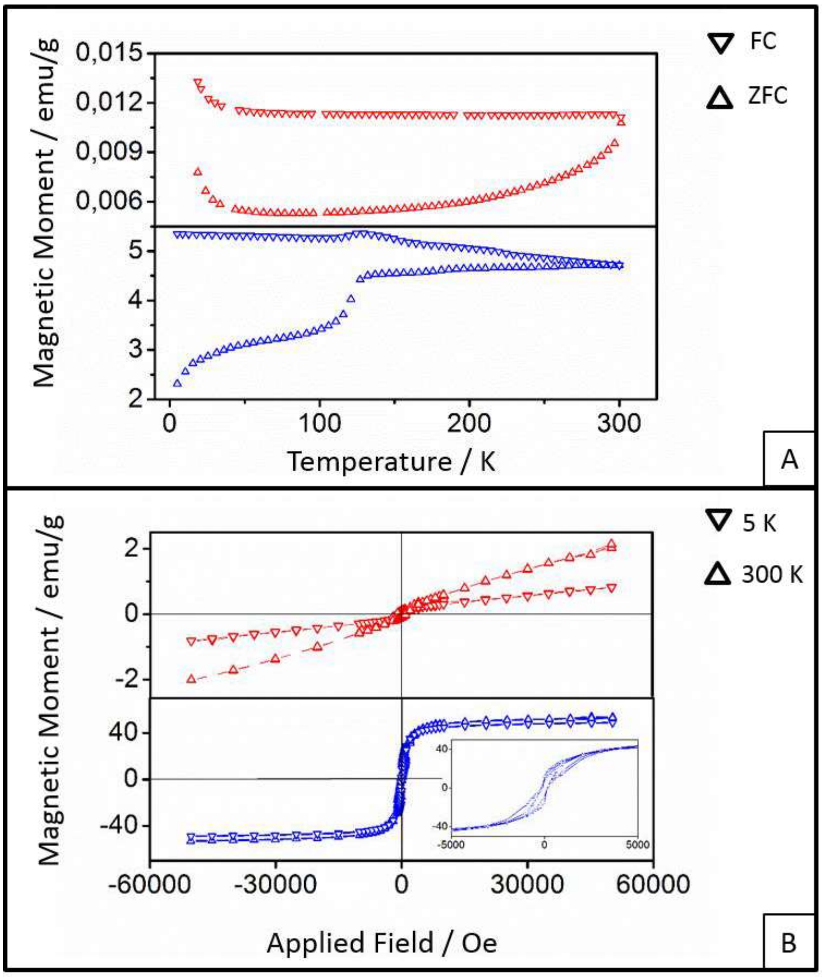

Figure 59: Magnetization measurements of hematite precursor particles and magnetic spindle-shaped particles for LC phases. A) Shows magnetization as a function of temperature. In both cases the ZFC curve exhibits no maximum. The branching temperature, where ZFC and FC curves coincide is 300 K. Hysteresis loops at 300 K and 5 K are depicted in B).

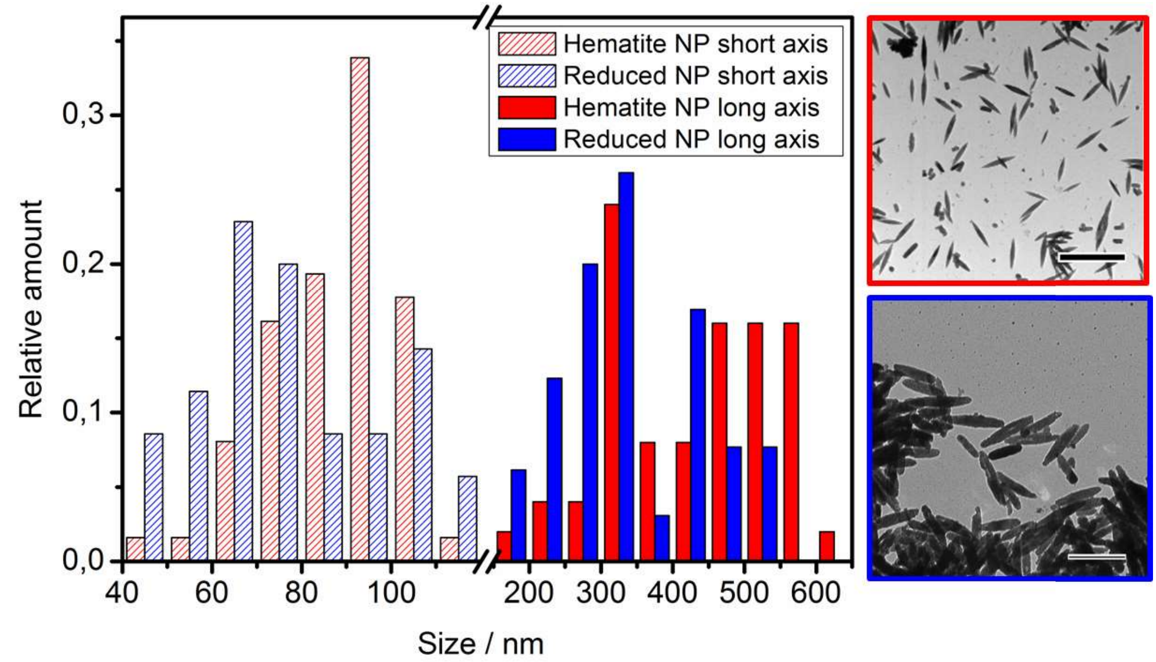

Figure 60: Size deviation of spindle-shaped particles before (red) and after (blue) reduction process. Short axis deviation is shown in striped pattern. Scalebars are 1 µm for hematite (red) and 500 nm for reduced NP (blue).

Appendix of IV-7

Experimental

Chemicals

$FeCl_3*6H_2O$ and THF were purchased from Acros Organics (Fisher Scientific), KH_2PO_4 was purchased from Sigma Aldrich (Germany) for nanoparticle synthesis. Polyvinyl alcohol (PVA, Polysciences Inc., Mw = 125000 g/mol), glutaraldehyde (GA, Merck KGaA, 50 % aqueous solution), and hydrochloric acid (HCl, Sigma-Aldrich, 37 wt.%, AR grade) were used for electrospinning and cross-linking reaction.

Nanoparticle Synthesis

The particles were prepared in a one liter round bottom flask by heating 1 L of water with 20 mmol $FeCl_3$ and 0,4 mmol KH_2PO_4 under reflux for three days. The product was precipitated with THF in several small aliquots, filtered with a 3.1 µm CME syringe filter (Roth) and dried at 80 °C. The combined particles were then divided into three batches to create dispersions of 5 wt.%, 25 wt.%, and 50 wt% in water which were later diluted to 5 wt.%, 15 wt.%, and 25 wt.% for electrospinning procedures. 50 wt% was highly viscous and could not be used for electrospinning.

Electrospinning and cross-linking

The different concentrations of hematite nanoparticles dispersions (5 wt.%, 15 wt.% and 25 wt.%) were combined with the 15 wt.% PVA solution at a ratio of 1:2 for a total polymer concentration of 10 wt.% and mixed through mechanical stirring and vortexing until a homogenous dispersion was obtained. The resulting dispersion was filled into a 1 mL syringe and electrospun at 20-25 % relative humidity and room temperature onto an aluminum foil support (20 cm distance, $0.3\ mL\cdot h^{-1}$ feed rate, 0.8 mm tip diameter, +18 and 0 kV). During the electrospinning, a TEM grid was used to collect samples for TEM measurements. Afterward, the electrospun meshes reacted with the 1 mL of 50 wt.% glutaraldehyde (GA) and 20 µL of 37 wt.% HCl in a vacuum oven. HCl was the catalyst for this cross-linking reaction. Afterwards, the cross-linked nanofibrous mats were put in the fume hood for 24 h to evaporate the unreacted GA and HCl.

Wettability and water stability of cross-linked electrospun mats

The wettability of PVA meshes was measured with a static contact angle measuring system equipped with a side camera (IDS uEye camera) and a goniometer. To test the water stability of PVA mats, those mats were immersed into water for 1 h then transferred into the fume hood to evaporate the excess water overnight. The morphology of PVA mats before and after water immersion were observed by scanning electron microscopy (SEM; Hitachi SU8000, Japan).

Cell-viability experiments

50 mg of PVA membranes without hematite nanoparticles and PVA membranes with high loading of hematite nanoparticles were separately incubated with H_2O_2 at 50 µM for 10 minutes in the shaking bed. Then the membranes and H_2O_2 solutions were mixed with the fibroblast cell line NIH-3T3 for overnight incubation. After a 16-hour incubation, the cells were washed with phosphate-buffered saline solution and detached from the culture vessel with 2.5% trypsin (Gibco, Germany). Before measuring on the CyFlow ML cytometer (Partec, Germany), the cells were stained with 650 µL of propidium iodide solution (diluted in phosphate-buffered saline solution to a final concentration of 2.0 $\mu g \cdot mL^{-1}$) to assess the cell viability. The experiments were performed at the [redacted] with the help of [redacted].

Tests for catalytic activity

To measure catalytic activities Europium(III) chloride hexahydrate and 3-(*N*-morpholino)propanesulfonic acid (MOPS) sodium salt (98 %) from Alfa Aesar, Tetracycline hydrochloride, Catalase enzyme (3000-5000 U/mg) and hydrogen peroxide (H_2O_2) from Sigma-Aldrich were used.

All chemicals were used without further purification and reactions were conducted with MilliQ water.

Catalase assay. The catalase-like activity of the tested materials were investigated similar to the fluorescence assay reported by Wu *et al.*[175] First, the following solutions were prepared.

A) MOPS buffer solution (10 mmol/L): The appropriate amount of MOPS sodium salt was dissolved in 800 mL of MilliQ water and the pH was set to 6.9, which is the pH of the buffer solution. The flask was filled up to 1 L with MilliQ water and the solution was homogenized.

B) $EuCl_3$ solution (6.3 mmol/L of Eu^{3+}): 115.3 mg of $EuCl_3 \cdot 6\ H_2O$ were dissolved in 50 mL of A)

C) Tetracycline hydrochloride solution (2.1 mmol/L): 50.5 mg of tetracycline hydrochloride were dissolved in 50 mL of A)

D) EuTc solution: 5 mL of solution B) and 5 mL C) were mixed and filled up to 50 mL with A).

The fibers were placed in a 96 well plate and the assay was conducted in accordance with the procedure, as described below. In addition to that, control measurements were done with native catalase enzyme. In later case solution E) was used.

E) Solution of native catalase enzyme (0.1 mg/mL):

Procedure:

In a first step the PVA fibers were washed several times with MilliQ water to remove free NPs that are possibly not completely cocooned in the polymer matrix. The fibers were placed in the wells of a 96 well plate, which was set in a temperature controlled (303 K) 96 well plate reader. Inside a 96 well plate the fluorescence active EuTc-HP complex was generated by mixing 65 µL D), 20 µL H_2O_2 solution (5 mmol/L) and 165 µL A). The solution was incubated at 303 K for 10 min. To start the reaction, the EuTc-HP solution was pipetted into the fiber containing wells. The reaction process was observed for 10 min based on the decrease of fluorescence intensity. Control measurements were conducted by varying the concentration of native urease enzyme.

Used Software

Powder X-ray diffraction data was analyzed using EVA (EVA 10.0 Rev. 1, Bruker AXS, Madison (WI) US (2003)) and the Pearson (XXX) crystal structure database (PDF-2, Release 2004, JCPDS – International Centre for Diffraction Data, Newton Square (PA) US (2004)). XRD data refinement was done using Topas (Topas Academic V 4.1, Coelho Software, Brisbane, AUS (2007)). Text, figures and some histograms were created using MS Office 2013 and 2010 and MS Paint. Graphs were plotted using Origin 8$^{\mathrm{TM}}$. All fits were calculated by Origin 8$^{\mathrm{TM}}$. Images of crystal structures were created using Diamond 3.0. Molecule structures and laboratory glassware was created using ACD/chemsketch free version.

Units

Oe: Oersted (magnetic field strength) $1\ Oe = \frac{10^3}{4\pi}\frac{A}{m}$

emu/g (mass magnetization) $1\ emu/g = \frac{A*m^2}{kg}$

Analysis

PXRD: The crystal structure was analyzed using a D8 Advance with molybdenum Kα-radiation ($\lambda = 0.72$ Å) and a Sol-X energy dispersive detector. The nanoparticle powder was dispersed on a scotch^{TM} tape. This causes a broad reflex at small 2 theta values.

IR: To analyze the surface functionalization a Nicolet iS10 ATR FT-IR with a diamond probe head from Thermo Scientific was used. Samples were measured as powder. Suitable data was collected from 650 cm^{-1} nad 4000 cm^{-1}. Also a JASCO FT/IR-4100 with an ATR sampling accessory (MIRacle, Pike Technologies) was used. The number of scans was set to 16 or 32 for LC compounds and functionalized NP respectively.

TEM: TEM images were taken with a Tecnai G2 Spirit from FEI (Hilsboro, USA) with LaB_6 cathode crystal, twin objective and a US 1000 CCD camera from Gatan (Pleasanton, USA). For sample preparation the particles were disperses in water or ethanol and one drop of the dispersion was dried on a carbon coated copper grit from Science Services.

Fluorescence Measurements Wellplate Reader: Fluorescence and Absorbance measurements for catalytic activity essays were done with a 96 Wellplate Reader Infinite 200 Pro (Tecan). For absorbance microplates 96 well made of polystyrene (F-bottom, clear, Greiner bio-one) were used. For fluorescence microplates 96 well made of polystyrene (F-bottom black Greiner bio-one) were used.

Mössbauer: Mössbauer spectroscopy was conducted using a constant-acceleration Mössbauer spectrometer (“Wissel”) equipped with a helium cryostat. All three hybrid composite samples as well as the NP precursor powder were measured in transmission geometry at T = 5 K and are shown in Figure 7. These experiments were conducted using the whole prepared pellet of hybrid compound. Isomer shifts are given relatively to iron metal at ambient temperature. Simulations of the experimental data were performed with the Recoil software.

SQUID: Magnetic properties of all the samples were analyzed using a Quantum Design MPMS-XL SQUID-Magnetometer magnetometer. Nanoparticle powder or small parts of the composite were placed into gelatin capsules that were transferred into the magnetometer in a plastic tube. Temperature dependency of magnetization was measured at 100 Oe for field cooling and zero field cooling respectively. Dependency on magnetic field was measured from up to 50 kOe at 300 K and 5 K respectively.

TGA: Thermogravimetric measurements of the nanoparticles were performed with a Pyris TGA 6 with nitrogen atmosphere in a corundum crucible at a heating rate of 15 °C/min for functionalized particles and 10 °C/min for polymer particle LC systems from 50 to 700 °C after 20 minutes at 50 °C. TGA is also sometimes called DTG (Difference Thermo Gravimetry).

GPC: Molecular weights of all polymers (except those with unprotected catechol groups) were determined using gel permeations chromatography in THF with polystyrene as external and toluene as internal standard. Polymer was detected with refractive index (G 1362A RID, JASCO) and UV/VIS (UV-2075 Plus, JASCO) detectors.

POM: Polarized Light Microscopy images were obtained with an Olympus BX51 microscope equipped with a Color View 2 camera (Soft Imaging Systems).

NMR: ^{1}H NMR and 19F NMR spectra measurements were recorded on a Bruker Avance III HD 300 at 300 MHz and Bruker DRX400 Avance at 400 MHz. The spectra are referenced internally to residual proton signals of the deuterated solvent.

UV-VIS: UV-vis-spectroscopy was performed on a VJasco-630-spectrometer and UV-vis-spectra were analyzed using Spectra Manager 2 (Jasco).

Demagnetizer/Degausser: The demagnetizing experiments were done by the use of a portable Walmag Magnetics hand demagnetiser HD-1. This gadget uses strong (> 1 T) alternating magnetic fields that weaken over time. The applied field must be stronger than the coercivity of the material that should be demagnetized. The alternating field induces a change of magnetization and because the amplitude of the field is decreasing over time the magnetization also decreases until is vanishes. The hysteresis curve of the demagnetized material gets smaller and smaller over time of exposure. Usual frequencies are around 50 Hz.

Elemental Analysis For the elemental analysis, a Vario EL cube from the company Elementar was used.

Plate reader: Plate reader measurements were conducted using an Infinite 200 Pro Plate reader from TECAN. Additionally flat bottom 96 well plates black from Greiner bio-one were used for the catalase assay. The excitation filter was set to 405 nm and the emission filter to 620 nm.

Electron microscopy (EM): The morphology of the PVA meshes were observed by transmission electron microscopy (TEM; JEOL JEM1400, Japan) and scanning electron microscopy (SEM; Hitachi SU8000, Japan). The PVA meshes were electrospun on a 400-mesh copper grid and silicon wafer for the TEM and SEM measurement, respectively.

Fourier-transform infrared spectroscopy (FTIR): The functional groups of crosslinked PVA meshes were measured by Fourier-transform infrared spectroscopy (FTIR). 20 mg of samples was mixed with KBr powder to make a pellet. The recorded wavenumbers of pellets are from 400-4000 cm^{-1}.

Table of figures

Tables

Declaration

I hereby declare that I wrote the dissertation submitted without any unauthorized external assistance and used only sources acknowledged in the work. All textual passages which are appropriated verbatim or paraphrased from published and unpublished texts as well as all information obtained from oral sources are duly indicated and listed in accordance with bibliographical rules. In carrying out this research, I complied with the rules of standard scientific practice as formulated in the statutes of Johannes Gutenberg-University Mainz to insure standard scientific practice.

Date:_____________________ Phillip
Daniel______________________________

Curriculum Vitae

[redacted]

[redacted]

[redacted]	[redacted]
[redacted]	[redacted]

[redacted]

[redacted]	[redacted]
[redacted]	[redacted]
[redacted]	[redacted]
[redacted]	[redacted]
[redacted]	[redacted]

[redacted]

[redacted]	[redacted]
[redacted]	[redacted]

[redacted]

[redacted]	[redacted]
[redacted]	[redacted]
[redacted]	[redacted]

[redacted]

[redacted]	[redacted]
[redacted]	[redacted]
[redacted]	[redacted]
[redacted]	[redacted]
[redacted]	[redacted]

[redacted]	[redacted]

Appendix

No Chemists were harmed during the production of this thesis